UNIVERSITÀ DEGLI STUDI DI UDINE
hic sunt futura

www.uniud.it

Corso di dottorato di ricerca in Scienze dell'Ingegneria Energetica e Ambientale

Ciclo XXX

Titolo della tesi

"*Thermal performance analysis of advanced cooling passages for gas turbine blades*"

Dottorando

Fabio Pagnacco

Supervisore

Prof. Luca Casarsa

Anno di discussione - 2018

UNIVERSITY OF UDINE

DOCTORAL THESIS

Thermal performance analysis of advanced cooling passages for gas turbine blades

Author:
Fabio PAGNACCO

Supervisor:
Prof. Luca CASARSA

Abstract

The Ph.D. project here presented aimed at the design and realization of a rotating test rig for heat transfer measurements on internal cooling passages of gas turbine blades, with the final purpose to apply the developed heat transfer measurement methodology on a realistic geometry of blade cooling channels.
The transient thermocromic liquid crystals (TLC) technique has been used for the measurements. This technique had to be adapted to the requirements of the test rig, hence allowing measurements in rotating conditions and with different temperature step evolutions imposed to the process fluid.
Indeed, the adopted technique is based on the imposition of a temperature step on the fluid that laps the measurement surface, previously painted with thermocromic liquid crystals. The analysis of the surface temperature evolution given by the indication of the liquid crystals allows the evaluation of the surface heat transfer coefficient, that is a direct indicator of the heat transfer distribution of the analyzed surface. In order to replicate the same buoyancy effects induced on the flow by the Coriolis forces during rotation on this complex geometry, the transient measurements are performed with a cold temperature step on the coolant flow.

The validation of both rig and methodology has been performed by tests on a simplified geometry of cooling channel, namely a square channel whit ribs normal to the flow direction installed only on a single wall. Liquid crystals with different activation temperatures were used. In order to stress the measurement chain, hence assess the reliability of the measurements, different temperature evolutions were imposed to the process fluid, also varying the rotating conditions.

Test on a realistic cooling geometry were performed at different rotating conditions. The cooling scheme is made up of three passages connected by two 180 degree bend. Each passage has different aspect ratio and turbulent promoters configuration, also at the end of the first passage and along the trailing edge a flow extraction is imposed.

In this thesis, the rig design and working principle are presented in details. In particular, the solutions adopted to generate the sudden cold temperature step, acquire the experimental data on board of the rotating test model and to control the experimental parameters during tests execution are described. The last chapters are dedicated to the presentation of the validation test and to comment the first results obtained on a realistic cooling channel geometry.

Contents

List of Figures

List of Tables

List of Abbreviations

EF	**E**nhancement **F**actor
LC	**L**iquid **C**rystal
LCT	**L**iquid **C**rystal **T**hermography
LS	**L**eading **S**ide
TIT	**T**urbine **I**nlet **T**emperature
TS	**T**railing **S**ide

List of Symbols

Bo	Buoyancy parameter	-
c	material heat capacity	$\mathrm{J/K}$
$c_{p,a}$	air specific heat capacity	$\mathrm{J/kg\ K}$
$c_{p,g}$	exhausted gas specific heat capacity	$\mathrm{J/kg\ K}$
D_h	hydraulic diameter	m
h	heat transfer coefficient	$\mathrm{W/m^2\ K}$
k	material thermal conductivity	$\mathrm{W/m\ K}$
L	characteristic lenght	m
$\dot{m}_a$	air mass flow rate	$\mathrm{kg/s}$
$\dot{m}_f$	fuel mass flow rate	$\mathrm{kg/s}$
Nu	Nusselt number	-
R	evaluation radius	m
Re	Reynolds number	-
Ro	Rotation number	-
T_3	turbine inlet temperature	K
T_0	initial wall temperature	$\mathrm{°C}$
T_b	bulk flow temperature	$\mathrm{°C}$
T_s	surface temperature	$\mathrm{°C}$
U_b	bulk flow velocity	$\mathrm{m/s}$
β	pressure ratio	-
η_{th}	theoretical efficiency	-
$\eta_{is,c}$	compressor isentropic efficiency	-
$\eta_{is,t}$	turbine isentropic efficiency	-
$\eta_{m,c}$	compressor mechanic efficiency	-
$\eta_{m,t}$	turbine mechanic efficiency	-
μ	air viscosity	$\mathrm{Pa\ s}$
ξ	vorticity	$\mathrm{1/s}$
ρ	air density	$\mathrm{kg/m^3}$
Ω	angular frequency	rad

Chapter 1

Introduction

1.1 Gas turbine overview

Gas turbines are power devices used to produce mechanical energy. The architecture of a gas turbine is composed by three main parts:

- a compressor used to increase the pressure of the processed airflow;
- a combustor in which fuel is added to the compressed air and the mixture is ignited in order to increase the energy of the combusted gas;
- a turbine coupled to the compressor in which the hot gases expand, converting their energy in shaft work output.

The main features of the gas turbine listed above are reported in Fig. 1.1, in the figure is also reported the ideal cycle (Brayton-Joule) that governs the operation of this device.
An isentropic compression (1-2) is the first transformation that ambient air undergoes. Successively, in the combustor, the air undergoes a supply of heat at constant pressure (2-3) to then enter in the turbine where it undergoes isentropic expansion (3-4). The ideal cycle involves, after the turbine expansion, a constant pressure heat transfer (4-1) to return to the starting point.
In real gas turbine:

- an open cycle has to be considered, with fresh air that enters in the compressor and the exhaust gases are suitably treated depending to the application;
- both compression and expansion are irreversible transformations;
- in the combustor, the heat supply is combined to a slight pressure loss;

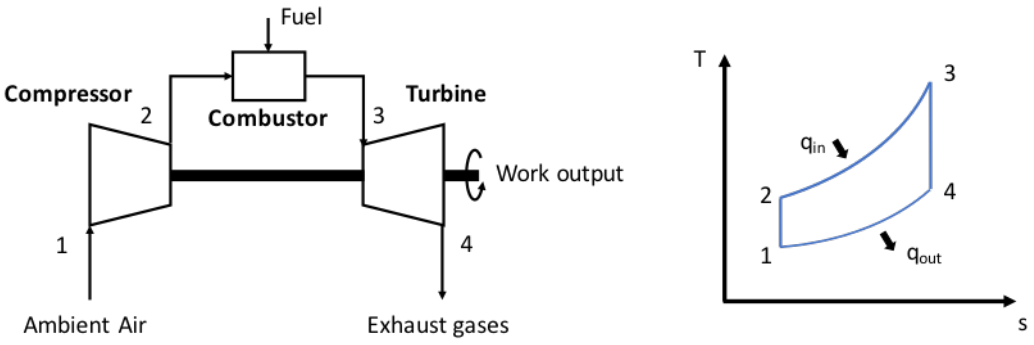

FIGURE 1.1: Turbogas sketch and ideal thermodynamic cycle.

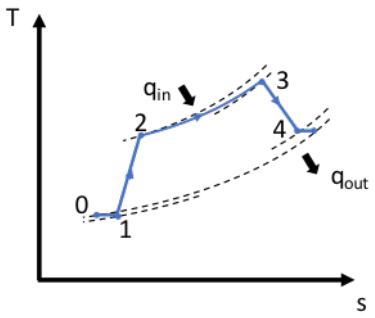

FIGURE 1.2: Turbogas real thermodynamic cycle.

with these considerations, the resulting real cycle is reported in Fig. 1.2.
A part of the work output is used to drive the compressor and electric generators that can be coupled directly or indirectly to the main shaft. The part of energy not converted in the turbine remains into the exhaust gases in the form of high temperature or high velocity.
The principal fields in which gas turbines are used are:

- electric power generation. In this case, the residual energy content of the gases can be used to supply a secondary power generator. This configuration is called combined cycle;
- propulsion (aircraft, ships, trains, etc.). In aircraft applications, the exhausted gases are accelerated after the turbine in order to generate the required thrust. Conversely, for example in naval applications, the residual energy content of the exhaust gases can be recovered using a combined cycle.

In Fig. 1.3 is shown the split of two gas turbine: one used for the production of electrical energy and one used for the propulsion of airliners (in particular of the Boeing 777). It can be immediately noticed how, depending on the application, the two turbo gases have a completely different architecture. Industrial gas turbines, having no substantial limitations in terms of weights and encumbrances, present a more robust and heavier frame, bearings and also blades.
The guideline of gas turbine industries is the continuous improvement of the performances of these devices, namely: increase of the efficiency with the consequent reduction in fuel consumption, improvement of the environmental impact (reduction in emissions and noise), reduction of weights (especially in the aeronautic field).

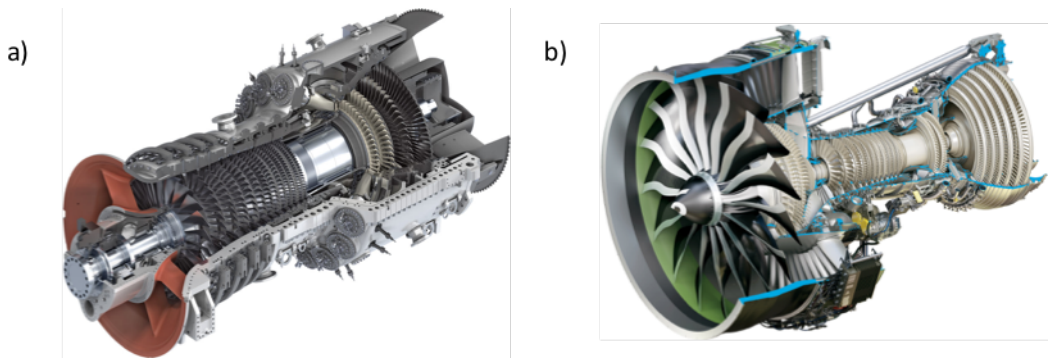

FIGURE 1.3: Siemens SGT5-8000h land based turbine (a), GE90-series aerospace turbine (b).

Last but not least is the economic aspect and the consequent search for reduction in production, maintenance and service costs.

1.2 Increase of gas turbine performances

Concerning the increase of the efficiency of these devices, several considerations can be made. The real cycle efficiency of a gas turbine can be evaluated as:

$$\eta_{th} = \frac{\eta_{is,t}\eta_{m,t}\left(1+\frac{\dot{m}_a}{\dot{m}_f}\right)c_{p,g}T_3\beta^{\frac{k-1}{k}}\left(\beta^{\frac{k-1}{k}}-1\right) - \frac{\frac{\dot{m}_a}{\dot{m}_f}}{\eta_{is,c}\eta_{m,c}}c_{p,a}T_1\left(\beta^{\frac{k-1}{k}}-1\right)}{H_i} \tag{1.1}$$

where β is the overall pressure ratio. It can be seen that for defined pressure ratio and inlet temperature an augmentation of the temperature at the exit of the combustor allows an increase of the theoretical efficiency. This temperature, also named turbine inlet temperature (TIT), is then a fundamental parameter in the design of a gas turbine.
As can be expected, an increase in TIT causes an increase of the stress of all components downstream the combustion chamber. In order to not penalize the useful life of all these components and to avoid breaks without giving up trying to increase the TIT, over the years the solutions summarized in Fig. 1.4 have been developed.
In the early 1950s, the search for new high-temperature resistant alloys has allowed the TIT to rise slightly. The great leap in quality has been enabled by the introduction of blade cooling systems. The simplest systems consisted of only one internal duct in which air bled from the compressor was used to trigger a forced convection. The intensive development of these systems slowed down in the early 2000s, reaching a very high degree of complexity in cooling schemes.

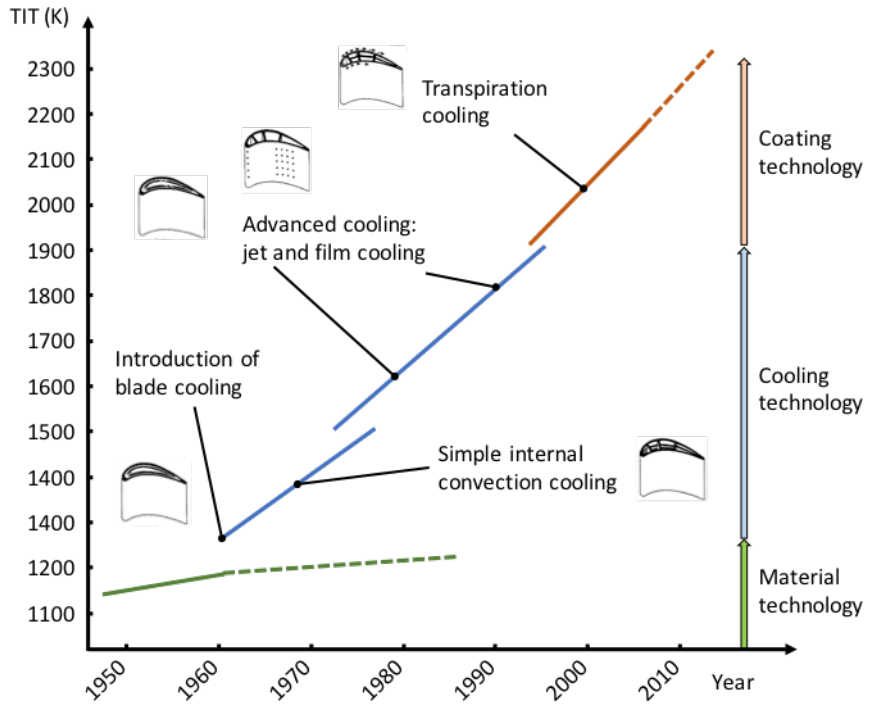

FIGURE 1.4: Evolution of TIT.

In the most complex solution, multiple channeling with turbulence promoters, external film cooling made the design very complicated.
In recent years, the development of new processing technologies and the use of new materials (ceramics) have allowed to further increase the TIT limit, allowing the development of new cooling techniques, such as transpiration cooling.
In turbine blades air cooling systems, the fluid is extracted from the latest compressor stages, resulting in a reduction in efficiency and power. This reduction is largely exceeded by the increase in the total turbine performance that may be due to the use of the cooling system. The gas turbine blade cooling technology is complex and ranges from manufacturer to manufacturer. Also, many of the cooling systems are intellectual property of the manufacturers and are not available in literature. However, these systems can be cataloged depending on the cooling technique used:

- *Internal forced convection cooling*. Is one of the first cooling techniques in which the air coming from the compressor is forced to pass through straight or coil-shaped channels, that are cast or machined inside the blade, and is then discharged into the mainstream formed by the hot gases. Heat extraction takes place by forced convection and heat exchange can be increased by placing repeating geometry elements (such as pins, ribs) inside the channel, which are called turbulence promoters.

- *Impingement cooling*. The cold air that flows inside the blade internal channels is directed against the inner walls of the blade through rows of small holes. The high air velocity caused by these local contractions generates a high thermal exchange in the impact areas of the generated jets. This effect allows a significant reduction of the blade temperature. This cooling method is mainly used in critical blade sections, such as the leading edge.

- *Film cooling*. A thin layer of air, obtained by leaking the cool air through a finite number of holes or slits distributed over the blade, covers and protects the outside surface from high temperature gases. It is currently the most efficient system because it combines both high refrigeration efficiency and a drastic reduction in the compressed air flow rate (smaller compared to other solutions). Unfortunately, this method is also one of the most complicated. In fact, it must be ensured that the air layer remains adherent to the surface and it is delicate in the design phase to estimate the thermal exchange between the surface, the coolant air and the hot gases.

- *Transpiration cooling*. Up to now this method is considered the definitive method for blade cooling. The inner structure of the blade is surrounded by a porous surface through which the air is blown out. In this way, the cooling of the blade structure cooling is guaranteed by the high thermal exchange occurring in porous microchannels. In addition, as in the cooling film, a thin layer of air around the blade is generated and provides extra protection.

The accurate design of the blade cooling scheme, and therefore the appropriate choice of the most effective configuration of the above techniques, plays a crucial role in ensuring that, the maximum surface temperature of the blade and the temperature gradients during operation, are compatible with the thermal stress in order to preserve the useful life of the blades. At the same time the cooling system must also be designed to minimize the bleed air from the compressor stages, in order not to reduce the output power. It is therefore essential for a designer to be able to accurately predict the efficiency of cooling systems in terms of heat transfer.
Inside multi-pass channels different types of turbulent promoters are used to enhance

heat transfer. The choice of which kind of turbulator to install is constrained by the channel cross section dimensions and aspect ratio, which in turns depends upon the blade region where the passage is located. Inclined ribs are usually found in the first legs, which have the task to cool leading edge and main body regions. As said above, in the leading edge region of blades subjected to particular high thermal stresses, in addition to the turbulent promoters also jet impingement can be found. Conversely, inside the thin trailing edge of the airfoil, pin-fin channels or slot ejection are prevalently adopted with combined benefits of structural integrity and heat transfer enhancements.
The thermodynamic and geometric complexity of cooling systems requires the use of numerical calculation methods in order to fully simulate the behavior of these devices. In recent years, accurate numerical models have been developed, thanks to the improvement of the computer architectures. In this way, numerical computations, even on very complex geometries, can be carried out in a reasonable time, with high discretization and accuracy.
In order to validate data obtained from numeric models, experimental tests are required. These tests are an essential method for obtaining information about temperature and surface heat flows, as well as the flow field inside the designed cooling system.
The first fundamental step faced by the researchers was to understand the phenomena that occur inside these cooling systems. In particular the combined effect of turbulent promoters, rotation, and channel orientation and the consequent effect on the heat transfer.

1.2.1 Effects of rotation on internal blade cooling

As said above, in the design of cooling systems for rotor blades, it has to be taken into account the effects of rotation on the flow field and consequently the modification of the thermal field that establish inside the cooling channels. Effects of rotation can be divided in:

- Stabilizing/destabilizing effects on the shear layer;
- Effects of the Coriolis forces;
- Effects of centrifugal forces.

Stabilizing/destabilizing effects on the shear layer
This effect is generated by the interaction of rotation and vorticity of the turbulent shear layer. In order to quantify the stabilizing/destabilizing effects it is useful to define the parameter S as:

$$S = \frac{2\Omega}{\xi} \tag{1.2}$$

where $\xi = -\frac{du}{dy}$ is the vorticity of the turbulent shear layer above mentioned.
Rotation of the channel alters significantly the background flow vorticity of the shear layer. If the two vortex vectors have the same orientation, the parameter S is positive and a stabilizing effect is generated on the shear layer, resulting in a decrease of the turbulent kinetic energy and the Reynolds stresses. On the contrary, if the background flow vorticity has opposite orientation with respect to the angular velocity of the rotating system, a destabilizing effect is generated on the shear layer resulting in an augmentation of the turbulent activity, hence in the mixing of the air belonging to the core flow (normally cold) and the air that flows near to the walls. This enhancement of the mixing is responsible of the augmentation of the heat transfer.

Effect of Coriolis forces on smooth channels
Coriolis forces can be expressed with the relation:

$$\overrightarrow{F_C} = -2M\vec{\Omega} \times \vec{U} \tag{1.3}$$

where $\vec{\Omega}$ is the angular rotating velocity and $\vec{U}$ is the relative velocity of the fluid that flows inside the channel. Therefore, Coriolis force can be decomposed into two components: one is parallel to the main flow direction and one is orthogonal to the flow and directed from the leading side to the trailing side (in green in Fig. 1.5). In order to equilibrate the contribution of the second component, a pressure gradient, constant along the height of the channel, establish with the high pressure in correspondence of the trailing edge and the low pressure in correspondence of the leading edge.

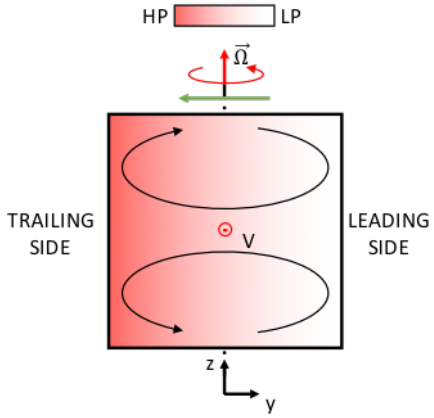

FIGURE 1.5: Generation of secondary induced vortices.

Near the walls, where the boundary layers are located, the velocities of the flow are lower with respect to the main flow (slip condition theory), hence also the intensity of the Coriolis forces are different along the channel height. In particular, lower forces will establish in correspondence of the boundary layers due to the low velocities. Right in this area, the magnitude of the Coriolis force is such that it cannot counteract the pressure gradient. This imbalance leads to the development of a fluid motion from the trailing side to the leading side (low pressure), generating two counter-rotating vortices that moves the fluid from the boundary layers towards the core flow as sketched in Fig. 1.5.
These secondary vortices also cause the acceleration of the fluid in the proximity of the walls where the orthogonal component of the flow speed is coherent with the reference system. Conversely in correspondence of the core flow the instauration of the secondary vortices will cause a reduction of the flow speed.
Depending on the regime of rotation at which the fluid is subjected, different instability can occur on the flow velocity profiles.

- For low rotation regimes, the velocity profile is almost parabolic with the formation of a vortex structure near the walls;
- For intermediate rotation regimes, instability leads to the formation of multiple vortex cells that distort the velocity profile of the flows making it similar to a wave;

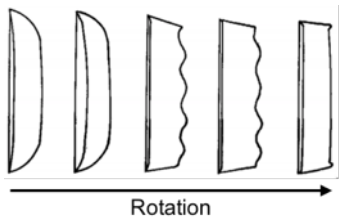

FIGURE 1.6: Evolution of the velocity profiles at different rotation conditions, reported in Hart [15].

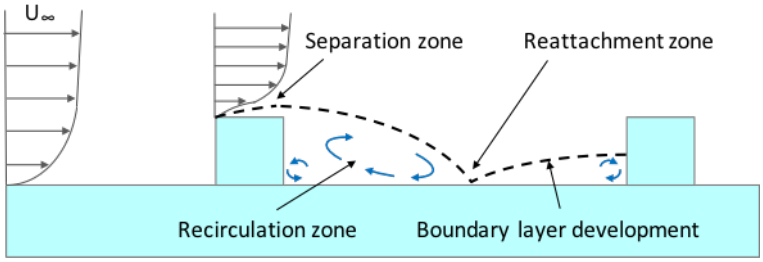

FIGURE 1.7: Flow evolution in a ribbed channel.

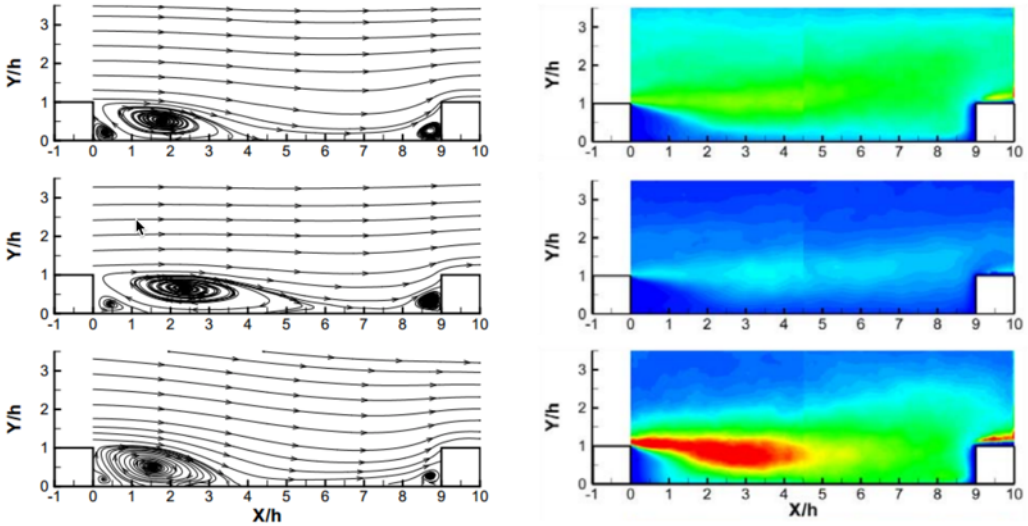

FIGURE 1.8: Flow field (left) and Reynold stresses (right) for a ribbed channel from [10]: static case (top), rotating leading side (mid), rotating trailing side (bottom).

- At high rotation regimes, there is a stabilization of the flow by establishing a Taylor-Proudman regime corresponding to a flat velocity profile, except for areas near the wall where secondary vortexes are present.

These behaviors are well recapped in Fig. 1.6 where the velocity profiles at different rotating conditions are reported.

Effect of Coriolis forces on ribbed channels
The presence of the ribs has a significant impact on the secondary flows with respect to the smooth channel. As reported in Coletti et al. [10] and depicted in Fig. 1.7, the flow that encounters the rib separates in correspondence of the upstream edge. A recirculation zone establishes downstream the rib; the main stream returns to develop a new boundary layer starting from the reattaching point.
As observed for the smooth channels, the action of Coriolis forces displaces the core flow towards the trailing side, altering in fact the stability of the boundary layer generated by the rib. This results in a reduction in the size of the recirculating bubble and, therefore, the reattachment point when the ribs are located on the trailing side. Conversely an extension of the recirculating bubble is observed for the rib to the leading side (Fig. 1.8).
The analysis of the Reynolds stresses (Fig. 1.8), highlight the destabilizing effect of rotation at the trailing side. Conversely, at the leading side, where rotation has a stabilizing effect, a lower turbulent activity is observed with respect to the static case.

Effects of centrifugal forces on ribbed channels
From the definition of the centrifugal force:

$$\overrightarrow{F_{CF}} = m\Omega^2\vec{r} = \rho V\Omega^2\vec{r} \tag{1.4}$$

it can be seen the dependency of this force to the variation of the density, rotation and radial position. Considering a rotating channel, it is clear that for a fixed flow and rotation condition, a variation in the density of the flow generates a variation of the centrifugal forces perceived by the flow. This phenomenon is defined as buoyancy effects.

1.2.2 Literature overview

Several contributions can be found in literature related to the effects of rotation on different types of internal cooling channels. The experimental and numerical results obtained by Hart [15], Lezius and Johnston [23], Johnston et al [19], Tritton [35], Speziale [32], and Speziale and Thangam [33] can be considered as the fundamental contributions describing the Coriolis effects on the flow field inside basic channel geometries (square or rectangular channels with outward flow in orthogonal rotation, i.e. the rotation axis is parallel to the channel height). In these channel configurations, the effect of rotation consists in the development of secondary flow structures made of two symmetrical vortex cells. The number of vortex cells can increase depending on the channel aspect ratio. However, separation and reattachment of the recirculating structures occurs on the leading and trailing walls of the channel, respectively. This leads to a flow unbalance towards the trailing side and a consequent enhancement of heat transfer. On the opposite, thermal performance will reduce on the leading side. The reverse trend is true in radial inward flow passages. Wagner et al. [36] extended the work about rotational effects to rib-roughed channels with ribs installed on both leading and trailing walls. The results show how the local heat transfer coefficients can vary from 0.65 to 4.5 times the values for the fully-developed flow in the smooth passage, with the positive effect measured on the trailing side. The same general behavior is confirmed by Zhou and Acharya [42], who considered

a high aspect ratio (4:1) two pass channel with ribs skewed 45° to the flow and reported heat transfer data on a wide range of working conditions (Re=10.000-70.000, Ro=0-0.7). As said, the above works refer to simplified geometries while more recent contributions clearly show how the flow structure can change significantly if the channel section is no longer rectangular. In Pascotto et al. [27] a triangular shaped smooth channel for leading edge cooling is investigated. By performing detailed PIV measurements and CFD simulations it is demonstrated that the secondary structures differ significantly to the ones found in rectangular channel. Separation and reattachment points do not occur anymore on the channel lateral walls, multiple vortex cells develop streamwise, with a significant impact on the heat transfer performance. Combined effect of ribs, rotation, and buoyancy are studied in Furlani et al. [14] again inside a triangular channel. The results show a different behavior from the rectangular channel case studied by Coletti et al. [10].
In real turbine blades, channels are not always in orthogonal rotation, i.e. the leading and trailing surfaces are not parallel to the rotation axis, because of the blade shape and the channel location. In the experiments of Dutta and Han [12] it is shown how the heat transfer inside a two-pass smooth square channel can vary with the channel orientation angle, the latter being defined as the angle between the channel outer wall in chord-wise direction and the channel rotation direction. The heat transfer inside a rectangular two-pass channel with 2:1 aspect ratio was studied by Huh et al. [16] for two channel orientations (90° and 45°) and smooth or ribbed walls. Again, it was reported how the channel orientation is important to heat transfer development and, in their particular case, it is beneficial to heat transfer augmentation on the leading surface of the first passage.
As already reported, pin-fins are normally used in blade cooling inside narrow channels at the trailing edge. The flow physics in a pin-fin channel are very complicated and three-dimensional in view of the complex and unsteady separation that takes place around the obstacles, and of the possible mutual interaction phenomena of wakes in staggered arrays of pins. This results in high sensitivity of heat transfer coefficients to pin-fin arrangement (Chyu et al. [9] and Metzger er al. [26], to cite few examples).
The scenario is further complicated by the progressive discharge of spent coolant through the trailing edge. Rallabandi et al. [30] highlighted that the progressive flow rate reduction causes a reduction of the local Reynolds number with a detrimental effect on the heat transfer process. Also, the reduction of bulk flow velocity determines the local increase of the rotation number, and rotational effects should therefore change in intensity while moving from hub to tip. However, studies about the effect of rotation in pin fins roughened channels (Rallabandi et al. [30], Willet and Bergles [39], Chang et al. [8]) concluded that it is not significant. A justification is based on the large blockage effect pins-fins have on Coriolis induced secondary flows. On the other hand, the recent work of Qiu et al. [29] investigated the effect of the channel orientation with the use of pin fins. For two extreme values of channel orientation (namely 90° and 180°), a strong variation of heat transfer is reported. A critical value of Ro, which sets an abrupt change in Nu, is also identified. It is therefore evident that there is a need for more detailed investigations into the thermal behavior of pin fin roughened channels under rotation.
The heat transfer performance inside the second and third legs can be significantly modified by the presence of the upstream turn. Indeed, inside the bend region complicated flow structures such as separation, recirculation, and secondary vortices arise as reported in Lei et al. [22]. In the above mentioned contribution and also in [21], Lei et al. shows how adding rotation and channel orientation increases the complexity of the flow, resulting in different behavior if a tip or hub turn is considered. The extended literature available on bend regions flow and losses is still not sufficient to draw conclusion of general validity to be applied for design purposes. Finally, the effects associated with the blade manufacturing process have to be considered. Gas turbine blades are manufactured by

casting, and therefore it is difficult to ensure that the internal passages have sharp edges or perfectly squared ribs. Also, degradation of the casting die due to ageing is an issue which results in rib rounding and filleting even in larger land-based gas turbine engines. Conversely, researchers have focused extensively on channels with sharp edged ribs, documenting heat transfer and friction loss characteristics for a variety of parameters. Only few studies are available on more realistic turbulator geometries and all demonstrated a deterioration in heat transfer due to fillets at the base of the rib (Bayley and Bunker [3], Taslim and Spring [34], Chandra et al. [7]) or pin-fin as reported in Rallabandi et al. [30]. However, in all cases, the effect is a reduction of the pressure losses.
From the literature review of above, it should be clear that the complexity of the modern internal cooling designs makes it difficult to predict the expected thermal performances starting from the available knowledge. Indeed, the majority of the data refers to stereotyped geometrical configurations or the results cannot be projected straightforward to the engine because of lack of full similarity between experiments (real or virtual) and real engine conditions.
This problem can only be overcome if experiments replicate the real working conditions, with particular attention dedicated to the correct reproduction of the rotational effects and the ability to accommodate large test sections that reproduce full blade cooling schemes. Consequently, the demand on size and capabilities of dedicated test rigs is highly increased. The task is to develop facilities where detailed thermal analysis can be performed under rotation at engine similar conditions.
Heat transfer measurement is based on the determination of the local surface temperature, which can be accomplished in several ways. Probably the simplest way to do it is to make use of thermocouples installed on the measurement surface. Examples of the application of this method can be found in the contributions by (Wright et al. [40] and Huh et al. [16]). The main drawback of this method is the spatial resolution achieved, which is usually not sufficient to investigate local heat transfer distributions generated by passage features (i.e. ribs, pins).
Infrared cameras can be used for heat transfer measurement, as reported in Astarita et al. [2]. However, the difficulties in manufacturing test models with walls transparent to infrared radiation can substantially limit the application of this method for very large or complex geometries.
One of the most widely used methods for heat transfer measurements is liquid crystal thermography (LCT). With respect to other methods, LCT technique allows high spatial resolution, it can be performed on very complex surfaces, and finally it provides accurate measurements without requiring expensive devices. Two different methodologies can be followed, i.e. steady or transient LCT. An example of steady LCT applied to blade cooling passages can be found in Mayo et al. [25], which describes the analysis of convective heat transfer distribution in a rib-roughened internal cooling channel at different rotation and Reynolds numbers.
The main disadvantage of steady measurements is the difficulty in providing an accurate estimate of the heat transfer losses through the test model surface, which becomes more significant for rotating experiments.
The transient method is more complex compared to the steady method, but it overcomes the problem of heat losses characterization, moreover it requires much shorter testing time and hence is more suitable to carry out measurements under rotation. Waidmann et al. [38] investigated the heat transfer distribution in a two-pass internal cooling rib-roughened channel with engine-similar cross-section. For this study, the transient TLC technique was used only for stationary measurements.
Other contributions using the transient TLC technique used for stationary measurements are (Domaschke et al. [11] and Kunstmann et al. [20]).

The key point of transient tests is to impose a temperature step to the coolant flow in order to activate the heat transfer process, and hence provide the boundary conditions used to compute the heat transfer coefficient distribution on the investigated surfaces as well reported by Ekkad and Han in [13]. The main issue with the use of this technique for rotating tests is that a cold temperature step on the cooling flow is required in order to match the same buoyancy effects found in real working conditions. Unfortunately, this increases the technical complexity of the system, indeed providing a hot step is rather simpler and can be obtained by widely used mesh heaters.
Additional technical issues that had to be solved are related to the onboard viewing system that is required to record the liquid crystal phase change, the synchronization of this system with the flow temperature acquisition, the data management, communication with the stationary control system and control of the test parameters.

1.3 Scope of the work

In the course of this Ph.D. project, a system for the evaluation of the heat transfer coefficient with transient Liquid Crystal Thermography has been developed. This measurement system allows measurements on different blade cooling schemes (stereotyped geometries or real geometries) in static and rotating conditions.
The first part of the project therefore focused on the design of the test facility and its commissioning, the development of a software that would allow the analysis of the acquired data and thus the calculation of the surface heat exchange coefficient.
The second part of the project focused on the first validation measures of the facility on a stereotyped geometry. Finally, tests were performed on a real cooling geometry, characterized by different turbulence promoters and a complex geometry.

Chapter 2

Heat transfer measurements

The design of an effective blade cooling system is a crucial aspect in order to extend the useful life of the blades and, therefore, of the entire turbine.
Nowadays, the improvement of the computer architecture, has allowed the development of increasingly complex numerical models, including models that simulate flow behaviors that are even close to the reality. Because of this, the need to validate the results provided by these simulations has arisen.
Validation of these models is carried out by conducting experimental campaigns on real, scale, or simplified geometries in order to obtain useful correlations for the designer. Of course, in order to replicate the real working conditions of the tested component, all experiments are performed under thermal and fluid-dynamic similarity.
In order to fully characterize a component (such as blade cooling channels) it is preferable to know both the flow field and the thermal field, the latter in terms of the surface heat transfer coefficient. In this contribution the attention is focused only on the latter aspect, developing a technique for assessing the surface heat transfer coefficient.
Referring to air flows in cooling channels, the heat transfer between the fluid flow and the walls of the channel can be considered caused mainly by forced convection phenomena.
If q is the heat exchanced in the process, h the heat transfer coefficient, T_s the surface temperature and T_b the adiabatic mixing temperature of the flow (bulk temperature), the heat transfer phenomenon can be modeled by means of the relation:

$$q = h(T_b - T_s) \tag{2.1}$$

An accurate evaluation of the surface temperature is needed in order to reduce the errors on the heat transfer coefficient computation.
Several instruments can be used to carry out the measurement of the surface temperature. A first classification can be made by considering the spatial resolution allowable. It is therefore possible to distinguish:

- discrete temperature gauges;
- two-dimensional temperature gauges.

Thermocouples and resistance thermometers are classified among the discrete temperature gauges. Considering the smaller, so less invasive dimensions, thermocouples are preferred, for example, in order to measure the airflow temperature. However, in certain applications, they are used to determine the surface temperature of a wall by immersing it inside copper plates that are integral to the wall. In this way, the space discretization of the temperature information is constrained by the dimensions of the plates.
The most common two-dimensional temperature indicators are:

- *Thermochromic paint pigments*. The operating principle of thermo-sensitive paints is based on the fact that some substances that make up the paint are released at

specific temperatures. As a result of that behavior, when the activation temperature is reached, an irreversible color change is generated. These indicators have low precision and also due to their irreversible nature make their use costly both in terms of time and cost.

- *Phase change paints*. Are similar to temperature-sensitive paints, in the sense that they are irreversible temperature indicators. The phase change paints are provided in the form of suspension in a volatile solvent. They are mixed with specific diluents and sprayed onto the surface, previously painted in black, to form a thin film. These paintings, when they reach a certain temperature, show a clear phase change, becoming transparent and creating a contrast with regions where the painting has not yet reached phase change. This indicator, like the previous one, has a relatively low precision and high costs.

- *Thermochromic liquid crystals*. They provide one of the most convenient, accurate and therefore popular methods for measuring wall temperatures. Their wide use is linked to their reversible and repeatable behavior and a wide temperature range (-30÷115°C) and pressure (up to 133 bar) where they can be used without any special problems. Unlike thermosensitive paints and phase change paints, LC-coated surfaces can be used for a long time, if protected by ultraviolet radiation. Since these types of indicators have been chosen in this work, a more detailed discussion of the measurement technique that sees them involved is referred to in the next paragraph.

It has to be also taken into account in the two-dimensional methods of acquisition of the surface temperature of a body the Infrared thermography. This technique allows the production of a visible image of IR radiation emitted by objects according to their thermal conditions. In this way it is possible to obtain temperature maps with high resolution and short time response. The main problems are related to the emission of surface emissivity and the availability of transparent optical access to IR radiation. Many materials are opaque to IR radiation (eg plexiglass, common glass), so quartz glasses are needed to allow measurement, but these glasses are very expensive.

2.1 Liquid crystals thermography

2.1.1 Introduction to liquid crystals

Liquid crystals thermography (LCT) is a technique used for the evaluation of the surface temperature, essential for the surface heat transfer determination. LCT is based on the property of the cholesteric liquid crystals. These crystals reflect and polarize the incident light at a wavelength that depends on the temperature at which the crystals are exposed. In this way it is possible to associate to each color reflected an indication of temperature. Nowadays this technique has become one of the most used for the experimental determination of the surface heat transfer due to the high spatial resolution achievable with respect to the others techniques and an accuracy on the determination of the surface temperature of about ± 0.3 K.
As can be easily deduced, the main role in this technique is played by liquid crystals. In general liquid crystals can be considered as a liquid, with all the physical properties of the liquids. Furthermore, as indicated by their name, they present the classical molecular organization of a crystal, hence with molecules arranged in different orders depending on the type of the crystal.

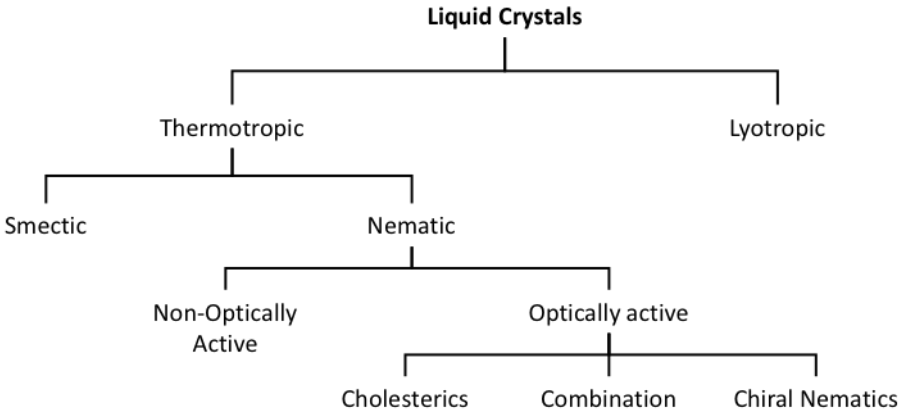

FIGURE 2.1: Liquid crystals classification.

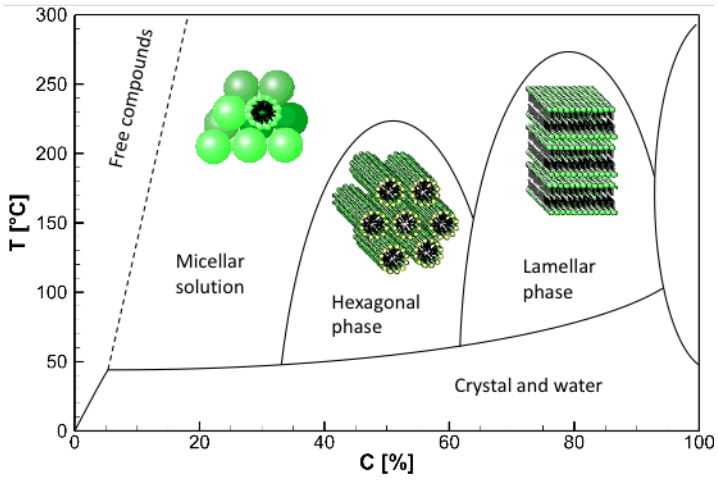

FIGURE 2.2: Lyotropic liquid crystals temperature/concentration dependence.

In Fig. 2.1 is reported a classification of the liquid crystals. The first classes in which liquid crystals are divided are Lyotropic and Thermotropic. The first is formed when certain compounds (e.g. salts of fatty acids) are dissolved in a suitable solvent under appropriate conditions of concentration, temperature and pressure. Acting on these parameters, several types of Lyotropic liquid crystals structure can occur as reported in Fig. 2.2. These materials are widely studied from a biological point of view hence for the purposes of this work are not relevant. More importance is given to the thermotropic liquid crystals since they change phase only if subjected to a variation of temperature. Therefore, in these materials, there is a range of temperatures at which all the phases of the liquid crystal can be seen: crystalline solid, liquid crystal and isotropic liquid. Modifying the temperature in this range can also lead to the observation of several mesophases (see Fig. 2.3), which present different physical properties:

- *Smectic mesophase* can be recognized by two principal characteristics: the long axes of the molecules are all parallel, also molecules are arranged in defined 2D planes, resulting in a layered structure as reported in Fig. 2.3;
- *Nematic mesophase* present molecules with an additional degree of freedom with respect to the Smectic mesophase, the long axes remain parallel and no discrete layers can be identified. Depending on the optical activity Nematic liquid crystals can be mainly divided into *Cholesteric* and *Chiral Nematics* . The first are the most used in all the applications of heat transfer measurements due to their optical properties of light reflection, hence will be the only considered in the further discussion.

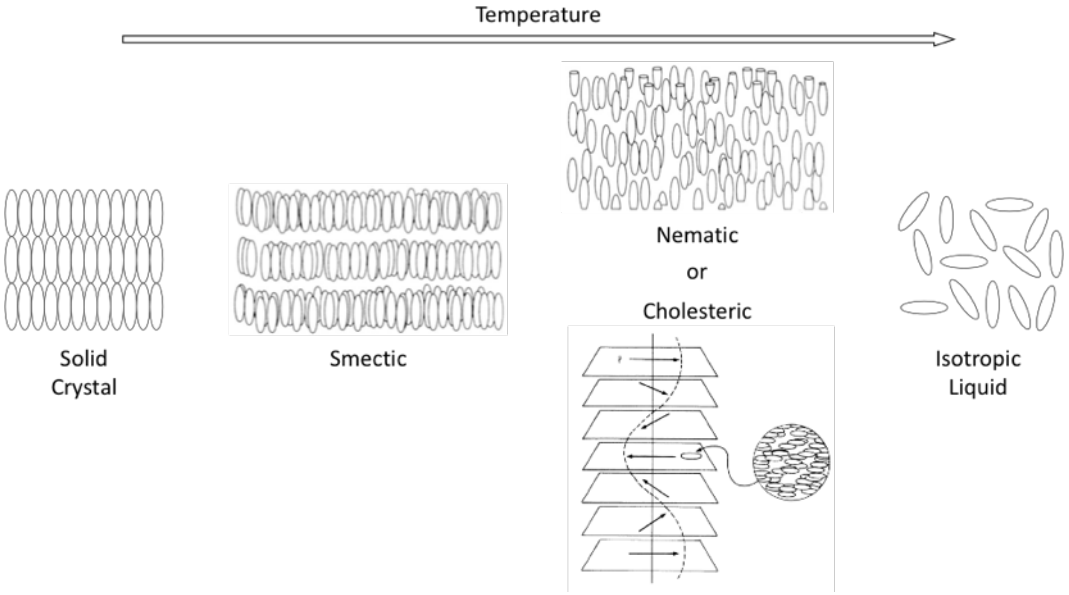

FIGURE 2.3: Phase change of Thermotropic Liquid Crystals.

Cholesteric liquid crystals present a natural twisted structure, with the preferred direction of the long axes of the molecules not constant through the molecular layers, resulting in a helicoidal architecture well reported in Fig. 2.3, where the black arrows represent the average direction of the molecules.
As said before, *cholesteric* liquid crystals have an extremely high optical activity. The anisotropy given by the helicoidal disposition of the molecules allows different optical properties such as:

- birefringence: only certain directions at right angles allow the transmission of a light wave through the material;
- circular dichroism: at given wavelengths, incident light is resolved by the *cholesteric* structure into two polarized components. One is completely reflected while its complementary is completely transmitted through the material. This property depends on the pitch of the helix, hence on the temperature;
- Bragg scattering: the *cholesteric* structure allows the liquid crystal to behave as a three-dimensional diffraction grating for light of visible wavelength. For this reason, the relation between the wavelength of the reflected light and the angle of an incident light beam can be expressed by the Bragg diffraction equation:

$$\lambda = P\,\bar{n}\,\sin\alpha \tag{2.2}$$

where: λ is the wavelength of the selectively reflected light, P is the *cholesteric* helical pitch, $\bar{n}$ is the mean refractive index and α is the angle of incidence normal to the surface.

An increase of temperature causes an expansion of the molecules in the *cholesteric* liquid crystals that results into two opposite effects:

- an increase of the intermolecular distance along the helical axis, hence an increase of the pitch and the reflected wavelength;
- an increase of the displacement angle between the long axes of adjacent molecules, decreasing in fact the pitch of the helix and the reflected wavelength.

The second effect is dominant for almost all commercial temperature-sensitive thermochromic liquid crystals, hence it can be assumed that an increase of temperature causes a reduction of the pitch and a consequent reduction of the reflected wavelength. For this reason, when the temperature ranges in the *cholesteric* region of a specific liquid crystal, the characteristic color change sequence can be seen. An exemplification is given in Fig. 2.4, where is reported the dependence of the reflected wavelength to the variation of the temperature.

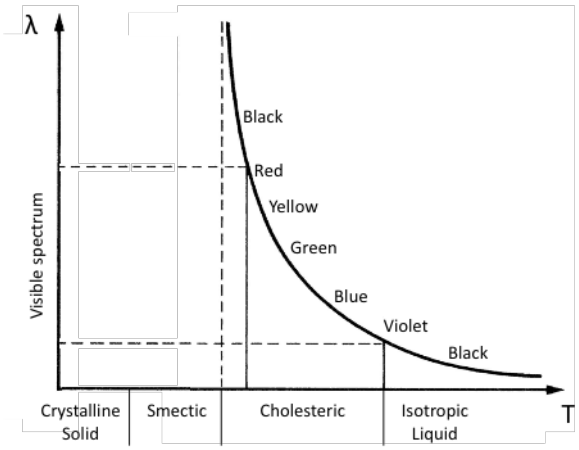

FIGURE 2.4: Reflected wavelength of a temperature-sensitive *cholesteric* liquid crystal.

Depending on the range of temperatures in which the crystals reflect the light in the visible field, two classes can be distinguished:

- narrow banded liquid crystals: characterized by an activation range of few degrees, typically one. Due to the tight range, they are widely used in transient applications;
- wide banded liquid crystals: characterized by a wider activation range with respect to the narrow banded (typically greater or equal to 5 degrees). This type of crystal is mostly used in steady applications.

2.1.2 Applications of LCT

Thanks to their physical and optical properties, liquid crystals can be sprayed directly on the investigated area, becoming a great tool for assessing the surface temperature in a variety of applications. Normally a black paint is also used to increase the contrast of the crystals.
Several techniques have been developed for the measurement of surface temperature by means of the liquid crystals, hence the indirect determination of the surface heat transfer coefficient. These techniques can be grouped into two main categories:

- steady analysis, which includes both black and white (*Akino*) and color versions;
- transient analysis.

Liquid crystal thermography: steady analysis
This technique bases it's fundamentals on the imposition onto the measurement surface of a known and constant heat flux. The liquid crystals sprayed on the surface (see Fig. 2.5), give an indication of the surface temperature. Since the layer of the liquid crystal is very thin (about 0.1 mm) it can be assumed that the temperature indicated by the crystals is exactly the one of the surface on which they are sprayed. Knowing the temperature of the air thanks to thermocouples immersed in the flow, it is possible to evaluate the heat transfer coefficient from the relation:

$$q = h(T_b - T_s) \tag{2.3}$$

In this technique the determination of the heat flux provided to the investigated surface is a crucial aspect. Generally, the heat flux is generated by Joule effect applying a constant voltage to the heads of a very thin flat resistor (Inconel). By doing this it is possible to ensure on the surface, with the exception of edge areas, a uniform current density, hence, for each point of the surface, the heat flux can be evaluated as:

$$q_J = V\ I \tag{2.4}$$

where V is the potential difference between the heads of the Inconel foil and I is the current that flows through it.
The heating flux can be seen as the sum of the conductive, convective and irradiating components as reported below:

$$q_J = q_{cond} + q_{conv} + q_{rad} \tag{2.5}$$

where q_{cond} represents the heat transferred by conduction through the wall, q_{conv} the amount of the supplied heat transferred by convection to the fluid and q_{rad} is the radiative component transferred to the elements that surround the heat source.
Since the interest is to evaluate the convective heat transfer coefficient, in order to reduce

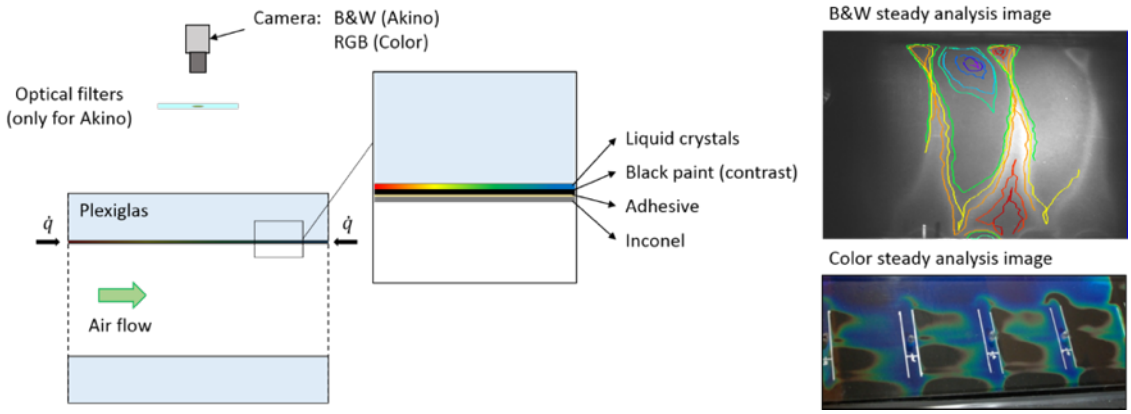

FIGURE 2.5: LCT steady analysis scheme.

errors in its determination, it is necessary to estimate correctly both the conductive and radiative components.
Once all these components are determined it is possible to evaluate the heat transfer coefficient starting from Eq 2.3 as reported below:

$$h = \frac{q_J - q_{cond} - q_{rad}}{T_b - T_s} \tag{2.6}$$

In black and white test mode (*Akino*), a B&W image of the investigated area is captured interposing between the surface and the lens an appropriate band pass optical filter (see Fig. 2.5). In this way, only the information of a given wavelength, then a certain temperature, will be displayed in the image. As can be expected, this technique is very time consuming. For each level of imposed thermal flux, it is necessary to achieve the thermal steadyness of the entire system. Furthermore, in the case of areas with very uneven thermal fields it is necessary to repeat the test several times in order to characterize the entire surface.
With respect to the B&W analysis, in the RGB color modality, the optical filters are not used. A RGB camera acquires an image of the measurement surface. The image is then analyzed using a software that associates to the hue of each pixel, the correspondent temperature value. This method allows test times shorter than the previous one, but it doesn't get away from having to wait for the stationary state of the system before the start of the acquisition.

Liquid crystal thermography: transient analysis
In this technique, a temperature step is imposed to the airflow that laps the investigated surface. A proper analysis of the surface temperature evolution, indicated by the liquid crystals spayed on the surface allows the computation of the surface heat transfer coefficient. A schematic working principle of this technique is reported in Fig. 2.6.
Analyzing the evolution of the color signals (R, G, B) of a sequence of images (see Fig. 2.6) are acquired with a RGB color camera at a constant frame rate (typically 25 Hz), it is possible to determine the activation times (correspondent to the maximum of the color signal) of each portion of the investigated area. A calibration of the liquid crystals allows association of the maximum of the color signal to the correspondent temperature.
Knowing the temperature evolution of the airflow, acquired as the steady approach by means of thermocouples immersed in the flow, and knowing the surface temperature at a specific time instant from the image sequence analysis and the liquid crystal calibration, it is possible to evaluate the surface heat transfer coefficient resolving the general heat

equation under specific assumptions (semi-infinite body and forced convection on the surface).
Referring to the coordinate system of Fig. 2.7, the equation of above can be written as:

$$\rho c \frac{\partial T}{\partial t} + \rho c \left(u \frac{\partial T}{\partial x} + v \frac{\partial T}{\partial y} + w \frac{\partial T}{\partial z} \right) = k \left(\frac{\partial^2 T}{\partial x^2} + \frac{\partial^2 T}{\partial y^2} + \frac{\partial^2 T}{\partial z^2} \right) + \dot{q} \tag{2.7}$$

Under the hypothesis of:

- no heat generation ($\dot{q} = 0$);
- no advection ($u = v = w = 0$);
- negligible lateral conduction ($\frac{\partial^2 T}{\partial x^2} = \frac{\partial^2 T}{\partial y^2} = 0$).

The Eq. 2.7 can be simplified obtaining the well-known Fourier equation:

$$\frac{\partial T}{\partial t} = \alpha \frac{\partial^2 T}{\partial z^2} \tag{2.8}$$

where α is the thermal diffusivity of the solid computed as $\alpha = k/\rho c$.
This equation represents the one-dimensional conduction through a solid describing, in fact, a transient diffusion phenomena. For $t < 0$ the solid and the fluid have the same temperature (T_0). At the instant $t = 0$ a step variation is imposed to the airflow raising the temperature from T_0 to T_b. This temperature variation sets the start of a convective heat transfer phenomenon between the airflow and the solid.
Assuming a pure forced convection phenomenon, it can be ensured the independency of heat transfer coefficient from surface temperature variations. Starting from these considerations and with the assumption of semi-infinite body, the initial and boundary conditions can be assumed as:

- $$T = T_0 \text{ for } z \geq 0 \wedge t = 0 \text{ and } z \to \infty \wedge t > 0 \tag{2.9}$$
- $$q_s = -k \left(\frac{\partial T}{\partial z} \right)_{z=0} = h(T_b - T_s) \tag{2.10}$$

Considering the non-dimensional parameters both Fourier equation and boundary conditions can be expressed in terms of Biot and Fourier numbers. The Biot number:

$$Bi = \frac{hL}{k} \tag{2.11}$$

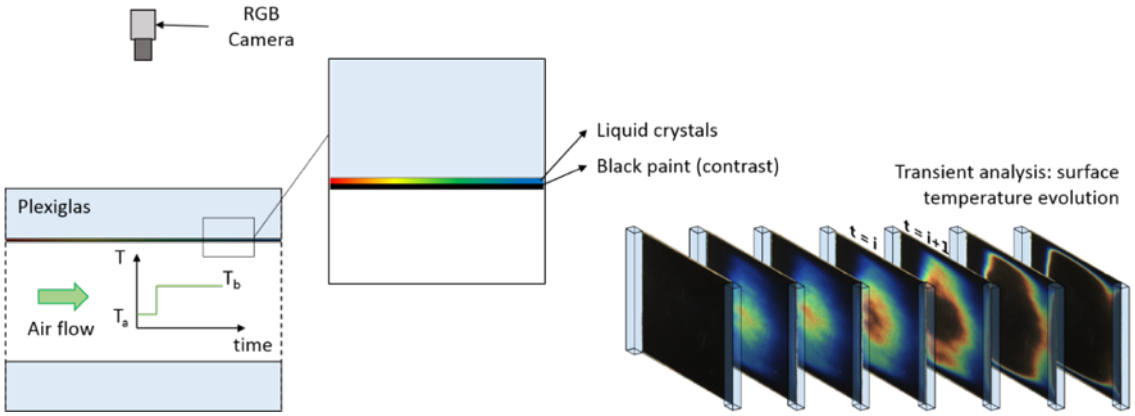

FIGURE 2.6: LCT transient analysis scheme.

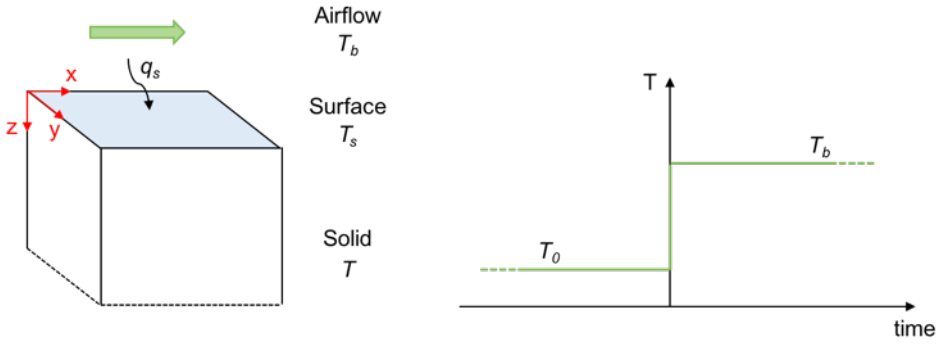

FIGURE 2.7: LCT transient analysis model.

represents an index of the ratio of the heat transfer resistances inside of and on the surface of a body, while the Fourier number:

$$Fo = \frac{\alpha t}{L^2} \tag{2.12}$$

is a dimensionless time parameter. Then, the Fourier equation 2.8 can be written as:

$$\frac{\partial \theta}{\partial Fo} = \frac{\partial^2 \theta}{\partial \zeta^2} \tag{2.13}$$

and the initial and boundary conditions as:

- $$\theta = 0 \text{ for } \zeta \geq 0 \wedge Fo = 0 \text{ and } \zeta \to \infty \wedge Fo > 0 \tag{2.14}$$
- $$-\left(\frac{\partial \theta}{\partial \zeta}\right)_{\zeta=0} = Bi(1-\theta_s) \tag{2.15}$$

where $\zeta = z/L$ is a dimensionless coordinate and $\theta = (T - T_0)/(T_b - T_0)$ the dimensionless temperature.

Resolving the Eq. 2.13 for $z = 0$, hence for $\zeta = 0$, the solution reported below is found:

$$\theta_s = \frac{T_s - T_0}{T_b - T_0} = 1 - \exp(\beta^2)\text{erfc}(\beta) \tag{2.16}$$

where erfc is the complementary error function and β is defined as:

$$\beta = Bi\sqrt{Fo} = h\sqrt{\frac{t}{\rho c k}} \tag{2.17}$$

It can be seen that in the solution of the Fourier equation the heat transfer coefficient appears in both exponential and complementary error functions, in this way it is not directly evaluable. Knowing the material physical properties, the surface, flow and initial temperatures it is possible to compute the heat transfer coefficient only with iterative methods.
As said before, this solution is found under the hypothesis of imposition of a step temperature variation to the fluid that triggers the heat transfer process. In experimental applications, is impossible to replicate that condition, airflow temperature evolutions can diverge significantly with respect to the ideal step variation. An analytical solution for each temperature variation cannot be determined since the flow temperature evolution is not known beforehand. For this reason, several methods for the flow temperature approximation were developed by different authors [17]. In this contribution, the Duhamel

superposition method is used. This approach is based on the discretization of the flow temperature evolution in a series of steps, in order to be able to use the solution correctly 2.16. In this way, the new solution of the Fourier equation can be written as:

$$T_s(t) = T_0 + \sum_{i=1}^{n} \left[1 - \exp\left(\frac{h^2(t-\tau_i)}{\rho c k} \right) \operatorname{erfc}\left(h\sqrt{\frac{t-\tau_i}{\rho c k}} \right) \right] (T_{b,i} - T_{b,i-1}) \tag{2.18}$$

From Fig. 2.8 it can be noticed that a thick discretization allows to better approximate the temperature evolution, at the expense, however of the computational time.

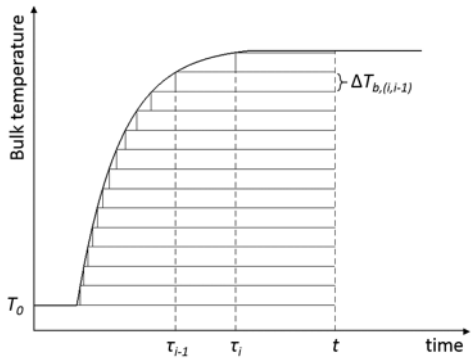

FIGURE 2.8: Duhamel superposition method scheme.

Chapter 3

Test rig design

3.1 Loading structure

The loading structure is composed by square steel tubes (cross section of 50×50 mm), welded together in a parallelepiped shape. In order to give more rigidity to the structure, supports are welded to the main frame and fixed to the ground by means of bolts.
The electric motor support is integral to the loading structure simplifying the transmission system. The support is composed by a steel plate on which the electric motor (5 kW) can be bolted and two slides that supports the plate. The latter can be moved horizontally in order to ensure the correct tension to the transmission belt, and allow the maintenance of the transmission components.
On the top of the loading structure is bolted a steel plate on which the seats for two bearings have been obtained. These two bearings allow the rotation of a hollow shaft that will transmit the rotation to the rotating frame. The shaft is hollow in order to allow the passage of the process air flow from the fan located on ground, and the test section mounted on the rotating facility. An electro-fluidic joint completes the loading structure. This device provides for electrical supply and signal connections to the rotating equipment by means of 32 slip rings ensuring, in this way, a constant physical connection between the rotating shaft and a stationary part integral to the steel frame in which are realized all the power and signal wiring.

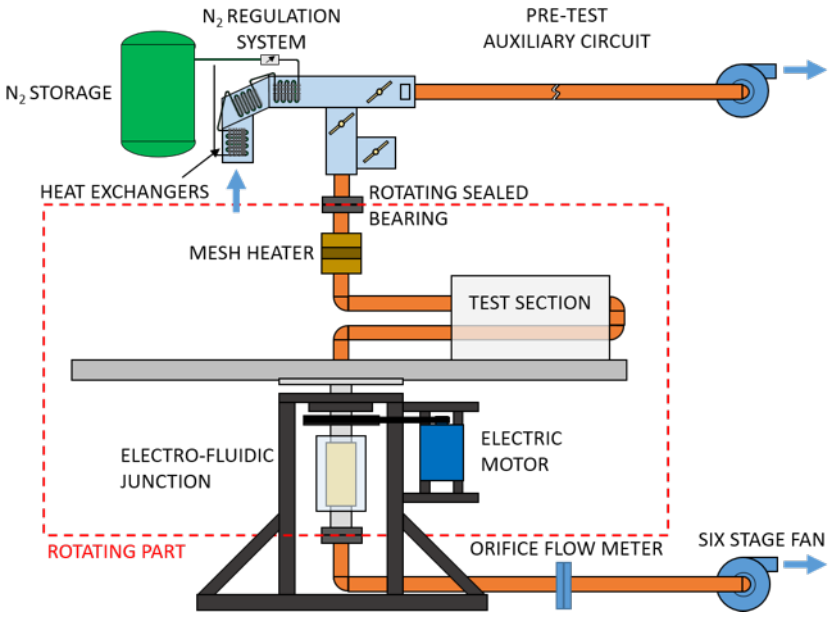

FIGURE 3.1: Air circuit sketch.

3.2 Air circuit

The peculiarity of the air circuit reported in Fig. 3.1 is that it has been designed in order to allow the airflow to either increase or decrease in temperature without serious modifications to the plant scheme.
Hence, air is sucked from the ambient into the circuit by a six stage fan; flow is drawn firstly in an air conditioning section which comprises: the air-nitrogen heat exchangers (used to cool down the process air), a set of remotely controlled valves necessary to recreate an abrupt change of the flow temperature and finally a mesh heater (used to warm up the process air). The treated air is routed into the test section and then collected into return pipes through the rotating joint, where it passes through a hollow shaft to the flow measurement section located just upstream the six stage fan. As can be noticed the more complex part of this circuit is the air conditioning section. In Fig. 3.2 is reported a detail of this section, reporting the main components of the cooling system, namely N_2 storage, heat exchangers, and control valves unit.
As said before the first part in which the air flow runs into is the cooling system. The main reasons that pushed for the use of a N_2 based cooling system instead of more conventional chiller units are the wider range of working conditions easily achievable and the overall reduced cost. The natural drawback of this choice is that a dedicated design has been required for both system components and control devices.
The heat exchanger unit is composed by a rectangular channel in which three fin and tube heat exchangers are installed in sequence and are supplied with liquid nitrogen from a 500 liter reservoir. Liquid nitrogen flow rate is controlled by a remotely driven gate valve and it is regulated by a needle valve. Additional automatic valves are installed in the nitrogen pipes for safety reasons in the event of a cryogenic leak.
Ambient air flows through the first heat exchanger, which has a tighter fin pitch and a wider cross sectional area with respect to the other two heat exchangers. Air starts to cool down to about 5°C, hence the great part of the air humidity content can condensate. The nitrogen is initially fed to the 3^{rd} heat exchanger in the unit, then the 2^{nd}, hence, being the coldest, they have the task to chill the air down to the minimum allowable temperature (about -80°C) and to extract the remaining water content from air that freezes on the heat exchanger fins. A wide fin pitch helps to prevent a blockage caused by frost.

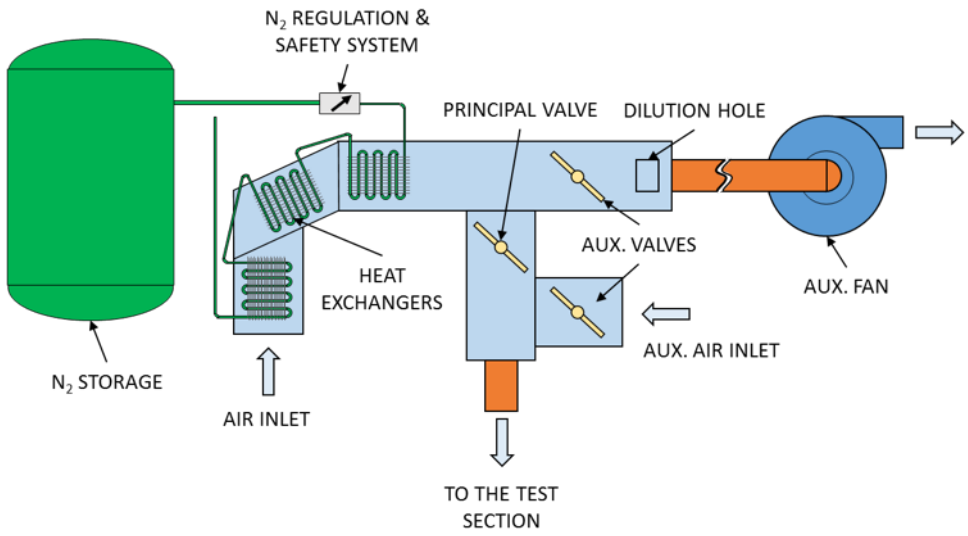

FIGURE 3.2: Nitrogen system sketch.

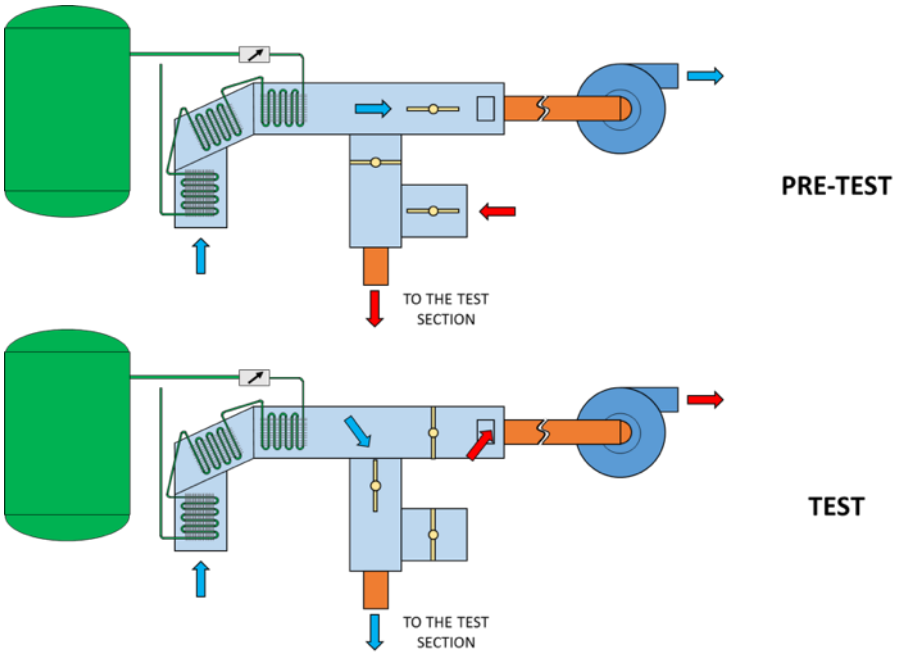

FIGURE 3.3: Valves system operating principle.

The switching valves unit, shown in Fig. 3.2, is located in between test and heat exchanger sections, and is necessary in order to impose the temperature step to the cooling air. The unit comprises three pneumatic valves remotely controlled, which enables two working conditions: pre-cooling and test phases.
In the pre-test phase both auxiliary valves are open while the principal one is closed. In this way, the test rig and nitrogen system are decoupled. Ambient air flows through the auxiliary inlet into the test section in order to reach initial isothermal steady conditions. Meanwhile, an auxiliary fan sucks ambient air through the heat exchangers in order to cool down the system and reach target conditions for the experiments.
The simultaneous switching of the three valves (auxiliary valves close, principal valve opens) set the test phase starting point and air chilled by the heat exchanger flows through the test section producing the temperature step. When the auxiliary valves are closed, a dilution hole in the auxiliary line prevents a vacuum situation in the valve system that

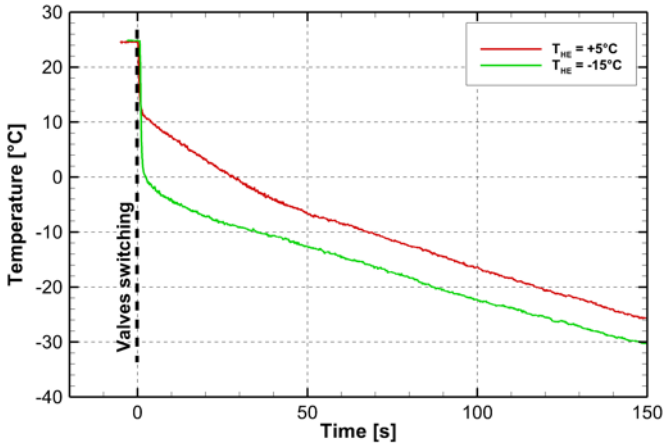

FIGURE 3.4: Achievable temperature steps at the inlet of the test section (Hot case).

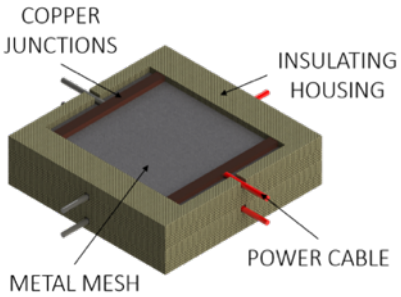

FIGURE 3.5: Mesh heater sketch.

can be source of leakage or structural failure.
Figure 3.4 shows examples of the achievable temperature profile at the position in the rotating arm where the test section inlet will be located. Two profiles have been obtained with different settings of the cooling system, which in turn results in different temperatures at the exit of the heat exchangers (T_{HE}).
When a raise in the flow temperature is needed, a device called a mesh heater can be easily installed in the air circuit as depicted in Fig. 3.5.
This device (Fig. 3.5) is formed by four supports made up of Bakelite, in which is machined a housing for a very thin metal mesh. This mesh is fed by an AC power supply in order to heat it by the Joule effect. Power supply, and then a uniform heating of the metal mesh is guaranteed by the use of copper tensioners on which the power cables are tinned.
In Fig. 3.6 are reported again the achievable temperature evolutions when the mesh heater is used. Comparing these temperature evolutions with the previous ones it can be clearly noticed that the system with the mesh heater has the fastest response allowing to obtain temperature evolutions closer to the ideal step. In the first above-mentioned configuration, the cooled fluid before entering the test section, must pass through the valve section. This passage, lengthens the air path with respect to the configuration with the mesh heater, in fact contributing to dump the temperature step. However, as will be seen later in the discussion, this dumping effect has no particular effect on the measurement.

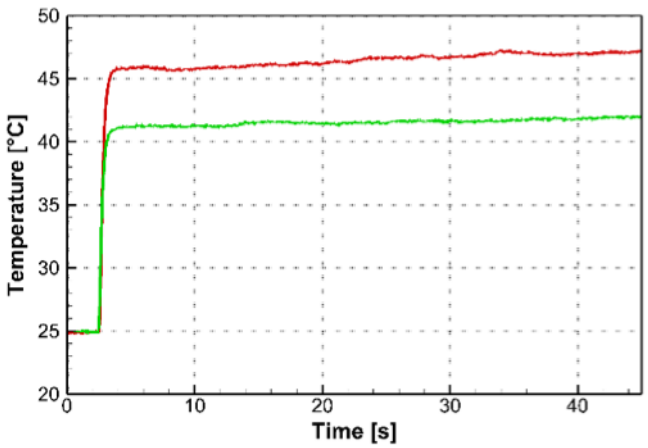

FIGURE 3.6: Achievable temperature steps at the inlet of the test section (Cold case).

3.3 Acquisition system

The acquisition system comprises all the systems that are used during pre-test and test phases in order to allow:

- the synchronous acquisition of the images of the investigated area and the temperatures of the air flow;
- the acquisition of pressure data along the test section;
- the control of the test parameters (Reynolds number, rotation number).

In order to ease the reading, the acquisition system can be divided in two main categories, on-board and on-ground instrumentation.

3.3.1 On-board instrumentation

Temperature acquisition
Bulk flow temperature variation inside the test section is measured using K-type thermocouples in order to guarantee a good accuracy in the temperature range between $-90°C$ and $+30°C$. Thermocouples signals are acquired by a National Instruments cRIO (Fig. 3.7a) with two NI 9213 thermocouple modules (Fig. 3.7b). Each of these modules allows the acquisition of a maximum of 16 thermocouples at a sampling rate up to 75 Hz. This acquisition rate is sufficiently high to ensure a good temporal discretization of the temperature evolutions.

FIGURE 3.7: NI cRIO (a), NI 9213 module (b).

A quick response to temperature variations is necessary for the measurement technique developed in this work, hence a simple procedure for the choice of the best suited junction diameter has been developed. Thermocouples with different hot junction diameters were placed inside the main flow of a jet created by means of a nozzle (see Fig. 3.8a). Thermocouple readings are recorded during the imposition of a temperature variation to the air flow generated by means of a mesh heater. Fig. 3.8b reports the temperature evolutions for the three investigated hot junction diameters: 0.05 mm, 0.075 mm and 0.2 mm.
As can be expected the thermocouple with the thinner junction has the fastest response to the temperature variation. Time response has been evaluated as the time necessary to reach the 85% of the final value of temperature. With this in mind time delays between the thermocouples with thicker junction and the thinner one can be evaluated. In Tab. 3.1 are reported the values of time corresponding to the time response definition above mentioned, and the delay in percentage for each thermocouple, using as reference time

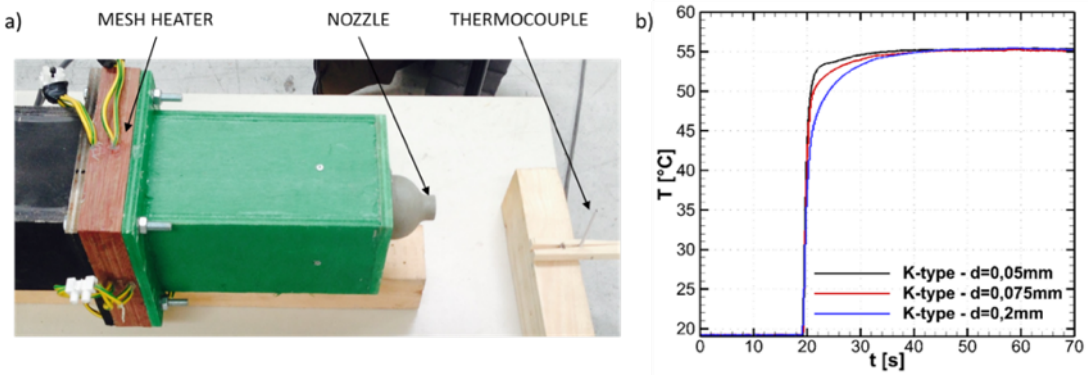

FIGURE 3.8: Experimental setup for TC choice (a), temperature readings (b).

TABLE 3.1: Time response evaluation.

d [mm]	t [s]	ϵ [%]
0.05	20.63	7.7
0.075	20.94	9.3
0.2	23.64	23.4

the initial time (when the temperature starts to raise) t_i=19.15 s. Limited availability and higher cost of the d=0.05mm junction, together with a no significant improvement of the response time leads to the choice of the d=0.075 mm junction.

Pressure acquisition
A 16 channel pressure scanner (NetScanner System mod.9116 in Fig. 3.9) is used to monitor and acquire pressure signals inside the test model and in specific locations of the air circuit. The pressure scanner range is 25 mbar with respect to a reference pressure, which can reach a maximum value equal to 100 mbar. The data acquisition is synchronous with temperature acquisition thanks to a TTL signal generated by the National Instrument cRIO. The pressure scanner is mounted as part of the rotating equipment, as close as possible to the rotation axis, which is aligned with the transducers axis. In this way, the pressure scanner readings are not affected by the centrifugal forces due to rotation.

FIGURE 3.9: NetScanner System mod.9116.

Vision system
The vision system can be divided in two main categories: the first focused on the image acquisition, the latter related to the illumination system.

- *Image acquisition system*. The key features that the cameras must satisfy for the specific application and that drove the device selection are listed in the following.

  – cameras have to be mounted on board the rig rotor, hence their size has to be minimal, in order to reduce weight and encumbrance;
  – a strict constant frame rate is required. This requirement can be met only with externally triggered cameras;
  – reconstruction of the color signal history of each pixel of the image for the whole duration of the experiment requires constant camera settings (particularly exposure time and channel gains), hence the choice must focus on cameras with customizable settings;
  – optics properties have to be taken into account as well. The restricted distance between the test section and the cameras leads to the use of wide angle lenses. Commercial compact cameras are mainly provided by non-customizable optics characterized by fisheye lenses, hence the need for custom optics that ensure a reduced image distortion with respect to fisheye lenses and customizable iris and focus settings.

  With these requirements in mind, two Basler acA1300-60gc (Fig. 10) cameras were selected for use, with a dedicated camera control software developed in LabVIEW.

  Data storage is another consideration in the selection of the vision system. For example, the resolution of this camera (1280×1024) and has bit depth of 24, meaning that each R, G, B signal have 8 bit available for storing data. With this data it is easy to estimate a size of an image of about 4 MB. Assuming a test duration of 2 minutes and an image acquisition at a constant frame rate of 25 Hz (typical test parameters), the amount of image data can be estimated at about 12 GB, hence the necessity of a fast and large memory support is clear. For these reasons, in the present design, the cameras are connected to a fan-less pc mounted on board the rotor that has the double function of: storing the acquired images and running the control camera software.

- *Illumination system*. Uniform and adequate illumination of the measurement area has to be guaranteed, hence the lamp choice and their positioning has to be made taking into account: the minimization of the radiative effect and the level out of the light intensity along the measurement surface.

FIGURE 3.10: Basler acA1300-60gc with C-mount lens.

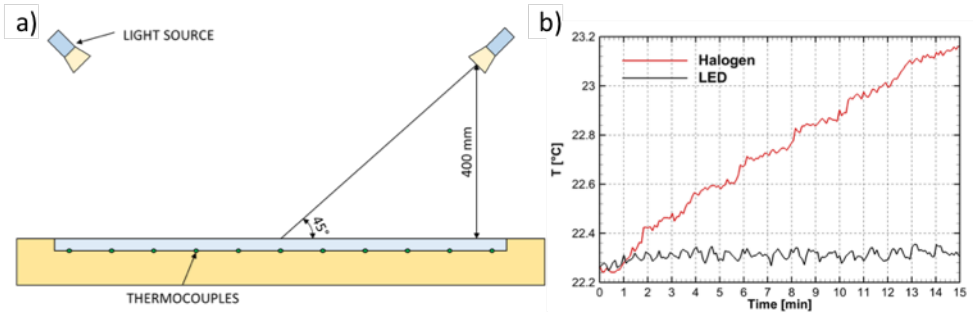

FIGURE 3.11: Experimental test for infrared emission evaluation: experimental setup scheme (a), temperature evolution (b).

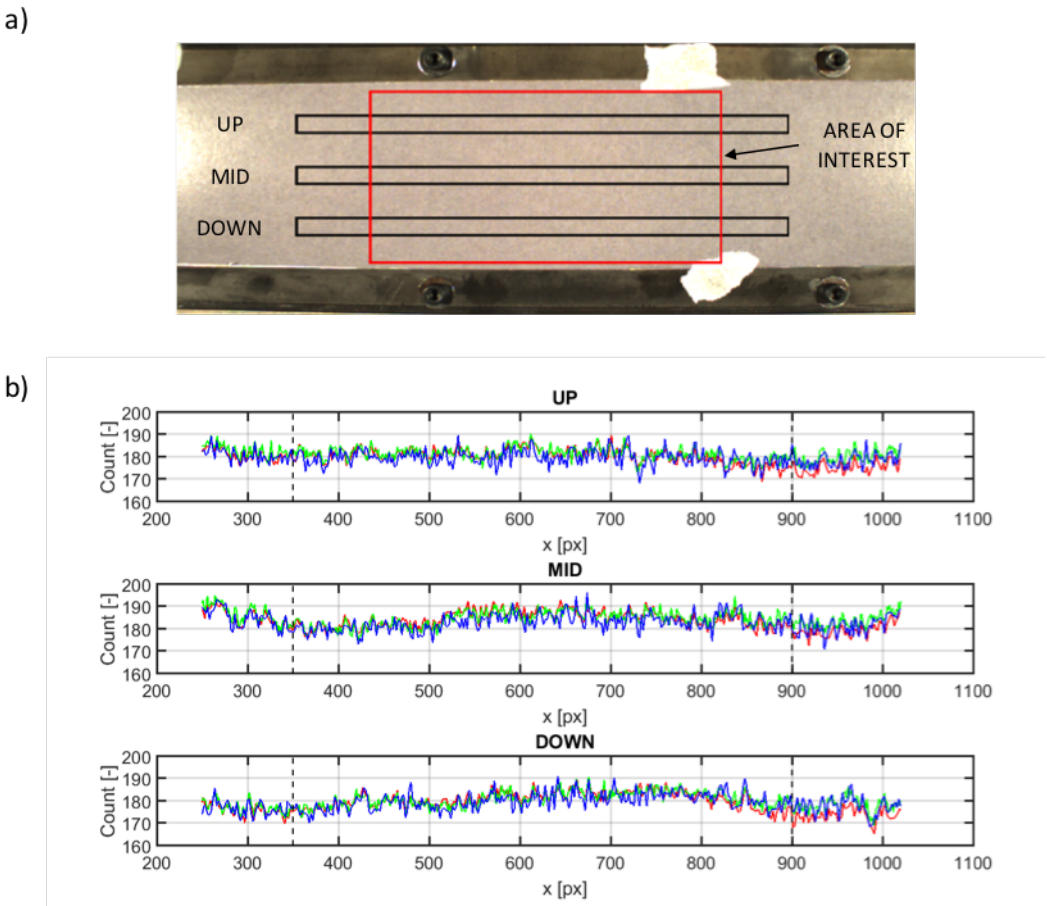

FIGURE 3.12: Example of uniform illumination: acquired image (a), signal intensity profiles (b).

Two different types of lamp have been considered at first: halogen and LED. In order to decide which lamp type is the best suited for this application, it is necessary to evaluate the infrared emission of both lamps. In order to evaluate this parameter, an experimental procedure has been adopted. In Fig. 3.11a is reported a sketch of the experimental apparatus used for the purpose. A Plexiglas plate ($350 \times 150 \times 12$ mm) is located in a seat ad-hoc milled on the surface of an insulating material. Lamps are placed at a distance between the center of the lamp and the surface of the Plexiglas plate of 400 mm and with an orientation of 45 degrees. Temperature evolutions are recorded thanks to thermocouples embedded inside holes drilled on the Plexiglas plate surface in contact with the insulating material. In Fig. 3.11b are reported the temperature evolutions in correspondence of the central thermocouple (ideal maximum luminance) for the two lamp configuration. As it can be seen, for long exposures the difference between the two types of lamps is significant. Considering the canonical test times for transient applications of LCT (about 2 min) the difference between the two lamp configurations can be considered negligible. However, in order to avoid any problem related to radiative effects, the choice fell on LED lamps.
Concerning the necessity of having a uniform illumination of the measurement surface, an aluminum struts frame integral with the rotating arms has been designed in order to allow the correct light positioning for different test section geometries. An exemplification of uniform illumination is given in Fig. 3.12, where an image of a color calibration target placed on the measurement surface is reported (Fig. 3.12a). The R, G, B mean signal intensities are evaluated for three rectangular areas: up, mid and down and reported in Fig. 3.12b. As it can be seen, the area of interest (between the dashed lines in graphs) presents a flat trend of the intensity signals in every evaluated section, meaning that the lamps are correctly positioned.

Triggering system
A perfect correspondence between images and thermocouple readings is required in order to reconstruct the correct temperature field of the measurement area for every instant of the test duration. For this reason, a unique triggering signal is used to clock both acquisitions of Ni cRIO and cameras. This signal is generated by a NI myDAQ module (Fig. 3.13) connected to the fan less pc.

FIGURE 3.13: NI myDAQ module.

3.3.2 On-ground instrumentation

Before starting to present the on-ground instrumentation it is necessary to define which parameter has to be monitored and controlled during the test.
The heat transfer process in a rotating cooling channel is dominated by the following non dimensional parameters:

$$Nu = f(Re,\ Ro,\ Bo,\ Pr,\ Ma) \tag{3.1}$$

Heat transfer distribution obtained from tests carried out on a scaled model can be projected to a real application only if similarity of these parameters is ensured between the experiment and real application.
The dependency on both Prandtl and Mach numbers can be neglected, since rig and real applications are working with air in subsonic regimes. The remaining parameters, i.e.: Reynolds, rotation and buoyancy numbers, cannot be set independently to each other, due to their definitions:

$$Re = \frac{\rho\, U_b\, D_h}{\mu} = \frac{\dot{m}}{D_h\, \mu} \tag{3.2}$$

$$Ro = \frac{\Omega\, D_h}{U_b} = \frac{\Omega\, \rho\, D_h^3}{\dot{m}} \tag{3.3}$$

$$Bo = \frac{\Delta\rho}{\rho}\, Ro^2\, \frac{R}{D_h} = \frac{T_w - T_b}{T_b}\, Ro^2\, \frac{R}{D_h} \tag{3.4}$$

$$D_h = \frac{4A}{P} \tag{3.5}$$

where A is the cross sectional area and P is the wet perimeter.
Consequently, in the experimental application, once the technical limitations of the rig have been defined (max rpm, temperature range, available flow rate), a map of possible test conditions is uniquely defined.
As an example, the map in Fig. 3.14, refers to an ideal model of square section of D_h=50 mm, in which the evaluation of the buoyancy parameter Bo is carried out at 700 mm from the axis of rotation.

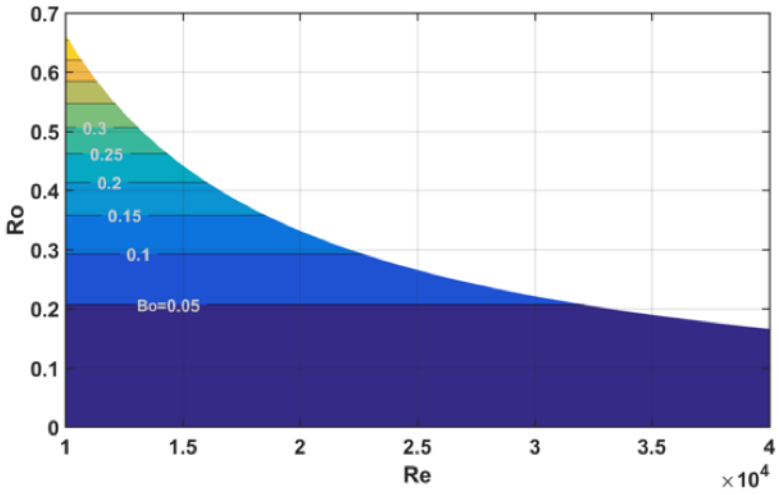

FIGURE 3.14: Example of achievable test conditions.

From these considerations, the parameters that have to be acquired before and during the test execution are:

- mass flow rate in order to evaluate the bulk velocity inside the test section;
- pressure and temperature of the reference location (inlet of the test section) where test control parameters (Reynolds and rotation numbers) are defined;
- rotational speed of the rotating arm for Ro calculation.

An additional temperature should be acquired in correspondence of the exit of the heat exchangers in order to define the start of the experiment.

Test conditions measurements
Mass flow rate that flows inside the test section is measured thanks to an orifice flow meter located upstream the fan as reported in Fig. 3.1. The orifice plate is realized according to the ISO 5167-2 international standards; upstream static pressure and differential pressure are acquired both using calibrated differential capacitive pressure sensors.
Pressure signals in correspondence of the reference location for test parameters evaluation is again acquired with a differential capacitive pressure sensor, while temperature is monitored thanks to a J-type thermocouple immerse in the core flow.
Rotational speed of the facility is measured by means of a photodiode mounted on a ground based tripod. A target integral to the rotating arm passes through the photodiode every revolution (see Fig. 3.15). An external software reads the data acquired by a NI board that samples the photodiode signal at a frequency sample of 100 Hz and elaborates this data in order to calculate the mean rotational speed of the rotating facility. It is clear that this speed is a mean value because can be evaluated just once a time at revolution.
All the data is acquired by a NI cDAQ device equipped with one thermocouple reader module, an analog input module and an analog output module. A LabVIEW interface has been developed in order to allow continuous monitoring and control of test parameters.

System control
Once a test condition is chosen, in order to ensure reliability and repeatability of the results, the test parameters that define the experiment (Re and Ro numbers) have to be kept constant throughout the duration of the experiment.

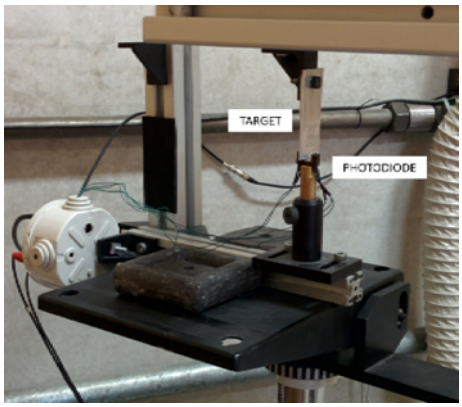

FIGURE 3.15: Photodiode system for rotational speed evaluation.

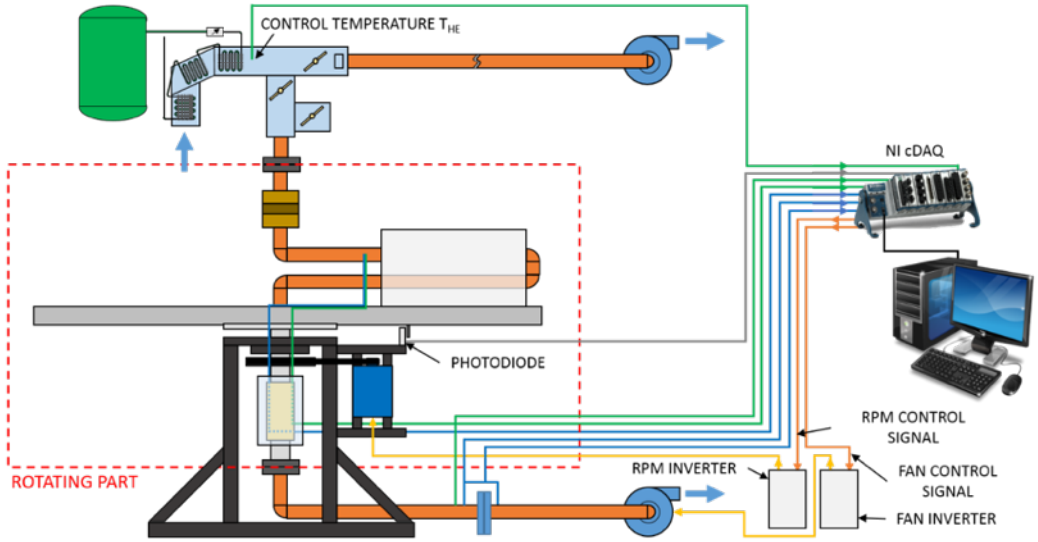

FIGURE 3.16: Control connection sketch.

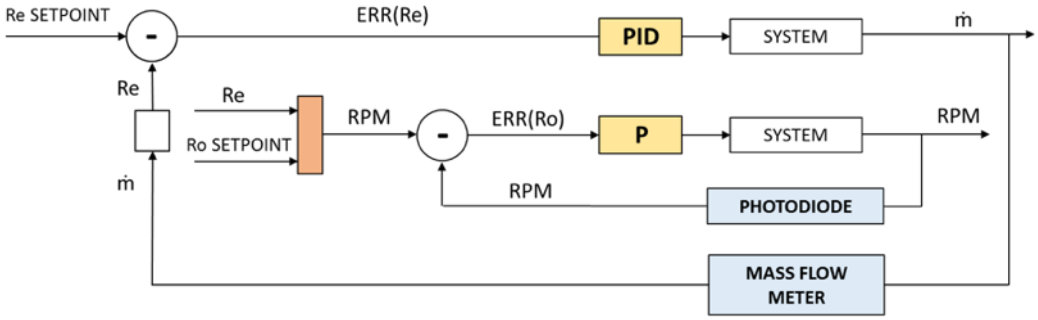

FIGURE 3.17: Control system scheme.

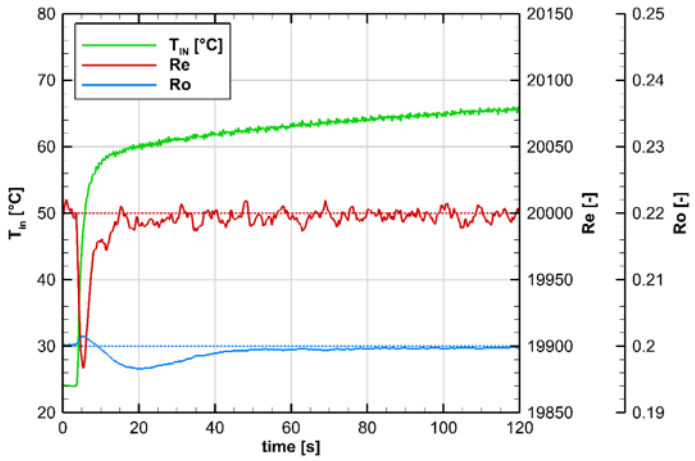

FIGURE 3.18: Example of control system on test parameters.

This is accomplished by a control loop implemented on the NI cDAQ platform that receives input signals about:

- peripheral velocity by sampling the photodiode signal;
- pressure and temperature signals from the orifice flow meter, the data is used by the control software to compute the actual flow rate;
- temperature and pressure values inside the test section measured at the location where the definition of Re and Ro values is made (e.g. inlet of the test section). These values are used to compute the coolant physical properties (i.e. density and viscosity). Signals are delivered to the ground control unit by means of the slip rings.

A sketch of the control system is given in Fig. 3.16, demonstrating the following colors for the connections:

- green for temperatures;
- blue for pressures;
- grey for photodiode;
- orange for output control voltage (0-10V);
- yellow for inverter output.

The output signals of the control loops are the voltage that has to be sent to the inverter that drives the rotation of the rotating arm and the inverter that drives the six stage centrifugal fan, hence control the flow rate.
The concept at the base of the control system adopted is reported in Fig. 3.17. A PID controller is used to control the flow rate, because of the quick dynamic response of both the six stage fan and of the measurement systems involved in the control (pressure and temperature at the orifice).
Conversely, a proportional controller is sufficient to regulate the rotational speed in view of the high inertia of the rotating arm (due to its weight of about 200 kg) and also because the rotor velocity has to decrease monotonically during the test.
An example of how the control system works is reported in Fig. 3.18. It can be seen that the control systems acts on the test parameters throughout the test keeping them constant, within a 0.7% margin of error for the Ro and 0.2% for the Re, after an initial overshooting due to the abrupt change in flow temperature (see as an example the variation of the channel inlet temperature T_{IN} in Fig. 3.18).

3.4 Weight balance procedure

The implementation of a weight balance procedure is necessary to ensure a safe and proper usage of the rotating rig. Before starting to run the experiments, the correct counterweight mass and location must be defined in order to make the structure both statically and dynamically balanced. During rotation the balance condition can be associated to the counterweights configuration that minimize the displacements of the steel load bearing structure. In order to define a first attempt configuration a procedure like the one reported below can be used. Once the counterweight mass and location are defined it is possible to verify the balance of the structure during rotation by means of optical devices that measure the displacements of pre-determined locations of the load bearing structure. This information is used to adjust the counterweight configuration until the achievement of a sufficient balancing condition. In the following is reported the procedure used in one of the experimental campaigns.
The definition of a first attempt counterweights configuration (location and the weight) in order to balance the test facility in both static and rotating conditions can be performed by setting a system of equilibrium equations for the whole structure.

TABLE 3.2: Weights and coordinates - Test section side.

Component	**m [g]**	x_G **[mm]**	y_G **[mm]**	z_G **[mm]**
Inlet	515	93	-3	160
Channel + Insulation	5090	691	-9	148
1^{st} support + screws	855	258	12	143
2^{nd} support + screws	825	560	13	145
3^{rd} support + screws	1055	1126	11	122
Threaded rod	370	685	-5	211
Radial support (wood)	664	1205	-6	126
Angular support	276	1229	0	111
1^{st} radial support (alum.)	890	1239	0	139
2^{nd} radial support (alum.)	221	1303	0	77
Outlet joint	312	1287	66	175
Outlet pipe	836.6	664	160	210
Outlet flange	350	10	82	128
Vision system	1414	925	-230	59
Lower angular	600	1245	0	17.5

TABLE 3.3: Weights and coordinates - Instrumentation side.

Component	**m [g]**	x_G **[mm]**	y_G **[mm]**	z_G **[mm]**
Router	980	358	-112	128
PC	1945	134	-25	209
cRIO	2045	336	97	150
Cables	3593	750	0	59
Counterweights supports	1030	1281	0	121
Target photodiode	97	1312	0	11

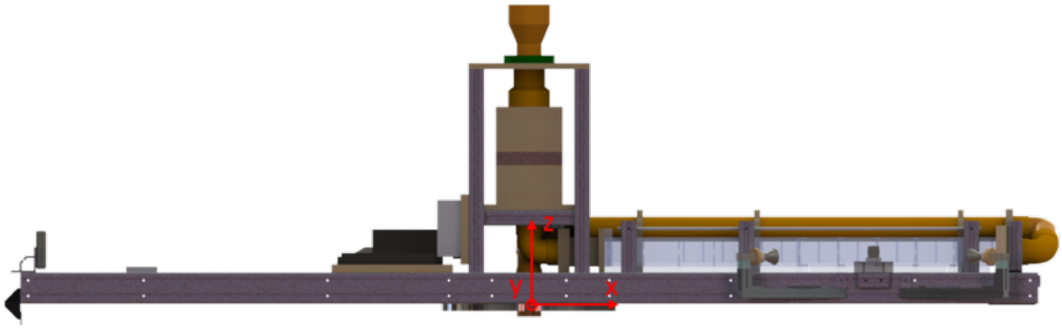

FIGURE 3.19: Weight balancing coordinate system.

This is possible only if the weight and the location of the center of mass of all the components of the facility are known. The locations of the center of mass of all components are measured with respect to the origin of an arbitrary reference system. In this application the reference system is located in the middle of the test facility as represented in Fig. 3.19. As an example in Tab. 3.2-3.3 is reported the list of all the components that compose the rotating facility divided in two main categories: components located on the test section side (TS) and components located on the instrumentation side (IN). Once all this information is known, it is possible to solve the equilibrium equation.
The general form presented here,

$$\begin{cases} F_x = 0 \\ F_y = 0 \\ M_z = 0 \end{cases} \tag{3.6}$$

can be detailed for the case, obtaining:

$$\begin{cases} \sum_i m_i \, g \, x_i + m_{cw} \, g \, x_{cw} = 0 \\ \sum_i m_i \, g \, y_i + m_{cw} \, g \, y_{cw} = 0 \\ \sum_i m_i \, \Omega^2 \, z_i + m_{cw} \, \Omega^2 \, x_{cw} \, z_{cw} = 0 \end{cases} \tag{3.7}$$

The first two equations, if considered in the canonic form here reported, ensure the static equilibrium of the system. Instead, if the gravity acceleration (g), is replaced by the angular velocity (Ω^2) these equations become an equilibrium of centrifugal forces. The solution of these equations impose that, in rotation, the radial loads on the bearings are balanced.
The third equation is already written considering the momentum generated by the centrifugal forces that acts on the different components of the system. This equation, once solved, allows the estimation of the z-position of the counterweight that ensures that rotation does not generate misalignment forces on the bearings.
As it can be seen, this system of equations is composed by three equations and four variables: m_{cw}, x_{cw}, y_{cw} and z_{cw}. The system can be solved imposing one of the variables. In this case it has been decided to impose the location of the counterweights in correspondence to the maximum radial distance available. Hence with x_{cw} = 1245 mm it results that:
$m_{cw} = 4738 \; g$
$y_{cw} = -23 \; mm$
$z_{cw} = 155.3 \; mm$

As said before, once the counterweight configuration is defined, the verification of the balance of the whole system in rotation is needed. Different techniques can be used: cameras, Laser triangulation displacement sensor, ad-hoc adapted PIV measurement system.

- *Cameras*: a video camera is mounted on a ground based tripod and is used to record the test facility during it's rotation. The analysis of the recorded video allows a qualitative estimation of the macroscopic displacement of the structure. In Fig. 3.20 three video frames extracted at different times are shown, they represent different rotational conditions. In each frame, a typical feature of the rotating frame is used as reference in order to estimate the vertical displacement of the frame.

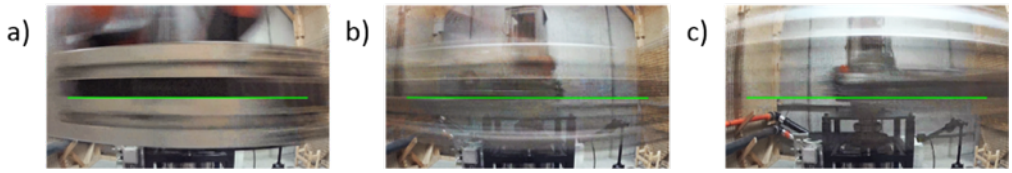

FIGURE 3.20: Qualitative estimation of the displacement of the rotating structure at different rotating conditions: 5 rpm (a), 100 rpm(b) and 250 rpm (c).

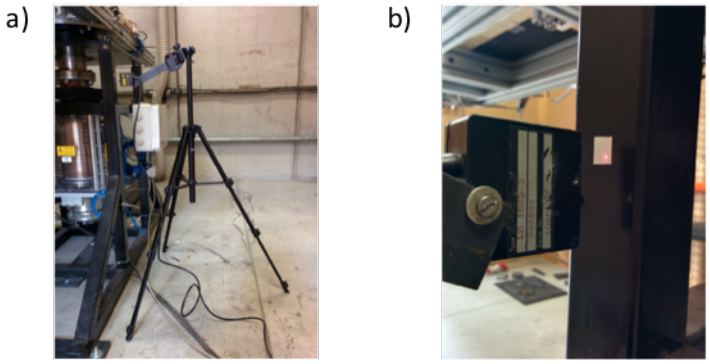

FIGURE 3.21: Displacements measurement with laser triangulation.

- *Laser triangulation displacement sensor*: a Micro-Epsilon LD-1605-2 can be used to measure the horizontal displacement of the load bearing structure. This device makes use of the laser triangulation principle. A laser diode projects a visible light spot onto a target integral to the measurement structure. The signal generated by this device is visualized by an oscilloscope that helps to determine the amplitude of the measured displacements. The only drawback of this measuring method is that with this device it is not possible to correlate the displacement measure with the related position of the rotating structure. In Fig. 3.21 is shown the measuring configuration used with the laser sensor kept at a distance of about 20 mm from a target glued on the steel frame.

- *Laser sheet measurement system*: a laser generator (NewWave-SoloPIV) projects a laser sheet pulse with a thickness less than 1 mm onto an edge of the load bearing structure. A high sensitivity cam (Sensicam PCO) located orthogonal to the laser sheet is used to record, during the rotation of the facility, the reflection generated by the laser that hit the surface of the load bearing structure (visible in Fig. 3.22). The emission frequency of the laser sheet is synchronized with the frequency of rotation of the rotating facility, measured by a photodiode triggered by a target

mounted on the facility. In particular, it is possible to set a delay in the output of the laser with respect to the passage of the target through the photodiode. By doing this it is possible to correlate the deformation of the structure obtained from the analysis of the images acquired by the high sensitivity camera, with the different angular position of the rig and then it is possible to refine the counterweight configuration previously defined.

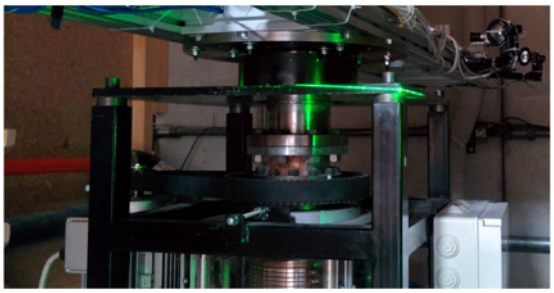

FIGURE 3.22: Displacements evaluation with laser sheet and high sensitivity camera.

3.5 Liquid crystal calibration rig

A typical ex-situ calibration slab is used to perform the calibration of liquid crystals. More complex in-situ calibration is not required since narrow banded liquid crystals will be used in the transient liquid crystal thermography and, therefore, accuracy issues related to viewing angle and illumination are negligible. Two different calibration rigs were developed and realized in order to calibrate liquid crystals with activation temperatures higher and lower than ambient temperature.
In order to calibrate cold liquid crystals (activation temperature lower than ambient temperature) a setup similar to the one reported in Fig. 3.23 has been adopted. The main issue in this type of calibration is to ensure the low activation temperature of the liquid crystal, which can be very close to 0 °C.
To accomplish this, on one side of an aluminum slab a cold sink is generated by using two 100W Peltier cells, connected in series (Fig. 3.23). To make them work close to the maximum efficiency, the hot side is cooled by means of a finned plate water heat exchanger. The hot sink on the other side of the aluminum slab is obtained with a similar set-up as the cold sink. By acting on the DC supply voltage to the various Peltier cells, different gradients can be re-created inside the metallic slab with a temperature range of -15 °C/+20 °C.
The liquid crystals to be calibrated are sprayed on a Plexiglas slab and then covered with black paint to increase the contrast. The Plexiglas slab is pressed tightly on the aluminum slab in order to place in contact the two surfaces and to avoid insulating air bubbles.

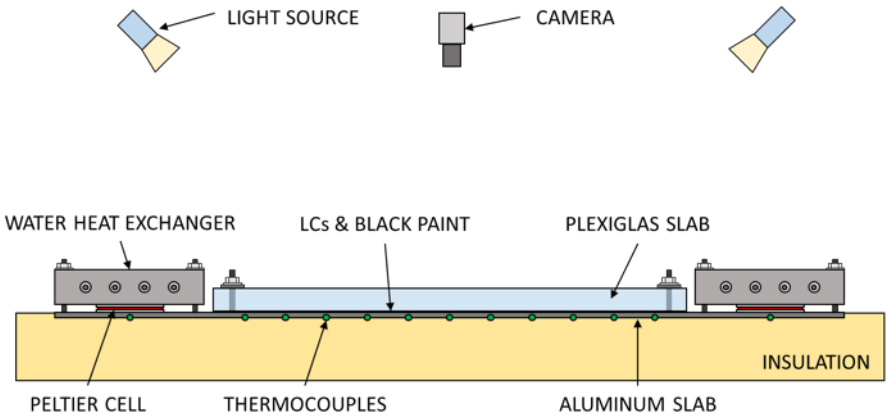

FIGURE 3.23: Cold liquid crystals calibration plate.

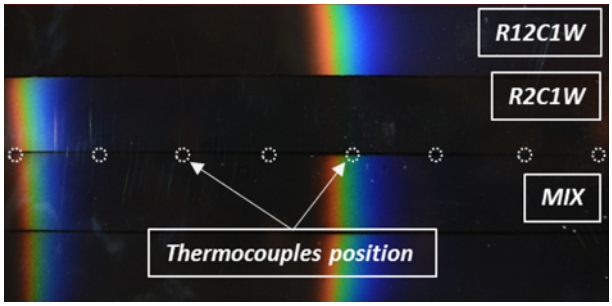

FIGURE 3.24: Calibration image.

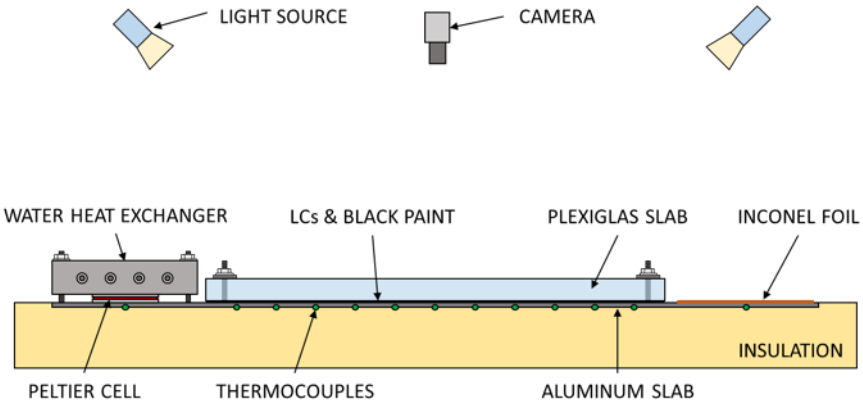

FIGURE 3.25: Hot liquid crystals calibration plate.

Under the plate, twelve K-type thermocouples are installed in known locations, inside holes drilled on the lower surface of the aluminum surface with a depth that will get as close as possible to the surface on which the liquid crystals are painted. These thermocouples are used to acquire the temperature of the aluminum surface that is assumed to be representative of the liquid crystals temperature.
To acquire the image of the calibration area, a camera and a lighting setup similar to the test rig setup is used. A typical image of cold liquid calibration is reported in Fig. 3.24, where two different liquid crystals are sprayed on the same Plexiglas slab.
In order to perform calibration of hot liquid crystals (activation temperature higher than ambient temperature), a setup similar to the one above mentioned has been adopted. As can be seen in Fig. 3.25, in order to achieve high temperatures, the hot sink is generated by means of an Inconel foil placed on one side of the aluminum slab and supplied by an DC power supply. As in the previous configuration, the cold sink is generated by using Peltier cells and a finned plate water heat exchanger; acting on the two power supplies different temperature gradients in the range of +20 °C/ +50 °C can be achieved.

Chapter 4

Data processing

Data obtained from the experimental tests has to be managed in order to evaluate the heat transfer coefficient on the measurement surface of the tested geometry. Due to the huge amount of data, hence the high computational costs, an in-house software has been developed. The software receives in input the stream of images of the tested surface, the readings of several thermocouples located inside the test section, an image of the calibration surface and the related temperature readings in order to perform liquid crystal calibration.
The structure of the software can be imagined as five separated blocks as reported in Fig. 4.1. The first is dedicated to the processing of images with the aim to obtain, from the information contained in each pixel of the images, a map of activation times. In this block is contained a section that takes into account the distortion of the images caused by the usage of short focal lenses and by the Plexiglas by performing an image calibration.
A second block has the task to evaluate the temperature distribution along the whole test section during the entire duration of the experiment starting from the temperature readings acquired in defined locations along the tested geometry.
The third block (violet rectangle in Fig. 4.1), receives as input an image acquired on the liquid crystals calibration rig and the temperature readings acquired during the calibration procedure.

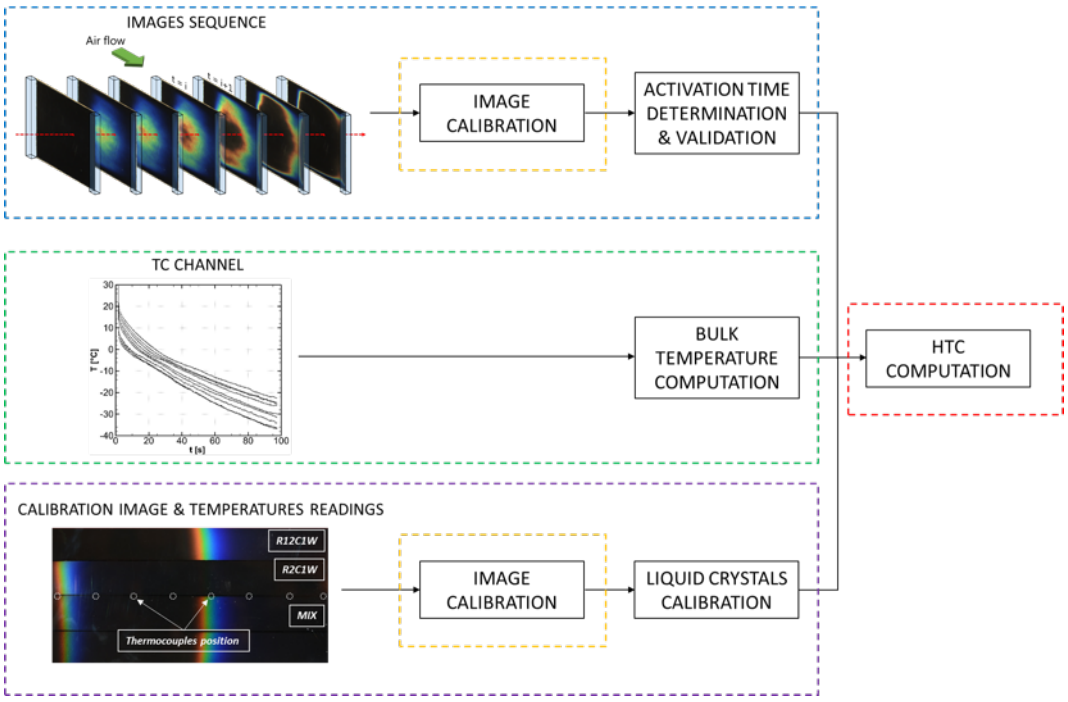

FIGURE 4.1: Working principle of data processing software.

After an image calibration, performed for the same reason previously mentioned, the software computes the activation temperatures of the liquid crystals used during the experiments. Once all the first four blocks are completed, hence are available the activation time map, the temperature distribution and activation temperature of the liquid crystals, the last block can be considered. This block has in charge the computation of the heat transfer coefficient of the measurement surface.
In the following all the software sections will be explained in detail.

4.1 Image calibration

The usage of short focal lenses and the reduced distance between the cameras and the measurement surface is the principal cause of obtaining highly distorted images. In order to avoid this problem, hence to account for lens and Plexiglas distortion, an image calibration procedure has been developed.

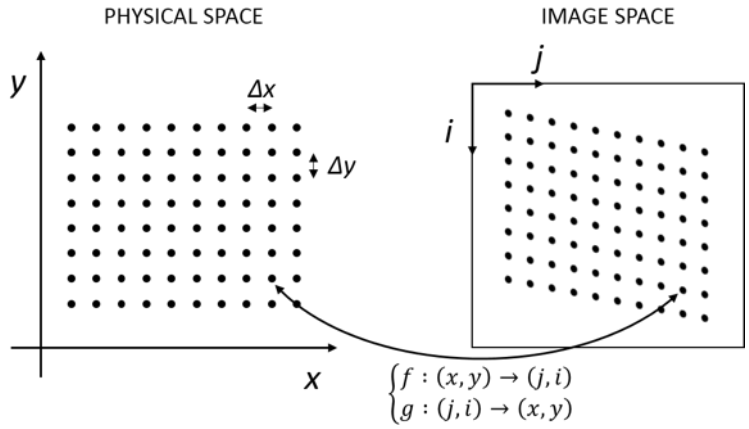

FIGURE 4.2: Image calibration working principle.

This procedure allows to associate the information of each pixel of the acquired image to the correspondent position in the physical space by using a calibration dotted target. The target is designed with circular dots with a diameter of 1.5 mm, rows and columns of the grid of dots are equally spaced and the distance between two consecutive dots is 6 mm.
A sketch of the image calibration is given in Fig. 4.2. On the left of the figure is shown the equally spaced grid representing the calibration target, hence the physical space; on the right is represented an image of the target in which is highlighted a distortion. The developed calibration procedure involves the search, then the identification (in terms of position), of the black dots. Once identified, the coordinates of the dots are used to evaluate the conversion function between the two spaces: physical (dimensions in the physical space are in mm) and image (dimensions in the image space are in px).
In the case of simple test channel geometries (e.g. channel surfaces without fillets or rounded surfaces) the target is placed in contact with the channel inner surface and an image of the target is acquired (Fig. 4.3a). In this way both lenses and Plexiglas distortion are taken into account. In case of complex channel geometry, the placement of the target in contact with the inner channel surface can be difficult. To overcome this problem a two-step procedure has been designed and is basically shown in Fig. 4.3b. The first step is used to account for lens distortion. An image of the dotted grid placed on the model external surface is acquired and a first set of transformation function are evaluated. The

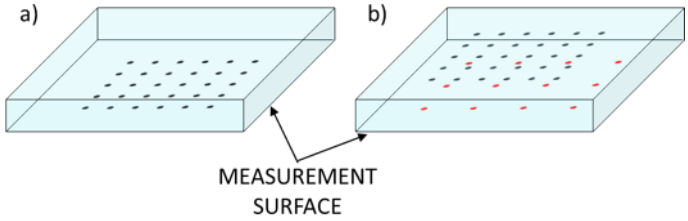

FIGURE 4.3: Sketch of target placement: internal calibration (a), internal/external calibration (b).

second step of this procedure is a refinement that takes into account for the distortion associated to the thick Plexiglas wall of the test section.
The procedure and methodology is basically the same as for the first step but with the difference that dots drawn at known positions on the inner surface of the test section are used as control points.
Once the image of the target is acquired, the image calibration can be carried out. This procedure is performed thanks to an in house developed software that operates in three main steps:

- identification of the calibration dots;
- association of the physical space coordinates (with dimensions in mm) to the calibration points;
- evaluation of space conversion polynomials.

4.1.1 Identification of the calibration dots

In order to detect all the dots of the calibration target, a two dimensional cross-correlation searching method has been used. The image of the target is firstly converted in a gray scale image, then the negative of the gray image is analyzed. This image conversion is performed in order to highlight the dots whit respect to the image background.

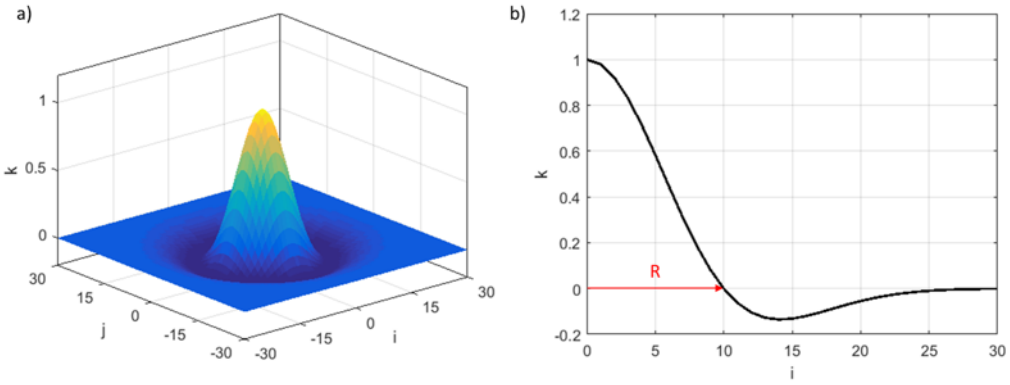

FIGURE 4.4: Mexican hat sample signal.

Since the points to find have a circular shape, a sample signal that can be well compared with the searched shape has to be defined. A Mexican hat function (see Fig. 4.4) is the best suited for this types of shapes. The sample function used is defined by the equation:

$$k(i,j) = \left[2 - \frac{2}{R_h^2}(i^2 + j^2)\right] e^{-\frac{1}{R_h^2}(i^2+j^2)} \tag{4.1}$$

keeping as the only variable parameter the radius R it is possible to correlate different circular dimensions. The cross-correlation acts essentially sliding the sample function along the image. Calculating the integral of the product of the sample signal and the correspondent image information for each position, a matching map can be obtained. The maximum of this map are the points in which the value of the two compared signals best match, hence the center of the dots. At this point, the program starts searching the location of all the maximum higher than a threshold. In order to avoid multiple count of a single dot, when one dot is localized the information related are erased from the matching map. The output of this first step is a list of image coordinates, one for each

dot found, where axial (j) and transversal (i) coordinates are expressed in pixels. As an example, in Fig. 4.5 is reported an image of the calibration target on which the dots are well recognized.

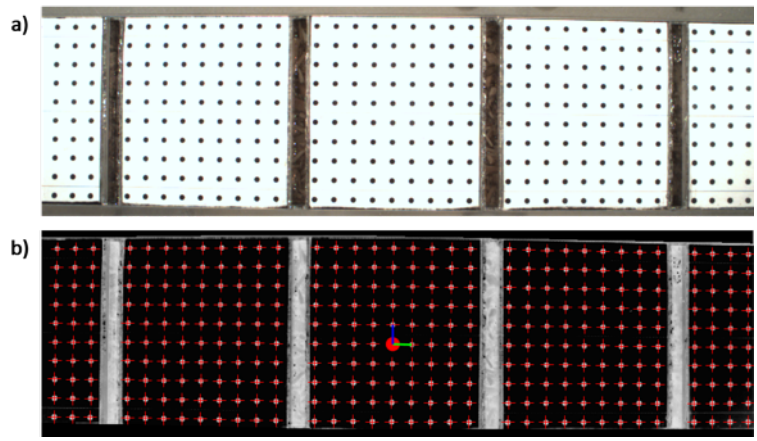

FIGURE 4.5: Dots location: target image (a), processed image (b).

4.1.2 Association of the physical space coordinates to the calibration points

Once every dots of the target is found, the software has to assign each point to the correspondent of a Cartesian grid of points spaced as the points drawn on the target (as drawn in CAD). In order to allow an automatic assignment of the physical space coordinates, even when a dot is missing (e.g. in correspondence of a rib), a dedicated procedure has been developed. The first step is the selection, operated by the user, of the reference dot that will be used as starting point for the coordinates system in the physical space; this definition imply that this point will have as physical coordinates the couple $(0, 0)$. At this point the orientation of the reference system can be defined choosing one point closer to the origin along the axial direction and one orthogonal to the previous one. For these points the software assigns the coordinates $(\Delta s, 0)$ and $(0, \Delta s)$ respectively to the points mentioned above, where Δs is the spacing of the grid in the physical space expressed in mm.
A predictor-corrector method has been developed in order to associate the correct physical coordinates to the related image coordinates (see Fig. 4.6a). Starting from the origin of the reference system a vector is defined, this prediction vector has initial length equal to the distance between the points of the axial reference system previously defined and the direction is the same of the reference system. In order to verify if there are points to assign beyond the reference points, the predictor vector is shifted as reported in Fig. 4.6a and within the image coordinates are found the ones that are included in the circumference of radius R and centered at the end of the prediction vector (guess point location). At this set of coordinates, the software associates the coordinates of real space: the x coordinate is given by the number of shifts of the prediction vector multiplied by the spacing of the dots (Δs), the y coordinate is the same of the previous points.
In case of missing points (Fig. 4.6b), if image coordinates within the finding area are not found, the prediction vector is being stretched to its same length while keeping unchanged the direction. A new finding area is defined and the search of the image coordinate in the area is repeated. In this case the axial coordinate of the physical space is evaluated with the relation:

$$x_c = (n_{shifts} - n_{skip})\, \Delta s \tag{4.2}$$

where n_{skip} is the number of times that the prediction vector is stretched by its length (equal to the number of missing points). The y coordinate of the physical space is the same of the previous points as the previous case. Since this searching method is designed in order to work only for axial shifts of the prediction vector, once a row of image points is completely associated to the correspondent physical space coordinates, the prediction vector is moved back to the origin and shifted on the next row with the origin in the coordinate $(0, \Delta s)$. The searching procedure starts again until all the rows are evaluated.

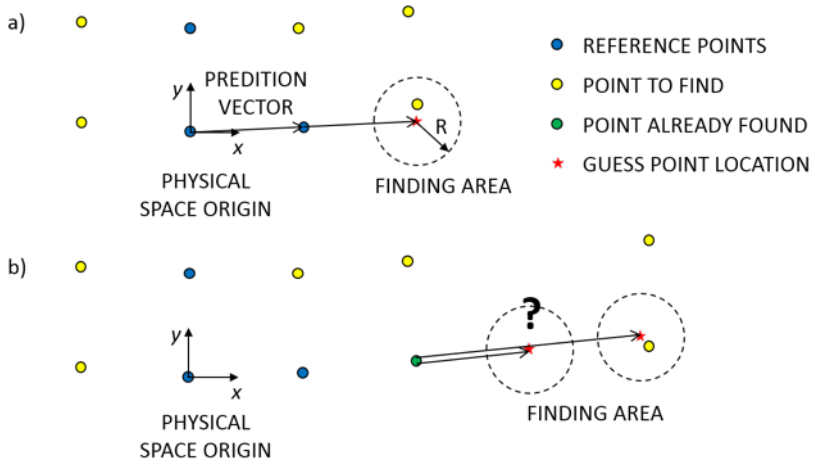

FIGURE 4.6: Procedure for physical coordinates assignment.

4.1.3 Evaluation of space conversion polynomials

The last step of the calibration procedure is the determination of the "transfer functions" that allow coordinate conversion between image and physical spaces as reported:

$$f : (x, y) \rightarrow (i, j) \qquad g : (i, j) \rightarrow (x, y) \tag{4.3}$$

In order to correct the distortions produced by the available optical configuration, it has been verified that polynomial equations can be used without affecting the accuracy of coordinate transformation. Hence the functions 4.3 can be detailed as below:

$$f : \begin{cases} j = A_n(x, y) \\ i = B_n(x, y) \end{cases} \qquad g : \begin{cases} x = A_n^{'}(j, i) \\ y = B_n^{'}(j, i) \end{cases} \tag{4.4}$$

For example, for a second polynomial degree, the coordinate transformation functions are:

$$f : \begin{cases} j = A_n(x, y) = a_0 + a_1\, x + a_2\, y + a_3\, x^2 + a_4\, xy + a_5\, y^2 \\ i = B_n(x, y) = b_0 + b_1\, x + b_2\, y + b_3\, x^2 + b_4\, xy + b_5\, y^2 \end{cases} \tag{4.5}$$

and the opposite

$$g : \begin{cases} x = A_n^{'}(j, i) = a_0^{'} + a_1^{'}\, x + a_2^{'}\, y + a_3^{'}\, x^2 + a_4^{'}\, xy + a_5^{'}\, y^2 \\ y = B_n^{'}(j, i) = b_0^{'} + b_1^{'}\, x + b_2^{'}\, y + b_3^{'}\, x^2 + b_4^{'}\, xy + b_5^{'}\, y^2 \end{cases} \tag{4.6}$$

Given that the coordinates of all points are known from the previous step, the coefficients of the polynomials can be found by the least squares method. The coefficients of the function 4.5 are used in image calibration to transform all the information of the image in the physical space. Conversely, the coefficients of the function 4.6 are used as cross-check

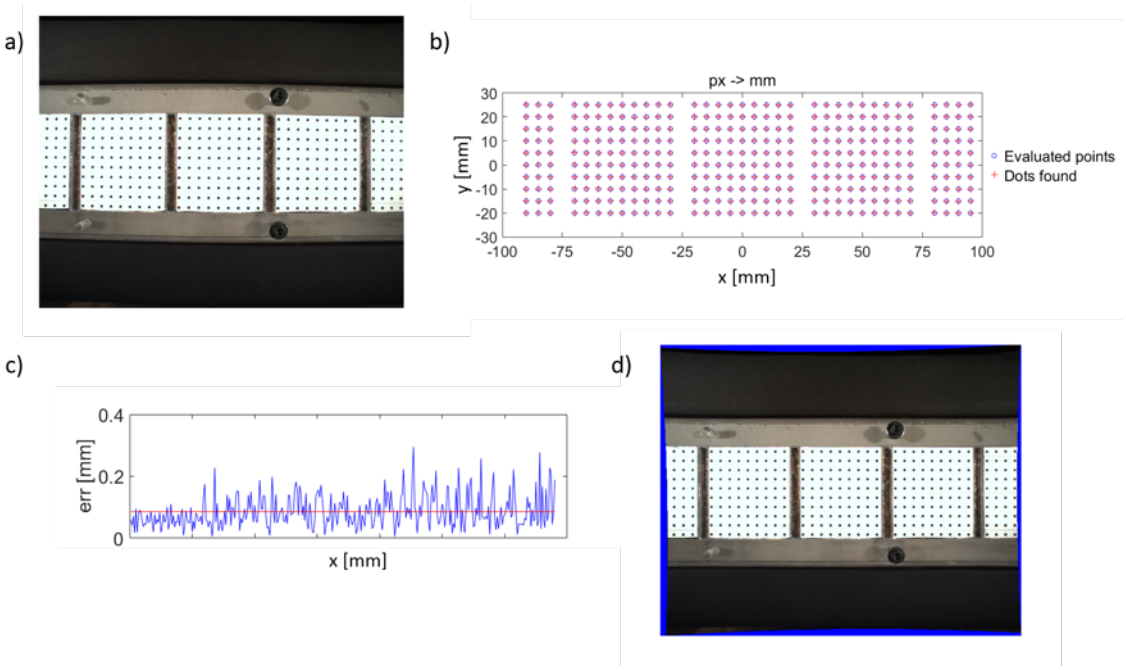

FIGURE 4.7: Calibration procedure: target image (a), dots search (b), error validation (c), de-warped image (d).

of the accuracy of the calibration. As an example in Fig. 4.7 is reported a summary of the calibration procedure.
Figure 4.7a is the acquired image of the dotted target. On the right, in Fig. 4.7b is reported the result of the identification of the calibration dots, with the blue circles representing the coordinates of the cartesian grid (CAD coordinates) and the red cross are the coordinates evaluated with the conversion polynomials.
Figure 4.7c shows the errors in the computations of the coordinates along the image, while the last figure shows the de-warped image where it can be appreciated the consistency of the developed software.

4.2 Image processing

In order to evaluate the activation time of the liquid crystals (defined as the frame, hence the time, in which the color intensity reaches the maximum value), the acquired stream of images has to be analyzed.
Images are acquired in .TIFF format, an image format in which the image can be represented as a matrix of data. The elements of this matrix are called pixels. Depending on the type of color model that is chosen for saving the image, each pixel will contain the information necessary to display the image.
Given the need to search for the instant in which the color intensity of each pixel reaches its maximum, the RGB model is the most appropriate for the purpose. In this model each pixel will then contain the intensity of color information for the three channels: red, green and blue. Each channel is acquired with a color depth of 8 bit meaning that the color intensity is discretized in $2^8 = 256$ levels (0 corresponds to absence of light, 255 corresponds to saturated color).
In view of these considerations, the software has to manage matrices with dimensions $N \times M \times 3$, in which N and M are the dimensions of the image (in this work 1280×1024 pixels) and 3 are the three layers of the matrix that contains the information of the RGB channels. An exemplification is given in Fig. 4.8.

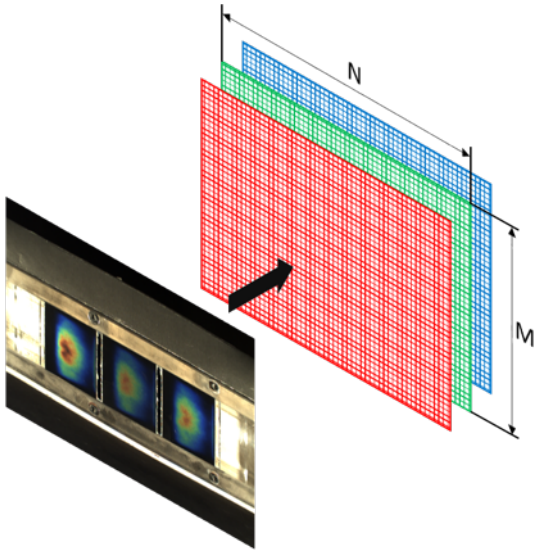

FIGURE 4.8: Example of raster image representation with RGB color model.

4.2.1 Domain definition

A reduction of the computational efforts can be achieved limiting the analysis to the pixels inherent to the measurement surface (the area framed by the camera can be greater than the effective surface covered with the liquid crystals). Different domains can be defined in order to include only the test section surface portions useful for the experiment. The software allows the definition of the domains directly from an acquired image. Fig. 4.9 shows an exemplification of what the user sees after the definition of three domains on a tested geometry.

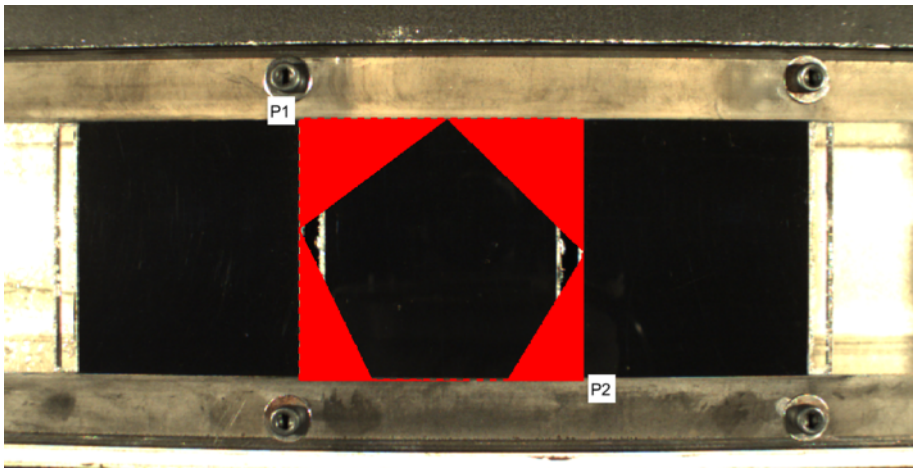

FIGURE 4.9: Domain definition.

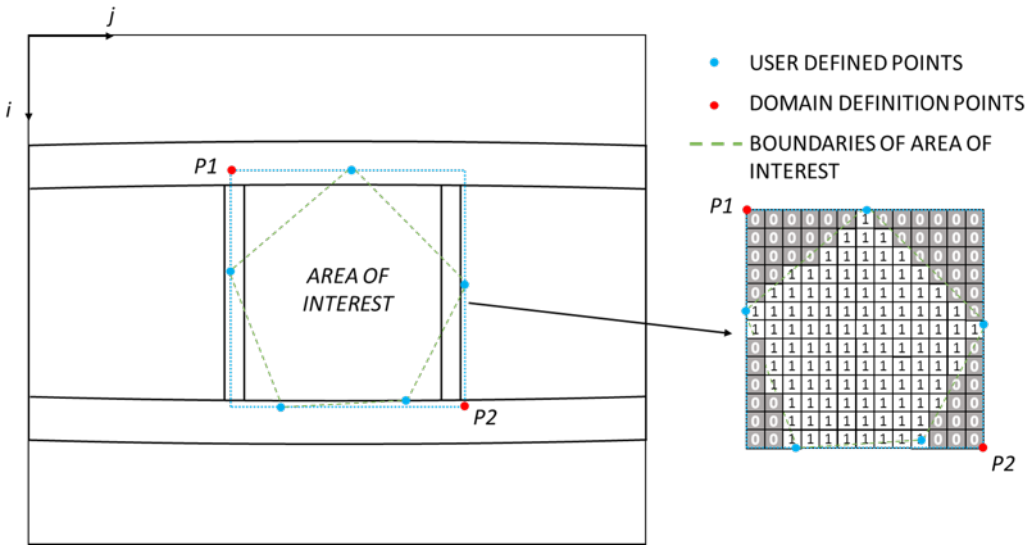

FIGURE 4.10: Area of interest definition.

For each domain a rectangular area is defined as in Fig. 4.10; considering the points selected by the user, points $P1$ and $P2$ are evaluated as follows:

$$\begin{cases} P1 = (\min(j), \max(i)) \\ P2 = (\max(j), \min(i)) \end{cases} \tag{4.7}$$

In order to consider only the pixels belonging to the area of interest defined by the user selected points, a mask is associated to the rectangle. To the point of the mask corresponding to the pixels contained within the area of interest, is associates the value 1. These points will be the only ones that will be later considered for the search of the activation time.
Since the search for the activation time requires the analysis of the evolution in time of the intensity of the three color channels, it is needed to load into the computer memory (RAM) all the information of the pixels contained within the domain. In order to avoid overloading the usage of RAM and then allow for proper operation of the computer, a method for memory usage evaluation is required.
The first operation is the determination of the total amount of memory required in order to store all the domain information. This is possible with the relation:

$$M_{TOT} = N_f \left(j_{P2} - j_{P1}\right) \left(i_{P2} - i_{P1}\right) \tag{4.8}$$

where M_{TOT} is the total memory required expressed in bit, N_f is the number of frames to load and d is the color depth for each pixel (24 bit, 8 bit for each color channel).
Defined a RAM limit (it is preferable define this parameter as 80% of the maximum RAM in order to avoid the slowdown of the PC operations), it is possible to split the domain into a finite number of subdomains found rounding up the result of the relationship:

$$n_{subdomain} = \frac{M_{TOT}}{RAM_{limit}} \tag{4.9}$$

By doing this, it is ensured that the memory consumption for each subdomain is less than the RAM limit. When a subdomain has been analyzed, the information related is erased from the memory in order to allow loading the next subdomain without overloading the available RAM.
Before starting to explain the core of the activation time search methodology, a clarification is needed in order to ease the reading. From now on, the concept of temporal evolution of the color intensity for a pixel will be called signal, furthermore the activation time will be expressed in number of frames. The evaluation of the activation time in seconds it's trivial since the acquisition of the images is carried on at a constant frame rate of 25 Hz.

4.2.2 Background subtraction

It is done in order to simplify any signal normalization and thresholds definition for the subsequent filtering operations. Background is obtained by averaging the information contained in each pixel of the evaluated domain of the first 25 acquired images. Considering in the mean the first second of acquisition it is ensured that liquid crystals are not activated, hence pixels contain only information inherent to the background. The background value is subtracted from the signal of each pixel, as reported in Fig. 4.11 where is shown an exemplification of background subtraction for the red, green and blue channels.

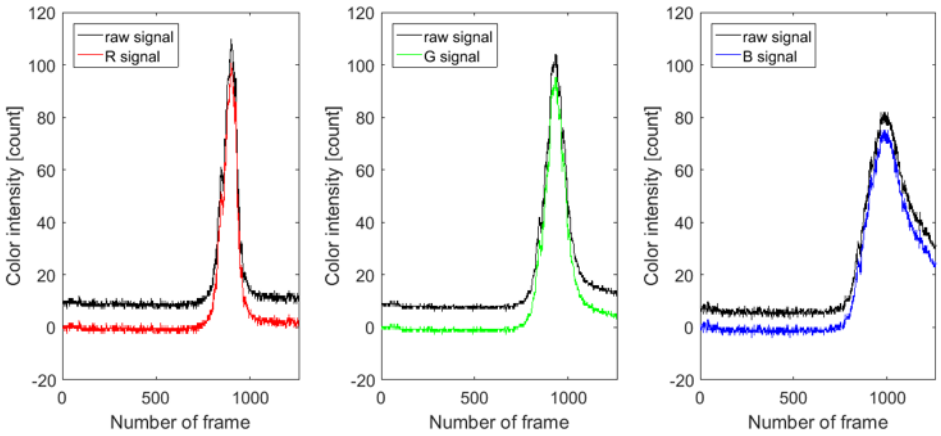

FIGURE 4.11: Background subtraction.

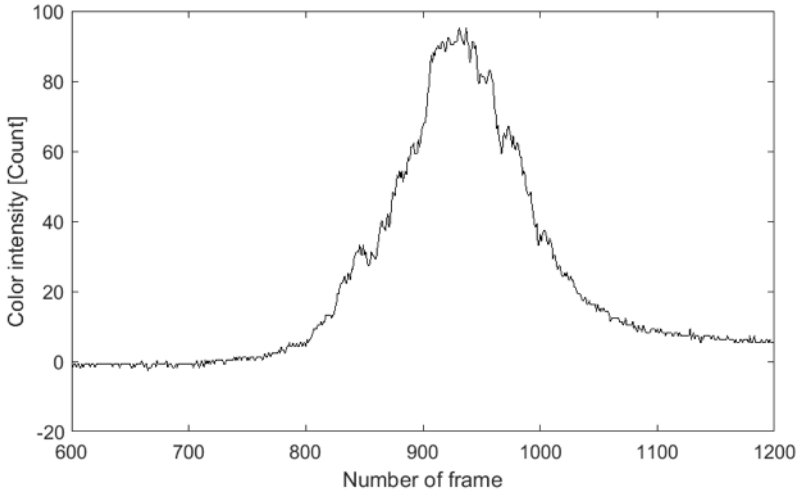

FIGURE 4.12: Highlight of a signal peak.

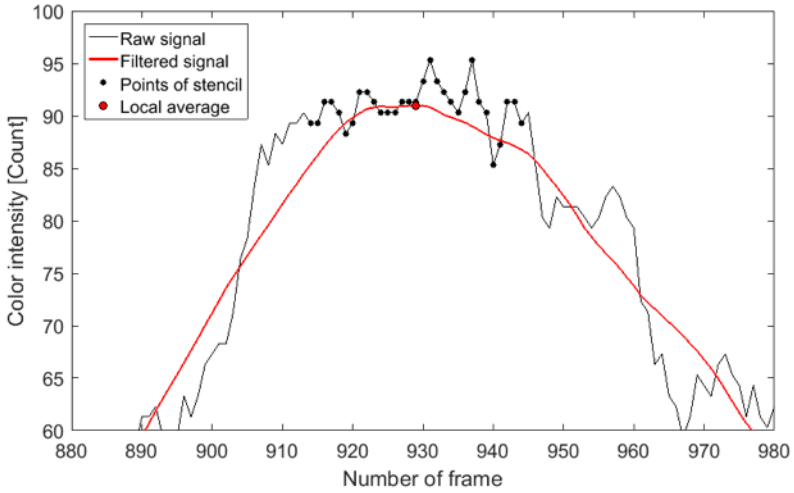

FIGURE 4.13: Example of moving average method.

4.2.3 R, G, B signal filtering techniques

As it can be seen in Fig. 4.11 and more clearly in Fig. 4.12, the color signals are characterized by a not negligible noisy component. This component can adversely affect the detection of the maximum of the signal leading to erroneous results. For this reason, before carrying out the search for the maximum, the signal has to be filtered so as to eliminate as much as possible of the noisy component being careful not to modify the shape of the signal (modification of the shape alter the peak location). Different filtering methods may be used depending on the type of signal and the three methods used in this work will be described.

Moving average
This method has been designed in order to perform a rough filtering of the signals in order to predict the position of the maximum, it is also used to define the maximum of the signal during liquid crystal calibration.
After defining the length of a stencil of points, to each point of the signal is assigned the average value of the points contained within the stencil according to the relation:

$$S_i = \frac{1}{2K+1} \sum_{k=i-K}^{i+K} S_k \tag{4.10}$$

where K is the half length of the stencil. As it can be easily guessed, this method causes data loss equal to half stencil at the beginning and at the end of the signal.
In Fig. 4.13 is shown an exemplification of this filtering method, it is visible how the filtered signal in red well fit the raw signal.

DFT (Discrete Fourier Transform)
Another approach has been developed resorting to the discrete Fourier transform in order to decompose the sampled signal into its frequency contents in order to make easier the determination and the elimination of only the noise component.
As an example, the color intensity signal in Fig. 4.14a is defined in time domain since each value of the signal corresponds to an acquired image.

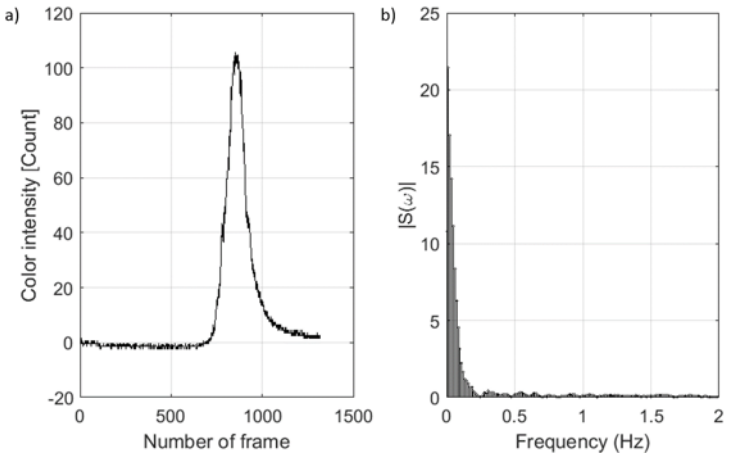

FIGURE 4.14: Example of DFT: raw signal (a), frequency spectrum of raw signal (b).

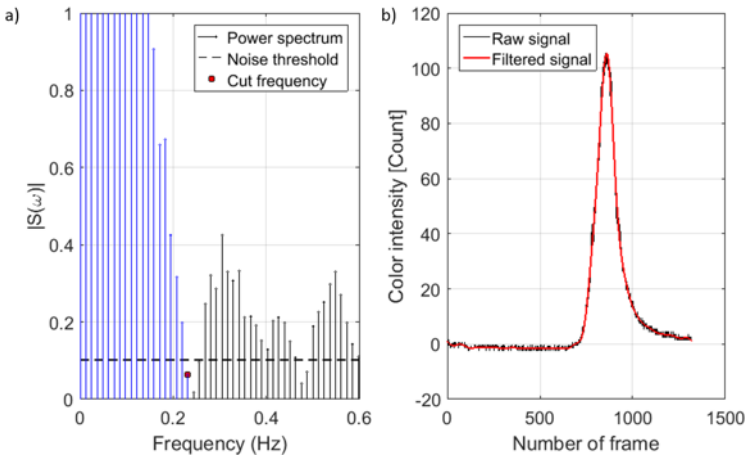

FIGURE 4.15: Example of DFT: cut frequency definition (a), filtered signal (b).

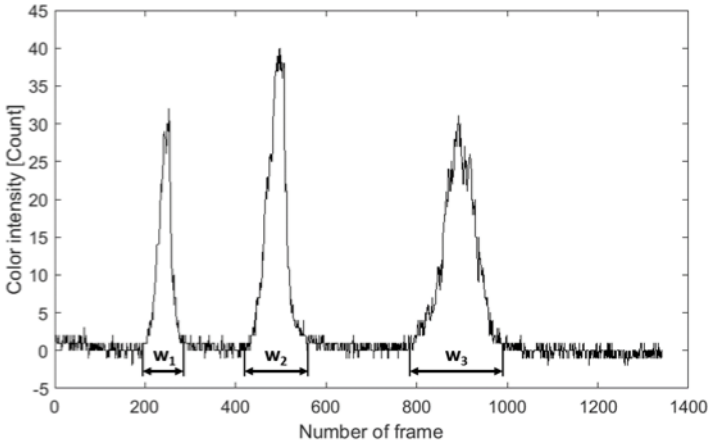

FIGURE 4.16: Example of multipeak signal.

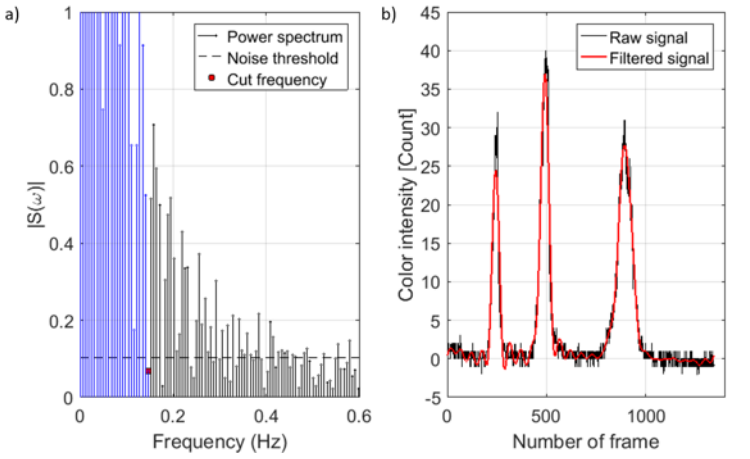

FIGURE 4.17: Example of DFT on multipeak signals: cut frequency definition (a), filtered signal (b).

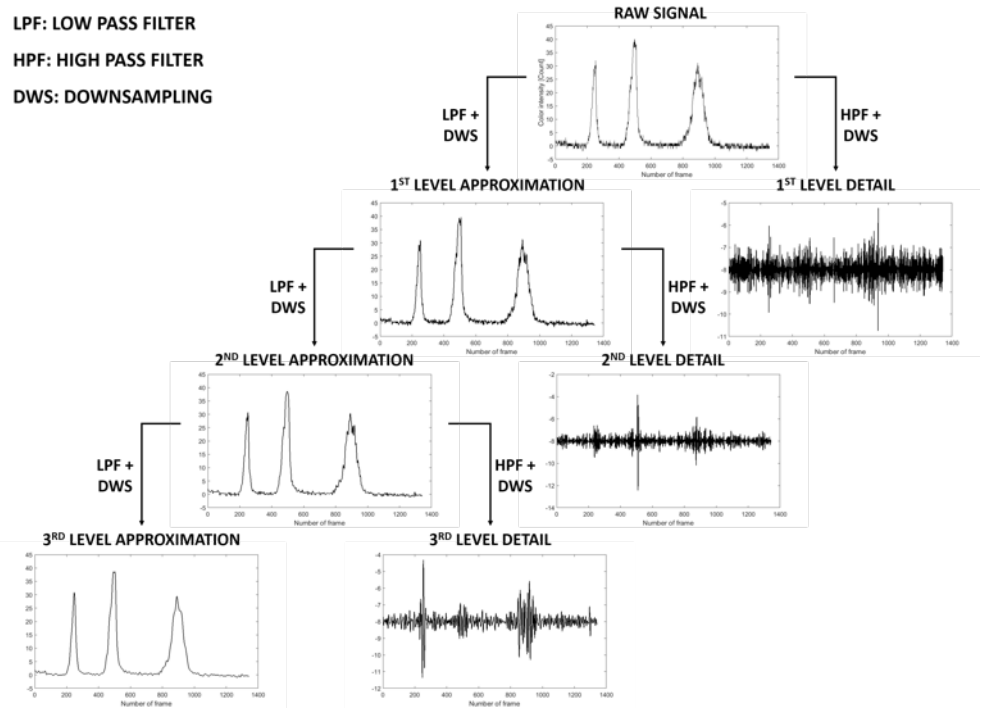

FIGURE 4.18: Example of DWT on multipeak signals using a *bior 3.5* mother wavelet.

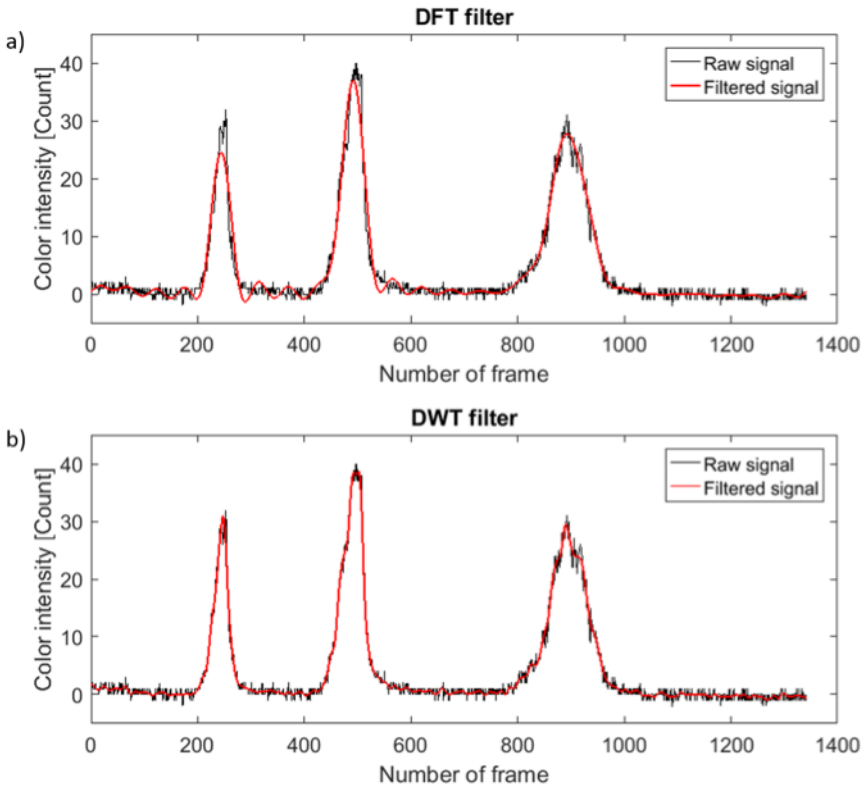

FIGURE 4.19: Comparison of DFT (a) and DWT (b) filters on multi peak signals.

Therefore, on signal $s(t)$ can be applied the discrete Fourier transform, bringing it in the frequency domain $S(\omega)$. In Fig. 4.14b is shown the spectrum of frequencies of the signal. As expected the spectrum is characterized by maximum values of intensity for low frequencies, corresponding to the trend of the signal. Then it can be seen a sudden collapse of the intensity modulus and a frequency interval in which the latter is maintained at low values.
This frequency range corresponds precisely to the signal oscillations that is going to eliminate, in other words the noise content.
The cut frequency, that is the frequency above which the signal content is considered noise, is defined as reported in Fig. 4.15a. A noise threshold is evaluated as the maximum value of the intensity modulus in the range of frequencies within $f_s/4$ and $f_s/2$ (Nyquist frequency). The lower frequency with the intensity modulus less than the noise threshold defined is adopted as cut frequency. At this point, the modulus of the frequencies higher than the cut frequency are set to zero and the signal is reconstructed through the use of the inverse transform obtaining the filtered signal in Fig. 4.15b.
Since discrete Fourier transform is defined only in frequency domain, this filtering method is applicable only on signal with one peak or signal with peaks with the same shape (intensity and width).

DWT (Discrete Wavelet Transform)
In TLCT applications, when multiple liquid crystals with different activation temperatures are used, the signal obtained from the evaluation of the color intensity of a pixel presents multiple peaks with different shapes as reported in Fig. 4.16. As it can be seen, the width of the peaks increases throughout the test duration reflecting on a difficult definition of a unique cut frequency in order to filter the signal. Analyzing the spectrum of the frequencies obtained applying the Fourier transform to the signal it can be noticed that frequency content related to the peaks are not well distinguished with respect to the case of single peak reported in Fig. 4.15. As in precedence, the signal is filtered using the same criterion for the cut frequency definition. The raw signal and the filtered one are reported in Fig. 4.17b. As it can be seen, this definition of the cut frequency does not allow a good signal filtering, introducing fluctuation and change in the peak position.
For this reason, it is considered necessary to use a method that allows the characterization of a signal both in the frequencies field in order to recognize and eliminate the noise component, and in time in order to locate the position of the peaks related to the activation of the liquid crystals.
The discrete wavelet transform is the best suited for the purpose. This filtering method well explained in [1], applies on the signal high pass and low pass filters; the output of the high pass filter is the detail signal, while from the low pass filter is obtained the first level approximation signal. This procedure is repeatable and a representation of this filtering method is reported in Fig. 4.18, where three banks of filters are applied to the raw signal on top. The result of the DWT filter is highlighted in Fig. 4.19b. Comparing the filtered signals in Fig. 4.19b and 4.19a it can be appreciated how DWT works better with multi peak signals allowing to avoid peak shifting that can be source of errors in the heat transfer coefficient computation.

4.2.4 Peak find procedure

In the following the peak find procedure will be explained. Fig. 4.20 depicts all the phases developed in order to correctly identify the maximum of a signal.
The analysis starts from the evaluation of the first derivative of the filtered signal, keeping in mind the elimination of the head and the tail of the signal that may provide false

information due to the filtering. The first derivative computation is performed by means of the central finite differences method, hence the derivative for each time instant can be written as:

$$dS(i) = \frac{s^f_{i+1} - s^f_{i-1}}{2} \tag{4.11}$$

Finding the maximum of the first derivative (Q) ensures that the first zero to the right of this point corresponds to the signal maximum ($B' - B$). Points P' and R' are the zeros of the first derivative upstream and downstream the peak maximum, in fact they define the amplitude of the peak and are used in the multi peak search in order to set the derivative to zero within the range defined by them. By doing this multiple search of the same peak can be avoided.
Thresholds on the first derivative and on the amplitude of the peak avoids the search of false peaks in order to reduce the computational efforts. If for the considered peak both thresholds are respected, on the raw signal is defined a stencil of points (A to C), where points A and C are defined as the 80% of the peak. Points contained in the stencil are interpolated by a third order polynomial as reported in the highlight of Fig. 4.20 and finally the maximum of the peak (T) is found on the interpolated signal.

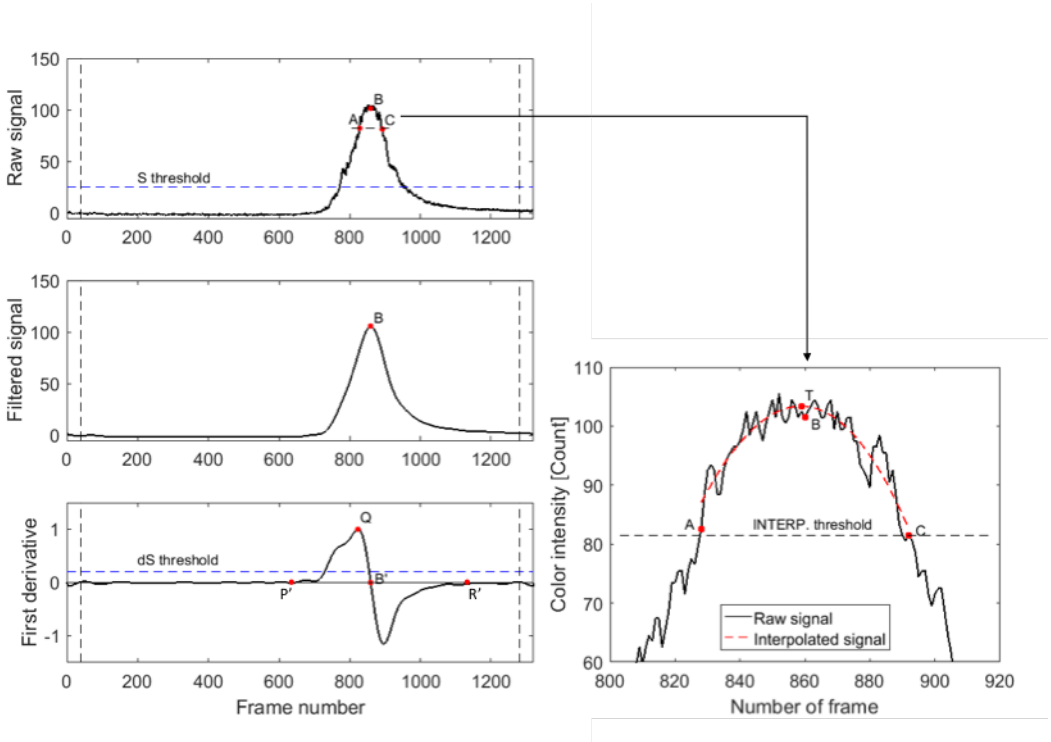

FIGURE 4.20: Example of peak find procedure.

4.2.5 Multi peak association & validation procedure

When a single liquid crystal is used, it is easy to associate the activation time derived from the analysis of the red, green and blue signals to the correspondent liquid crystal. However, when multiple liquid crystals are used this association becomes more difficult since the detection of the activation time doesn't follow a specific order. In Fig. 4.21 a representation of a multi peak signal is shown. It can be seen that the peak find algorithm has found the peaks of the three liquid crystals plus an additional peak on the red signal. The reasons for which these false peaks are found can be: search errors due to incorrect setting of the thresholds or the establishment of local recirculation zones (especially in the vicinity of the ribs) where the crystals are subject to a non-monotonous temperature variation, hence in these areas it can be activated multiple times during the same test.
For this reasons it becomes necessary to adopt a methodology in order to recognize and not consider the false peaks in the calculation of the heat transfer coefficient. The peak association algorithm developed is shown in Fig. 4.22.
Peaks of each color signal are sorted and to each one is associated a flag that indicates if the number of peaks found is equal, higher or lower with respect to the expected number of liquid crystals (in a correctly defined experiment is the number of liquid crystals sprayed on the measurement surface).

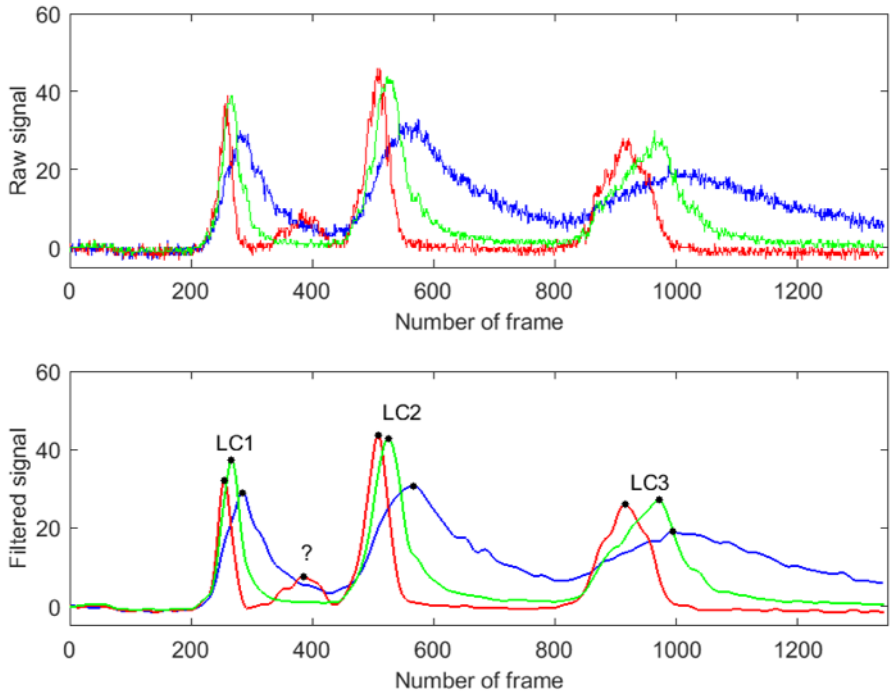

FIGURE 4.21: Multi peak signal with false peak information.

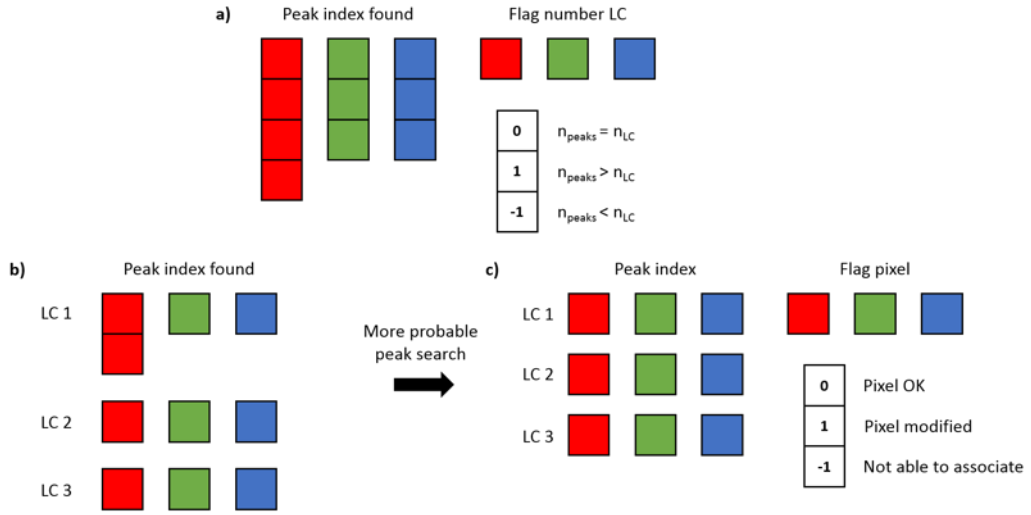

FIGURE 4.22: Peak association algorithm.

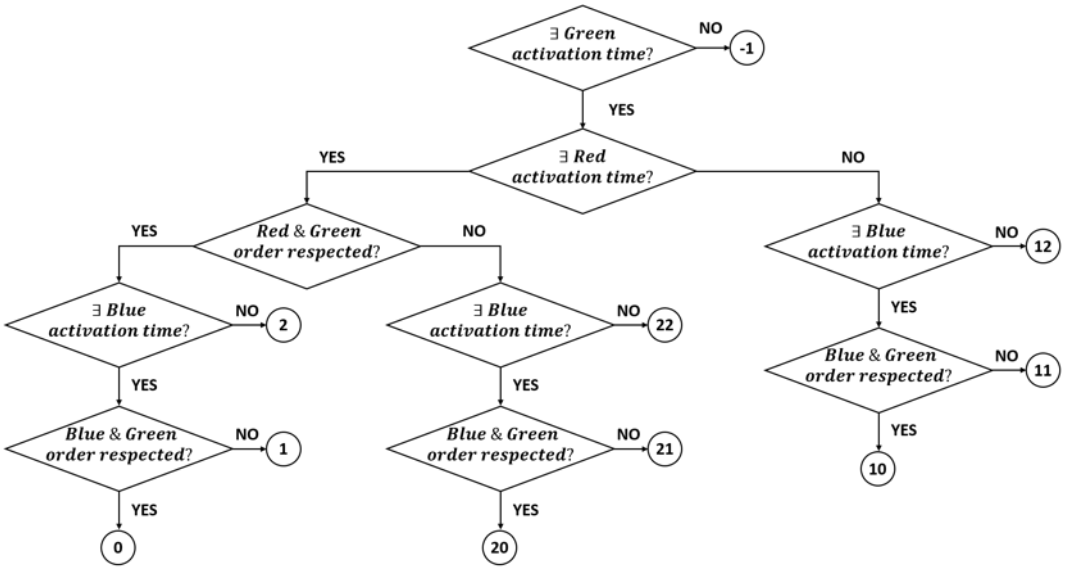

FIGURE 4.23: Liquid crystal validation algorithm.

The algorithm associates between their peaks that have a relative distance less than the distance given by the product $f_s\ t_{thr}$, where t_{thr} is the minimum time between a two consecutive peaks and is set by the user by a previous analysis of the image sequence (Fig. 4.22b). Depending on the type of the experiment (hot or cold) the peaks with lower activation time are associated respectively to the liquid crystal with lower activation temperature and the other crystals are associated consequently.
At this point, for each liquid crystal with a number of peaks found higher than the expected number of liquid crystals, starts the search for the most probable peaks. These peaks are recognized as those who respect the correct order of activation depending on the experiment (hot or cold) and have the highest intensity value.
For each pixel a flag is then associated. For each channel, the flag reports: if the search for the most probable peak occurred, if this function has not been used or if there is not enough information for the pixels to be able to assign unambiguously the peaks correspondent to the crystal (Fig. 4.22c).
The last step is the validation of the pixel. A hierarchical algorithm (Fig. 4.23) has been developed in order to identify and classify pixels not in compliance with a "well done experiment" criteria; as an example, pixels where the R, G, B activation order is not respected or where one color peak is missing. The results of this procedure are n validated activation time matrices (one for each liquid crystal).

4.3 Bulk temperature computation

The widely used reference temperature for defining the local heat transfer coefficient in internal flow is the bulk temperature. In the case of constant specific heat and density can be expressed by the equation:

$$T_b(x) = \frac{1}{\bar{u}A} \int uTdA \tag{4.12}$$

In experimental applications the determination of flow temperature of the whole domain can be very complicated. For that reason, it is common practice to use as reference flow temperature the linearization of the temperatures acquired in correspondence of the inlet and the outlet of the test section.
Following the idea proposed by Poser et al. in [28], a procedure of calculation of the T_{bulk} has been developed and is based on the two-dimensional interpolation of the temperature information obtained by thermocouples immersed in the fluid in known positions along the channel length.
Firstly, temperature readings are filtered. In order to avoid introducing instability or distortion of the filtered signal caused by the rapid change in temperature applied to the air stream in order to trigger the thermal exchange with the walls of the measuring section, the raw signal is divided into two parts:

- Before the application of the temperature step (red point in Fig. 4.24). This point is found by an algorithm that moves a stencil along the vector that contains the temperature values; when all the points contained in the stencil satisfy the relation:

  $$T_i > T_m + 2\sigma \tag{4.13}$$

  where T_m and σ are the mean temperature and the standard deviation respectively evaluated on the first second of acquisition, the algorithm stops the search and the time instant before the time instant correspondent to the first element in the stencil is set as the starting point of the temperature step.
  At this point, to the time interval between the initial time and the start of temperature raise is assigned the mean value of the temperature evaluated on the same interval.

- After the red point a fifth order low-pass *Butterworth* filter is used in order to reduce the noise of the signal.

The geometry of the entire test section is imported from a CAD interface (Fig. 4.25). Boundary coordinates of the geometry and thermocouple positions are used to define a mesh (Fig. 4.26) over which the bulk temperature is evaluated thanks to a FEM solver.
Boundary conditions are imposed on the meshed area in order to allow the computation:

- Imposed temperature ($T = T_i$) in correspondence of the thermocouple positions;
- Neumann conditions ($\partial T/\partial n = 0$) on the inlet and outlet surface and on the channel walls.

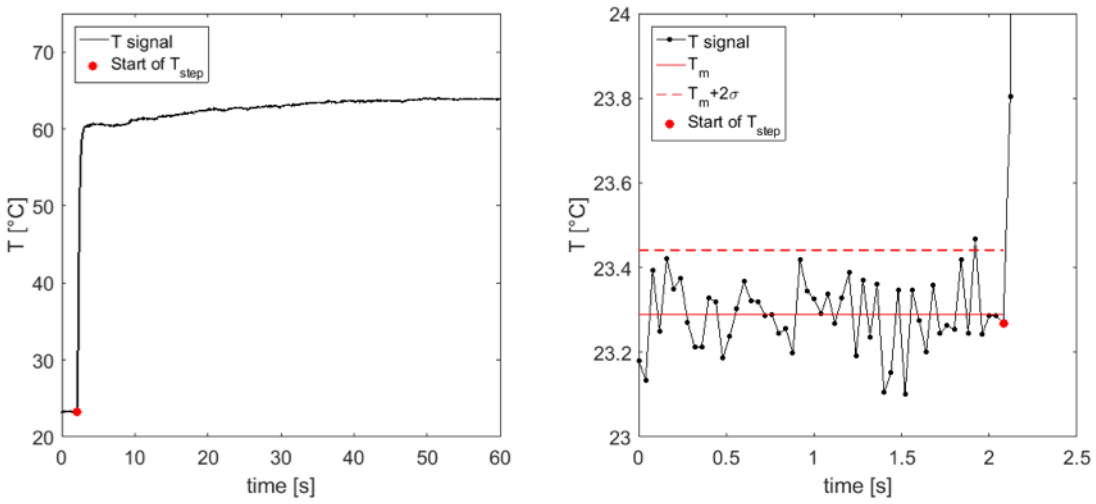

FIGURE 4.24: Temperature step start definition.

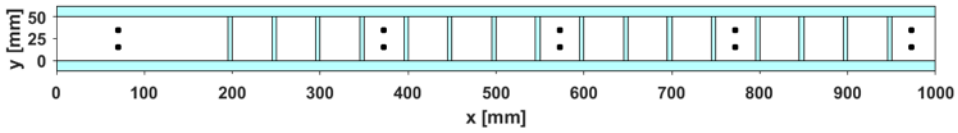

FIGURE 4.25: Example of T_{bulk} domain.

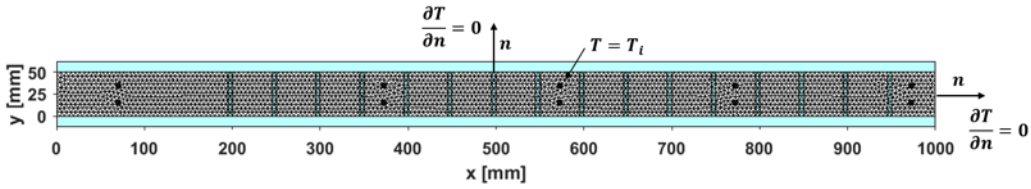

FIGURE 4.26: Example of mesh for T_{bulk} computation and boundary conditions imposition.

In order to obtain the temperature of the flow on the mesh nodes not corresponding to the positions of the thermocouples, an interpolation scheme based on the assumption that at each time step is used. The spatial distribution of the temperature of the fluid is described by the Laplace equation:

$$\frac{\partial^2 T}{\partial x^2} + \frac{\partial^2 T}{\partial y^2} = 0 \tag{4.14}$$

It is known that this equation physically represents the stationary conduction within a solid, but it still represents an excellent two-dimensional interpolation strategy.
The result of the computation is a temperature map evaluated for each time instant. In Fig. 4.27 is shown the temperature distribution obtained with a hot temperature step imposed to the process fluid.

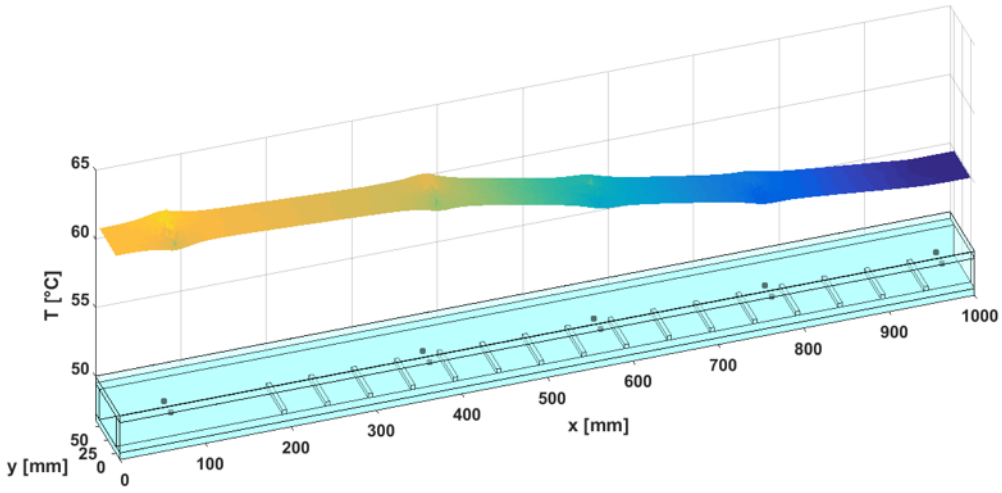

FIGURE 4.27: T_{bulk} at a generic time instant.

4.4 Liquid crystal calibration (RGB)

The liquid crystal calibration is the procedure needed in order to assess the activation temperature of the liquid crystals by associating each maximum of the signal intensity (red, green and blue signals) to the correspondent temperature. It can often happen that information provided by the liquid crystal suppliers are incomplete or inaccurate, hence a calibration procedure has been developed and liquid crystals calibrations are carried out using the calibration apparatus explained in Par. 3.5. In order to obtain reliable data useful for heat transfer computation, information of temperature and images of the calibration surface are acquired simultaneously for different temperature gradients imposed to the calibration plate. The acquisitions are performed always only after the plate has reached a stationary condition of the temperature.
To manage the acquired data and obtain the activation temperature of the liquid crystals an in-house software has been created. The software receives in input:

- the temperature values acquired by the thermocouples placed at known positions below the calibration plate;
- an image of the calibration surface on which the liquid crystals are painted.

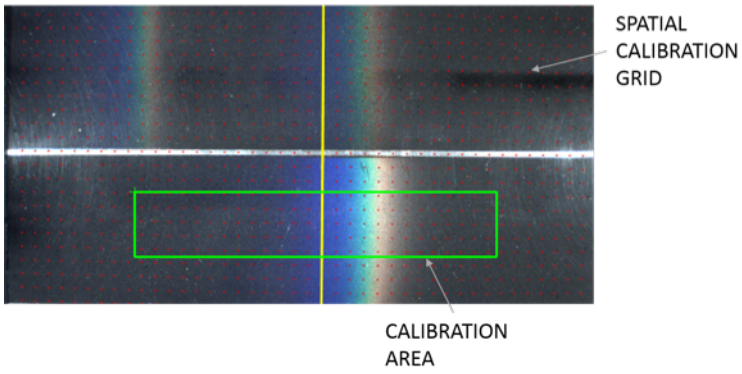

FIGURE 4.28: Calibration area definition.

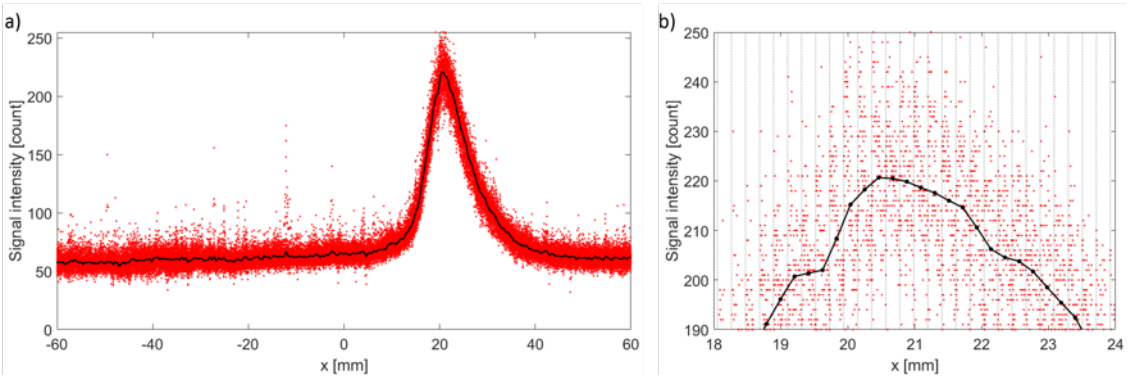

FIGURE 4.29: Color intensity signal.

Temperature readings of each thermocouple are averaged over time. Subsequently, this data is interpolated using the quadratic polynomial equation reported below, in order to obtain temperature values also between the thermocouple positions.

$$T(x) = ax^2 + bx + c \tag{4.15}$$

A calibration window can be selected directly from the acquired image. As shown in Fig. 4.28, the definition of window allows isolation, and then analysis of different areas of the calibration plate. It's clear that the selected window must contain the activated liquid crystals. This selection defines a portion of the image in which the software retrieves all the color intensity information stored in the form of a three-dimensional matrix, in which each layer corresponds to one color: red, green and blue. Using the coefficients of the transformation functions previously evaluated with the image calibration (see Par. 4.1), the color indications of each pixel are associated to the correct position in the physical space. Referring the information of all pixels to the same reference system, a distribution of color intensity can be obtained. In Fig. 4.29a is reported the distribution of the color intensity for the red signal. As it can be seen from the magnified signal represented in Fig. 4.29b, the color levels corresponding to each space coordinate are very dispersed. Hence, in order to perform a correct analysis of the color intensity signals, the color levels relating to each space coordinate can be averaged. It can also be noted how points correspondent to the same spatial coordinate don't have the same value of abscissa, hence the arithmetic average of the color intensity cannot be used. A series of gropus of points having similar abscissa can be distinguished from the figure. For each group, the center of gravity can be evaluated for the cloud of points. The center of gravity represents the average value of the signal in the spatial coordinate. The result of this spatial average is the black line shown in Fig. 4.29a.
For each red, green and blue averaged signals, the maximum value is found. The maximum of signal intensity corresponds to the activation temperature of the liquid crystal. The axial coordinates correspondent to the three maximum are used to evaluate the related activation temperature using the interpolation polynomial (Eq. 4.15) as follows:

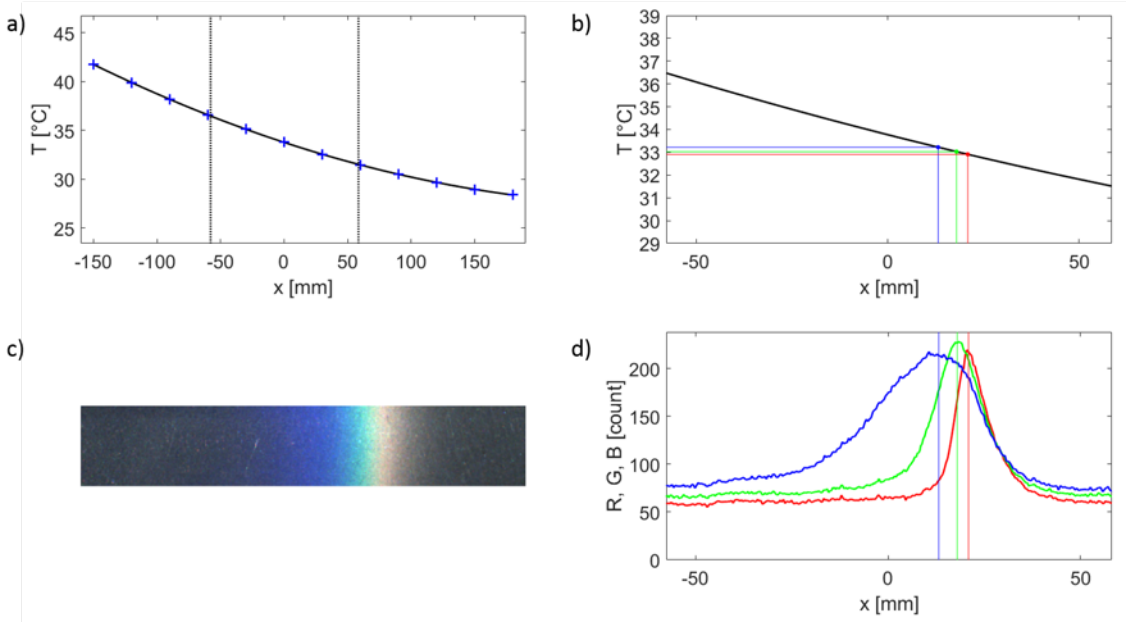

FIGURE 4.30: Liquid crystal calibration.

$$\begin{cases} x_R = \max(I_R) & \rightarrow & T_R = T(x_R) = ax_R^2 + bx_R + c \\ x_G = \max(I_G) & \rightarrow & T_G = T(x_G) = ax_G^2 + bx_G + c \\ x_B = \max(I_B) & \rightarrow & T_B = T(x_B) = ax_R^2 + bx_B + c \end{cases} \tag{4.16}$$

In Fig. 4.30 is recapped all the information used for the liquid crystal calibration: the temperature interpolation (Fig. 4.30a), the average of the signal intensities and the related maximum search for the three color channel (Fig. 4.30d), and the determination of the activation temperature (Fig. 4.30b).

4.5 Heat transfer coefficient computation

In order to compute accurately the heat transfer coefficient for each point of the domains, it must be ensured the coherent combination of the information given by the analysis of the color signals and the evaluated bulk flow temperature values. Since these two information are related to two different domains (camera domain and the whole test section), it is necessary to introduce new reference systems which allow an easy coordinate transformation.
In Fig. 4.31 the reference systems adopted are shown:

- Absolute reference system (X, Y, O): this reference system is used to define the positions of the nodes of the finite elements used for the interpolation of bulk temperature and the points on which the heat transfer coefficient of heat exchange will be calculated;
- Relative reference system (x, y, O'): is the reference system of the physical space, defined during the spatial calibration
- Camera reference system (j, i): is the reference system of the image space. It has as it's origin the vertex at the top left of the camera field of view.

Once the reference systems are defined, it is possible to evaluate the correct position of each point of the domain (in red in Fig. 4.31) using the relation:

$$\begin{cases} X = DX + x(-1)^{rx} \\ Y = DY + y(-1)^{ry} \end{cases} \tag{4.17}$$

where rx and ry can be 0 or 1 depending if the axes of the absolute and relative systems are in accordance or are discordant.
At each point it is then associated to the bulk temperature of the nearest node. Now that all the necessary information is known, it is possible to carry out the calculation of the heat transfer coefficient.

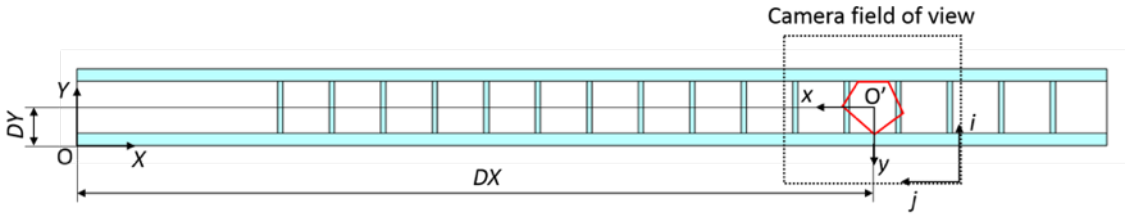

FIGURE 4.31: Reference system.

In order to ease the reading, below is reported the solution of the heat equation approximated with the Duhamel approach for non-ideal temperature steps (Eq. 5.4). It can be seen that the evaluation of h cannot be performed directly, hence a recursive approach has been adopted.
The Newton-Raphson method has been chosen in order to evaluate the heat transfer coefficient. This method, starting from the Eq. 5.4:

$$f(h) = T_s(t) - T_0 - \sum_{i=1}^{n} \left[1 - \exp\left(\frac{h^2(t-\tau_i)}{\rho c k} \right) \operatorname{erfc}\left(h\sqrt{\frac{t-\tau_i}{\rho c k}} \right) \right] (T_{b,i} - T_{b,i-1}) \tag{4.18}$$

evaluates the value of the heat transfer coefficient resolving the iterative relation here reported:

$$h_{n+1} = h_n - \frac{f(h_n)}{f'(h_n)} \tag{4.19}$$

The iterations stop when $|h_{n+1} - h_n| \leq 10^{-4}$ meaning that the value of the function $f(h)$ is closer to zero.

4.6 Nusselt number (*Nu*) and Enhancement Factor (*EF*) evaluation

For each point of the evaluated domain it is possible to compute the non-dimensional Nusselt number in accordance to the well-known relation reported below:

$$Nu = \frac{h\ D_h}{k_{air}} \tag{4.20}$$

Where h is the heat transfer coefficient, D_h is the hydraulic diameter of the test section considered and k_{air} is the thermal conductivity. This parameter is evaluated making use of a correlation that relates the air thermal conductivity to the absolute temperature of the air flow. The absolute temperature considered is the mean local flow temperature evaluated in the range between the instant in which the temperature variation is imposed to the flow and the activation of the liquid crystal. The correlation adopted is the third degree polynomial reported here:

$$k_{air} = 1.52 \cdot 10^{-11}\ T^3 - 4.86 \cdot 10^{-8}\ T^2 + 1.02 \cdot 10^{-4}\ T - 3.93 \cdot 10^{-4} \tag{4.21}$$

In Fig. 4.32 is reported the evolution of the air conductivity with respect to the increase of the flow temperature. The visible strong temperature dependence means that it becomes really important to associate to each point of the measurement area to the corresponding value of air conductivity.

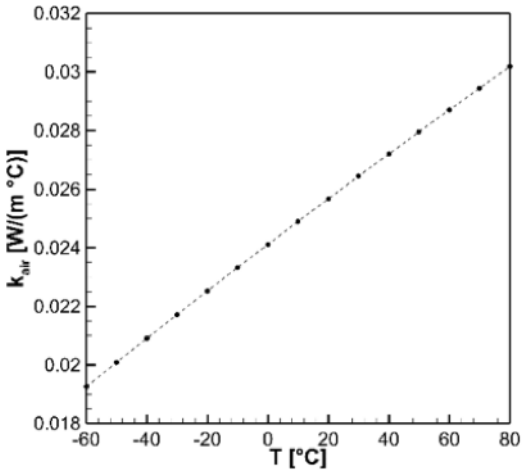

FIGURE 4.32: Air thermal conductivity.

In order to highlight the effect of the turbulent promoters it can be useful to normalize the evaluated Nusselt values with respect to a reference Nusselt. A common and widely used reference value is the one related to a fully developed turbulent flow in a circular pipe with smooth walls, evaluated with the correlation of Dittus-Boelter. The enhancement factor of the turbulent promoters can be then computed as the ratio:

$$EF = \frac{Nu}{Nu_0} = \frac{h\ D_h/k_{air}}{0.023\ Re^{0.8}\ Pr^n} \tag{4.22}$$

where Pr is the Prandtl number, and n can be equal to 0.4 if the wall temperature is higher than the flow temperature ($T_w > T_b$), otherwise 0.3 if the higher temperature is the flow temperature ($T_w < T_b$).

Chapter 5

Experimental applications: one-side ribbed square channel

5.1 Channel geometry

The test section has a length of 1000 mm and a square cross section with $H \times W = 50 \times 50$ m. The hydraulic diameter is than 50 mm, evaluated with the relation reported in Eq. 3.5. In the first 200 mm, the channel walls are smooth while on the remaining part 16 squared ribs are installed on one side of the passage and are arranged normal to the flow direction ($\alpha = 90°$). The ribs height is equal to 5 mm resulting in a pitch-to-height ratio $P/e = 10$ and in a blockage ratio $e/D_h = 0.1$.
As mentioned in Par. 2.1.2 the model used to compute the heat transfer coefficient is based on the Fourier equation under the semi-infinite body hypothesis. In order to replicate this hypothesis in the experimental setup, the test model is completely machined out of Plexiglas that ensures a good optical accessibility, with a minimum wall thickness of 20 mm. The low thermal diffusivity of the Plexiglas and the thickness adopted ensures that the thermal wave generated by the imposition of a sudden variation of the flow temperature does not penetrate inside the whole thickness of the wall before the end of the experiment.

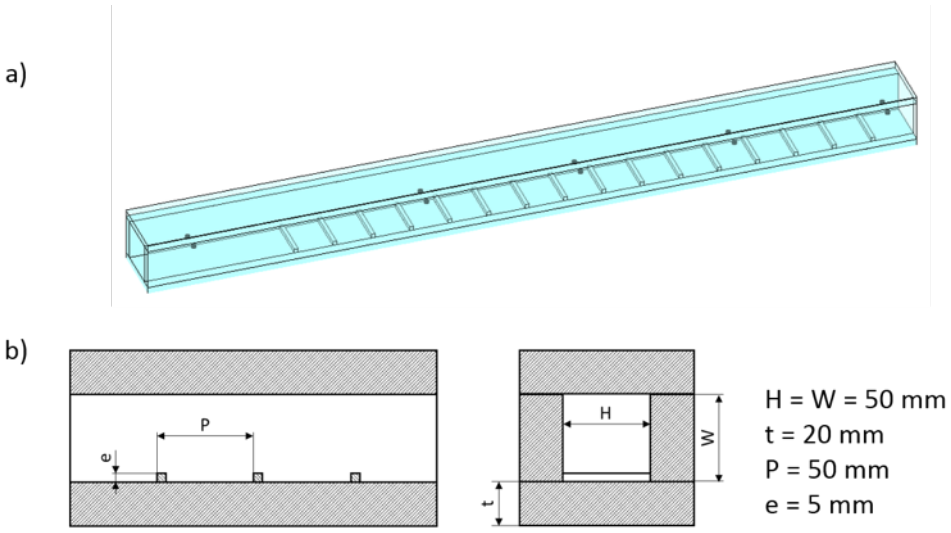

FIGURE 5.1: Test section sketch (a), test section main dimensions (b).

Shultz and Jones in [31] states that the time needed in order to have an increment of $0.01(T_w - T_0)$ of the temperature of the outer surface is:

$$\tau = 0.1\, t^2\, \frac{\lambda}{\rho\, c} \tag{5.1}$$

where t is the wall thickness, λ is the Plexiglas thermal conductivity (assumed as 0.19 $W/m\ K$), ρ is the Plexiglas density (1190 kg/m^3) and c is the heat capacity (1460 $J/kg\ K$). The relation reported in Eq. 5.1 allows duration of the transient tests of about 300 s in accordance with the semi-infinite body assumption.
This geometry has been selected because it can be considered as a good test case against which to validate the proposed experimental rig and methodology, since its aero-thermal behavior is well documented in literature, at least for the stationary channel (Casarsa and Arts [6]). For the rotating channel case, data on a nearly similar geometry is also available thanks to Coletti et al. [10] and Mayo et al. [24], [25].
Ten K-type thermocouples are installed along the channel centerline, entering the channel from both of the side lateral walls (with respect to the ribbed surface) in the positions highlighted by the black dots in Fig. 5.1a.
In Figure 5.2 is reported a schematic representation of the thermocouple installation. A plastic tube is inserted inside a 3 mm hole drilled in the Plexiglas wall in correspondence of the mid height of the wall. Due to the small diameter of the thermocouples adopted (0.075 mm), a thinner plastic tube is then inserted inside the first tube and immersed inside the flow. The immersed length is about one third of the channel width and is necessary to minimize the length of the thermocouple wire exposed to the fluid and in order to give rigidity to the thermocouple probe.
In order to reduce the flow field distortion that can be introduced by a simple 90-degree connection between the air conditioning system and the channel inlet, an ad hoc test section inlet (Fig. 5.3) has been designed. It is composed by an outer chamber constructed in wood and an inner chamber made of insulating material (Depron) separated by an air gap. This insulation allows to minimize the damping effect on the flow temperatures. Conditioned air enters from the top of the inlet chamber and is routed in a direction opposite to the channel entry in order to ensure the best uniform conditions in correspondence of the test section inlet. Due to the imposition of cold temperature evolution to the flow (in the range of +20 °C/-80 °C) the installation of flow straightener before the test section inlet it is not recommended. In the case of a high humidity content in the cooled air flow, the flow straightener channels can be occluded by the formation of frost causing a non-uniform inlet flow field.
In order to monitor the temperature distribution at the channel inlet, hence the flow field uniformity, a mesh of five thermocouples is placed at the entry cross section of the channel. During the execution of the test, temperature differences below 1 °C were observed among the five readings, confirming no distortion of the temperature field that could be a main issue in terms of data accuracy.
The suitability of the designed channel inlet it has been verified performing a test in static conditions for Reynolds equal to 10000 at the test section inlet. Normalized Nusselt data reported in Fig. 5.4 has been evaluated on a wide area of the test section from $X/D_h = 8$ to X/D_h equal to 17, corresponding to the range within 400 mm and 850 mm of the channel length. An augmentation of the enhancement factor until $X/D_h = 12$ and then a stabilization of the Nu/Nu_0 around 2 it can be seen. This trend is attributable to the growth of the fully developed flow condition reached at about $X/D_h = 13$.

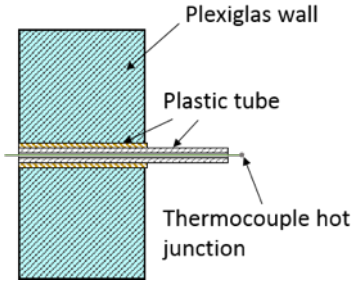

FIGURE 5.2: Thermocouple installation.

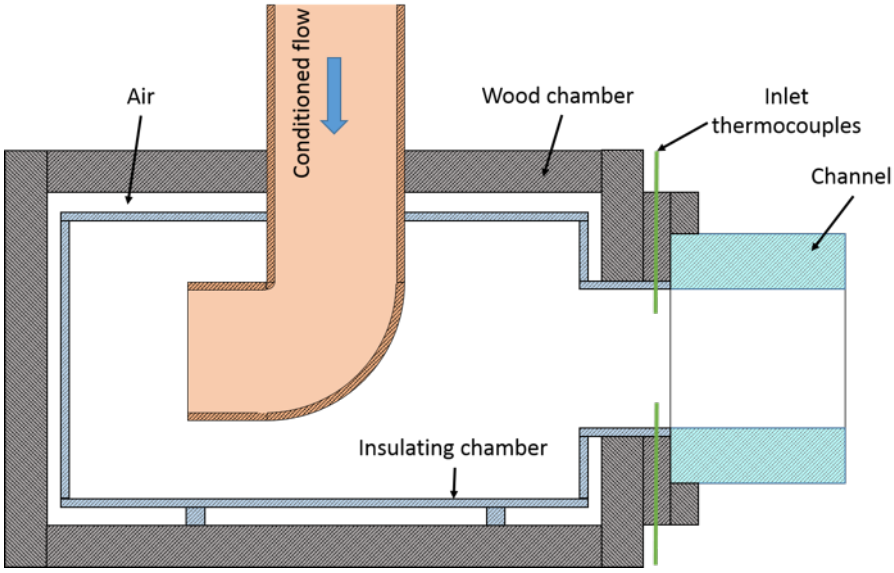

FIGURE 5.3: Sketch of the channel inlet.

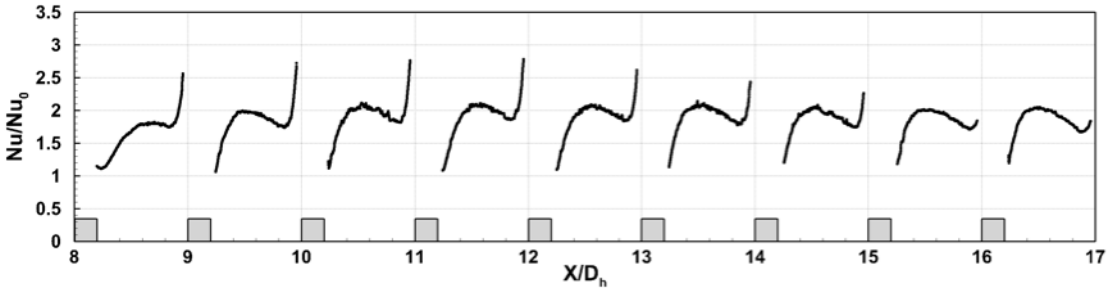

FIGURE 5.4: Normalized Nusselt evolution along the channel lenght, $Re = 10000$ – $Ro = 0$.

5.2 Experimental conditions and data reduction

The measurement campaign had the goal to provide data useful for the rig and methodology validation. With this in mind, a wide test matrix was defined (see Tab. 5.1) where the variation of multiple experimental choices and parameters is considered. A first series of tests (Tab. 5.1a) were performed under static conditions, at $Re = 30000$ and by warming up the fluid (hot step). Heat transfer data was acquired from tests characterized by different activation times of the liquid crystals (achieved with different temperature step evolutions imposed to the process fluid) and by different liquid crystals setup (single or mix of 3 liquid crystals with equal proportion in volume).

TABLE 5.1: Test matrices: static tests - hot step (a), static/rotating tests cold/hot step comparison (b)

(a) Re=30000 - Ro = 0

	Θ
Hallcrest R36C1W	0.47
	0.35
	0.53
	0.63
	0.45
Hallcrest R32C1W	0.44
	0.32
	0.55
	0.44
MIX R32+R36+R40	0.33
	0.43
	0.52

(b) Re = 10000

	Ro	Bo_{ABS}
Hallcrest R36C1W	0	0
	0.1	0.016
	0.2	0.063
	0.3	0.141
	0.4	0.251
Hallcrest R12C1W	0	0
	0.1	0.019
	0.2	0.077
	0.3	0.172
	0.4	0.306

Successively, the Reynolds number was reduced to 10000, in order to be able to explore sufficiently high Rotation values ($Ro = 0 - 0.4$) so highlighting the buoyancy effects that are varying between cold or hot step. All the tested conditions are reported in Tab. 5.1b. Indeed, with the appropriate selection of a single liquid crystal, the same test was repeated imposing a cold or hot step. The static case condition was also repeated in order to verify for data consistency with the rig operated in cold or hot step modality.
Reynolds and rotation numbers are defined with the well-known equations in correspondence of the test section inlet. Buoyancy parameter is evaluated for each point of the measurement surface with the correspondent radius R (with respect to the rotation axis). The evaluation of the buoyancy parameter can be performed only at the activation time instant of the liquid crystal, because only at this instant both wall and bulk flow temperature are known. In Tab. 5.1b are reported the absolute values of the buoyancy parameter relative to the test performed. It should be noted that although the absolute value of the Bo parameter is about the same for similar tests with hot or cold step, they actually pertain to opposite buoyancy effects, not realistic for the hot step case (hotter fluid with respect to the wall).
Heat transfer data will be presented in terms of Nusselt number Nu (Eq. 4.20) or enhancement factor EF (Eq. 4.22).
In accordance to the considerations made in the previous paragraph, heat transfer data were acquired in correspondence of the inter-rib area between the 11^{th} and the 12^{th} ribs (between $X/D_h = 14 - 15$ from the test section inlet), where the flow and the thermal

fields can be considered fully developed.
Narrow banded liquid crystals have been used, since a short activation temperature range is recommended in transient application of the liquid crystals thermography.
The activation temperatures of the crystals were defined simulating the wall temperature at the desired time instant due to the imposition of a step temperature variation to the process fluid (air).
Defining a flow condition (e.g. $Re = 30000$) it is possible to evaluate the Nusselt value for a tube with smooth walls for an imposition of a hot temperature step to the fluid:

$$Nu_0 = 0.023\ Re^{0.8}\ Pr^{0.3} \tag{5.2}$$

supposing an enhancement factor $EF = 3$ due to the presence of the turbulence promoters installed on the measurement surface, a local heat transfer coefficient can be evaluated knowing the geometrical properties of the test section:

$$h = \frac{EF\ Nu_0\ k_{air}}{D_h} = 123\ \frac{W}{m^2\ K} \tag{5.3}$$

setting the final temperature of the air, hence the temperature step, and the desirable activation time of the liquid crystal it is possible to evaluate the wall temperature using the relation given in Ireland and Jones [17] for a step change of the fluid temperature. In this example with the supposed flow temperature T_b is 50 °C and the desired activation time t is 15 s:

$$T_s = T_0 + \sum_{i=1}^{n} \left[1 - \exp\left(\frac{h^2(t-\tau_i)}{\rho c k} \right) \operatorname{erfc}\left(h\sqrt{\frac{t-\tau_i}{\rho c k}} \right) \right] (T_b - T_0) = 36\ ^\circ\mathrm{C} \tag{5.4}$$

hence, in this case, a liquid crystal with an activation temperature of 36 °C should be used in these conditions. In according to the relation given in Yan and Owen [41]:

$$\Theta = \frac{T_w - T_0}{T_b - T_0} = 0.53 \tag{5.5}$$

the evaluated activation temperature is verified in order to ensure that the non-dimensional temperature parameter falls within the range $0.3 < \Theta < 0.7$. By ensuring this condition, the data uncertainty on the heat transfer coefficient h can be minimized.
For this reason, in order to allow the imposition of multiple flow temperature evolutions, the liquid crystals adopted are: Hallcrest R32C1W (LC1), R36C1W (LC2) and R40C1W (LC3) for the hot step tests, and Hallcrest R12C1W for the cold step ones.
In order to ease the reading in the next paragraph are also included the calibration results of the Hallcrest R2C1W. This liquid crystal has been used in the other application of the presented measurement technique.

5.3 Results

5.3.1 Liquid crystal calibration

The different liquid crystals have been calibrated thanks to the calibration apparatus explained in 3.5 and following the procedure reported in 4.4. Multiple acquisitions were performed for each crystal and the adopted value for the heat transfer coefficient computation is the average of the temperature values obtained for each configuration.
In Fig. 5.5 and Fig. 5.6 are reported the results of the calibration performed on liquid crystals used in a single and in a mixture configuration. In order to perform these calibrations, the aluminum plate is painted, symmetrically to the middle line, on one side with the single liquid crystal and on the other side with the mixture of the three liquid crystals. Images of the measuring surface and corresponding temperatures of the aluminum plate have been acquired at different moments in order to verify the repeatability of the calibration of the crystals over time. The summary of all tests carried out is shown in Tab. 5.2, where the average values of the temperatures of the various crystals calculated for each channel (R, G, B) and the corresponding dispersion is reported.
The dispersion of results is given by a set of causes, such as the accuracy of the determination of the maximum of the color intensity signals by the developed algorithm. The uncertainty with which the maximum is determined, propagates on the estimation of the activation temperature. From Eq. 4.15 results that:

$$\left(\frac{dT}{dx}\right)_{x=x_0} = 2ax_0 + b \quad \rightarrow \quad \Delta T = (2ax_0 + b)\Delta x \tag{5.6}$$

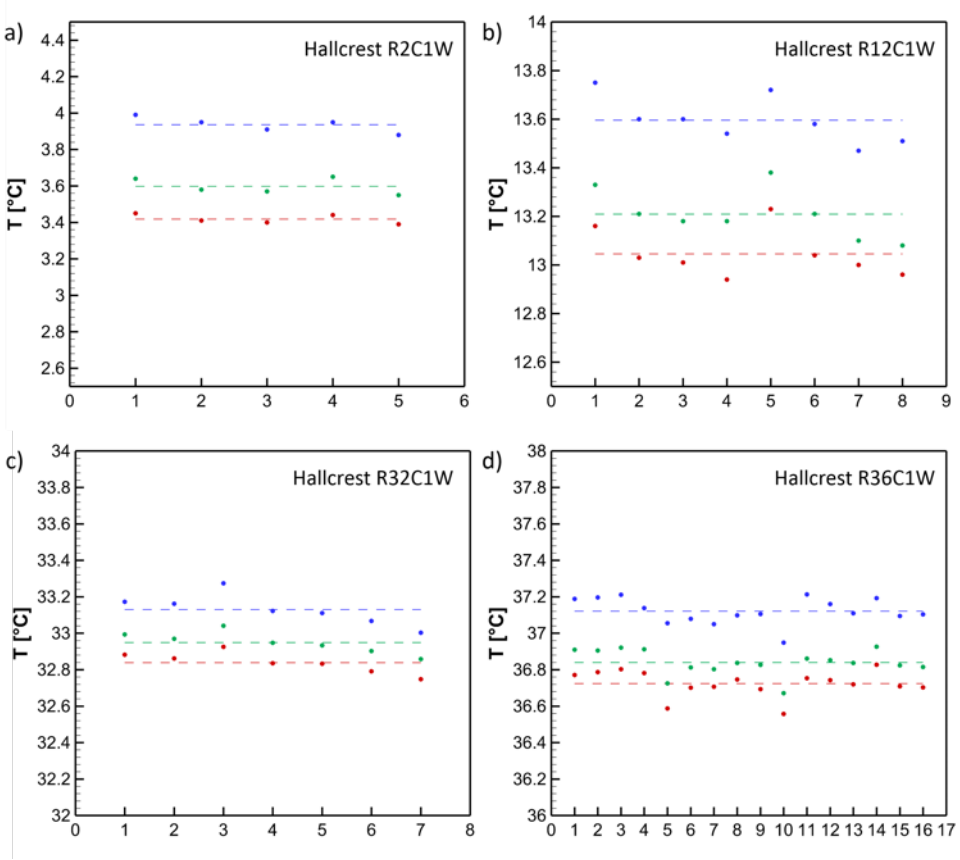

FIGURE 5.5: Calibration of liquid crystals in single configuration: R2C1W (a), R12C1W (b), R32C1W (c), R36C1W (d).

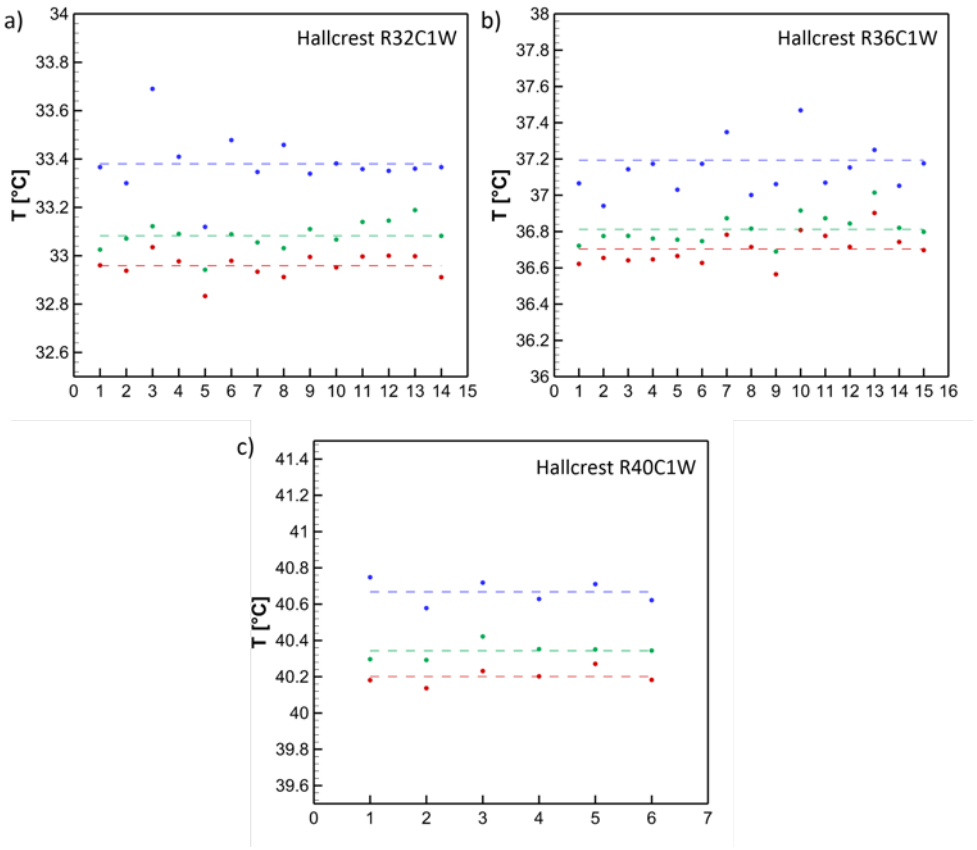

FIGURE 5.6: Calibration of liquid crystals in mixture configuration: R32C1W (a), R36C1W (b), R40C1W (c).

it is clearly highlighted the dependency of the temperature uncertainty to the location of the maximum (x_0). For these reasons, in order to reduce the uncertainty of the results, liquid crystal calibrations were carried out in areas of the aluminum plate subject to a low temperature gradient.

TABLE 5.2: Summary of liquid crystal calibration

	R	**G**	**B**
Mono - R2	3.42±0.03	3.60±0.04	3.94±0.04
Mono - R12	13.05±0.1	13.21±0.1	13.60±0.1
Mono - R32	32.84±0.06	32.95±0.06	33.13±0.09
Mono - R36	36.72±0.07	36.84±0.07	37.12±0.07
Mix - R32	32.96±0.05	33.08±0.06	33.38±0.12
Mix - R36	36.70±0.09	36.81±0.08	37.19±0.27
Mix - R40	40.20±0.05	40.34±0.05	40.67±0.07

5.3.2 Stationary results: validation tests

In Fig. 5.7 is reported the normalized Nusselt map (Fig. 5.7b) obtained from the analysis of the data acquired during test performed in static condition at a Reynolds number equal to 30000 and a hot temperature step imposed to the process airflow. A comparison between an enhancement map obtained by Çacan [5] on the same geometry, at the same test conditions and with the steady liquid crystal thermography is reported in Fig. 5.7a. This comparison highlights the similarity of the heat transfer features caused by the presence of the ribs, with the peak of heat transfer in correspondence of the impingement zone.

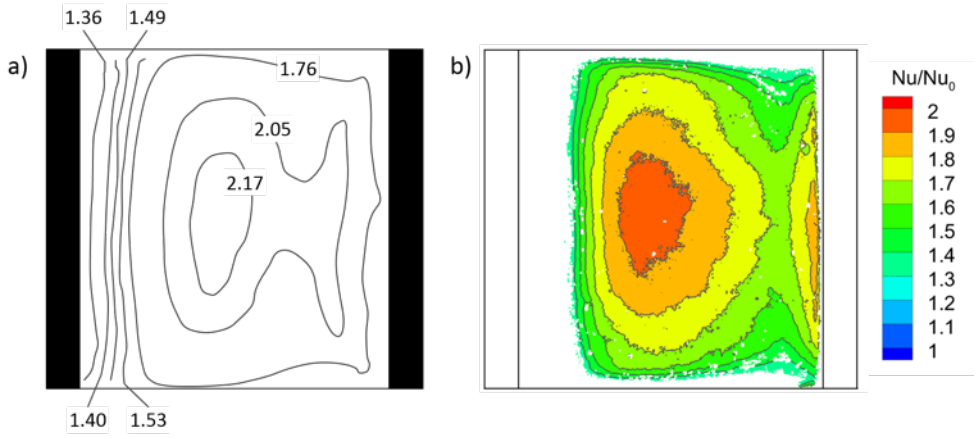

FIGURE 5.7: Normalized Nusselt map comparison, $Re = 30000$ - $Ro = 0$: from [5] (a), present work (b).

Figure 5.8 reports the results obtained with LC2 for tests with different flow temperature steps characterized by different non dimensional temperature parameter Θ as summarized in Tab. 5.1a and in the legend of the figures. The temperature evolution imposed to the process airflow in order to activate this first liquid crystal are shown in Fig. 5.8a.
In order to ease the comparison, Nusselt profiles are extracted in corresponding to the channel centerline and reported in Fig. 5.8b. Again, the typical features of the heat transfer field inside a rib roughened channel flow already presented by Casarsa and Arts [6] are detected namely: a region of high heat transfer located just downstream of the flow reattachment (X/e about 4), the consequent decrease of Nu because of new boundary layer development, and the further peak of Nu upstream of the following rib due to the new flow separation. However, the scope of the present work is to validate the rig and methodology, which is actually confirmed by the satisfactory comparison between the Nu profiles in Fig. 5.8b. Indeed, Nu values from different tests are within $\pm 5\%$ of Nu_{AVG}, which is the ensemble average of all data. This data also highlights the effect of the Θ parameter choice on the data accuracy. As reported in Yan and Owen [41], when Θ approaches the limits of its possible range of variation, the data uncertainty can rise up very quickly. Indeed, data from tests characterized by $\Theta = 0.35$ and $\Theta = 0.63$ differ about 2-3% from the others, which conversely are characterized by a Θ value in the middle of the suggested range and provide almost identical results.
The same considerations can be made by looking at the Nu profiles obtained from tests carried out with the use of a different and colder liquid crystal (LC1) and reported in Fig. 5.9. Also in this case all the profiles fall in the $\pm 5\%$ range with respect to their averaged value, while the effect of Θ is less evident.

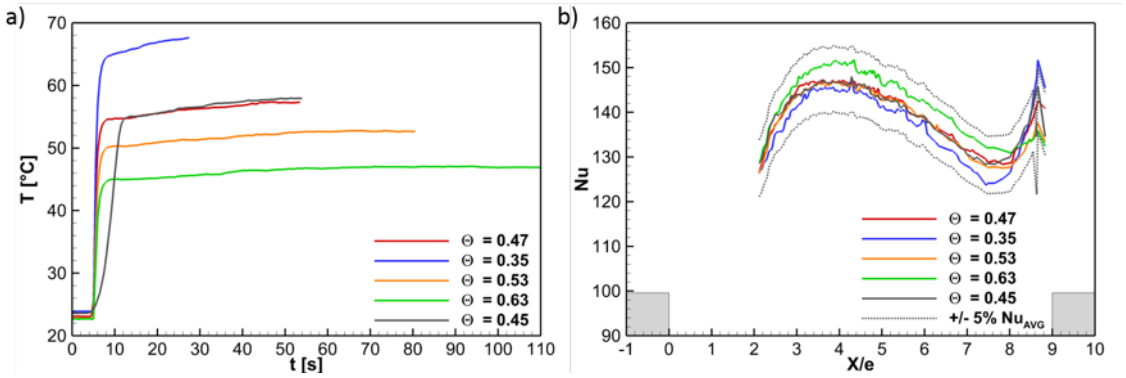

FIGURE 5.8: Temperature step dependency analysis for LC2 ($Ro = 0$): Temperature steps (a), Nusselt profiles .

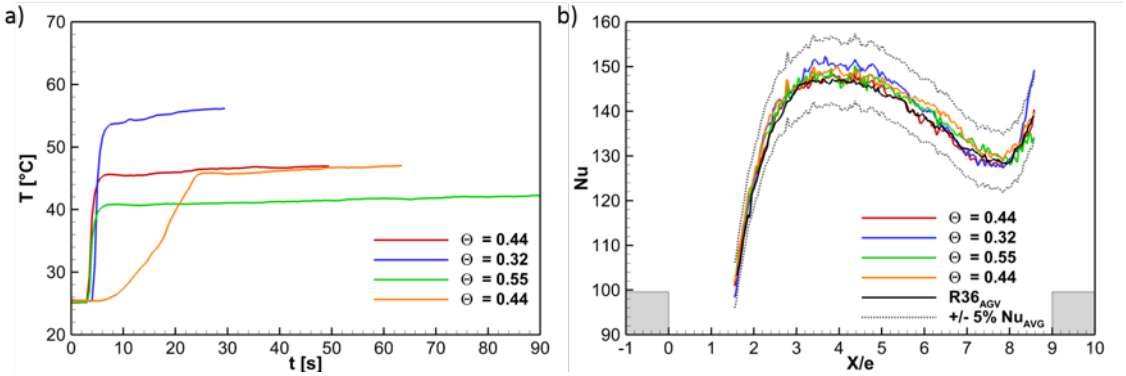

FIGURE 5.9: Temperature step dependency analysis for LC1 ($Ro = 0$): Temperature steps (a), Nusselt profiles.

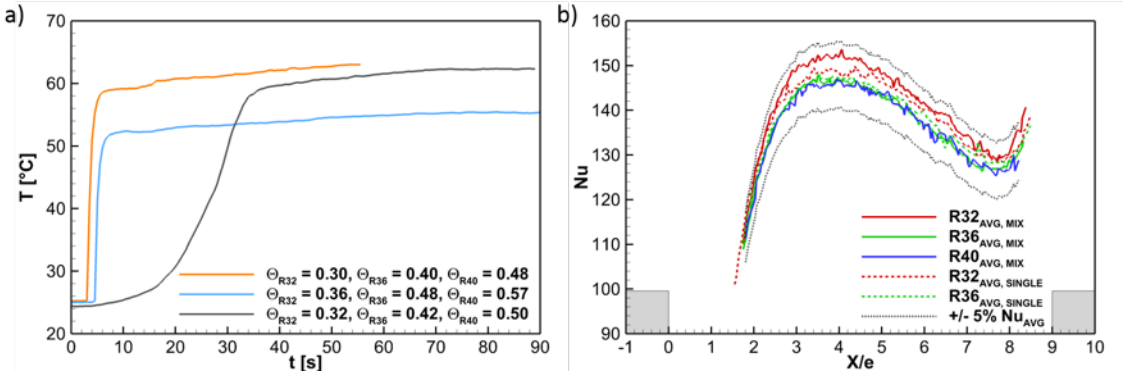

FIGURE 5.10: Liquid crystal mixture comparison ($Ro = 0$): Temperature steps (a), Nusselt profiles (b).

The comparison with the data obtained with LC2, which averaged value is also reported in Fig. 5.9b, confirms once again the robustness of the developed methodology.
Figure 5.10 reports the results obtained with the three liquid crystals used in a mixture configuration. Data comparison, not reported in the graphs in order to ease the reading, shows that also in these cases the variation of the step profile has a minor impact on the final values. For this reason, only the averaged data from the different tests is reported in Fig. 5.10. The indications provided by the three liquid crystals used in a mixture configuration are in good accordance to each other. A maximum difference of about 4% can be found in the region of high heat transfer/flow reattachment downstream the rib. The comparison between the indication of LC1 and LC2 used as single liquid crystals or in mix are also very well in agreement. This confirms that the developed image processing tools are well suited to handle the unavoidable loss of signal intensity that occurs with mix of multiple liquid crystals. As a final remark, it can be noticed that the indications with the lowest Θ parameter ($LC1_{AVG}$ data in Fig. 5.10a) are the only data that provides higher Nu values which are not in perfect agreement with all the other indications.
The results above commented can be also used to provide an estimation about the data uncertainty. Indeed, the test matrix in Tab. 5.1a covers a wide range of variation of multiple experimental parameters. Indeed, by applying it to the same experiment it allows to highlight the measurement errors that can be generated by uncertainties on the measurement of T_b, T_w and on the identification of the activation time. With this in mind, and in view of the results of above, the overall uncertainty can be estimated below 10%.
As a final verification, a comparison with the available literature is made in Fig. 5.11. Confirming the difficulty of performing these types of measurement, here is reported a comparison between data (in terms of Nu/Nu_0 values, span-wise averaged on the inter rib surface) obtained on the presented geometry and data obtained by a literature survey. The selected references are geometries not identical to the present one but with minor differences that do not affect the comparison (0.9 aspect ratio for Mayo et al. [24]). Test conditions are the same for all the compared geometries and the measurement technique adopted for the heat transfer evaluation is the transient LCT for the presented data and the steady LCT for the data found in literature.
This comparison highlights a visible difference between the results obtained with the transient LCT and data obtained by Çacan [5] and Mayo et al. in [25]. Conversely the presented data is in agreement with the data obtained by Mayo et al. in [24].

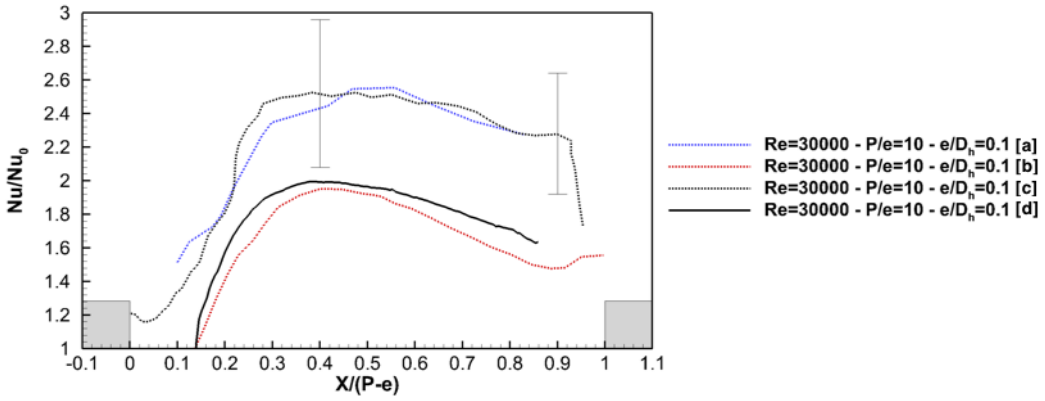

FIGURE 5.11: Literature comparison for $Ro = 0$. [5] (a), [24] (b), [25] (c), Presented data (d)

5.3.3 Rotating results

Before going into the details of the rotating data, a first comparison between data obtained with cold and hot air flow temperature steps is made in static conditions in order to assess methodology reliability. The comparison is provided in Fig. 5.12b (Nu values along the channel centerline), which shows that there is no effect on the aerothermal behavior by changing the test modality. The thermal behavior presented is confirmed by the flow field of Fig. 5.12c, obtained by Coletti et al. [10] on the same geometry in similar flow conditions making use of the Particle Image Velocimetry (PIV). The flow field data of Fig. 5.12c presents a peak of heat transfer in correspondence of the impingement at pitch to rib height ratio of about 4. In the region within $X/e = 4 - 8$ a reduction of the heat transfer it is observed in agreement with the development of the shear layer. In proximity of the rib, at $X/e = 8 - 9$, an increase of the heat transfer is highlighted, and is due to the impingement of the small recirculation bubble visible in Fig. 5.12c.

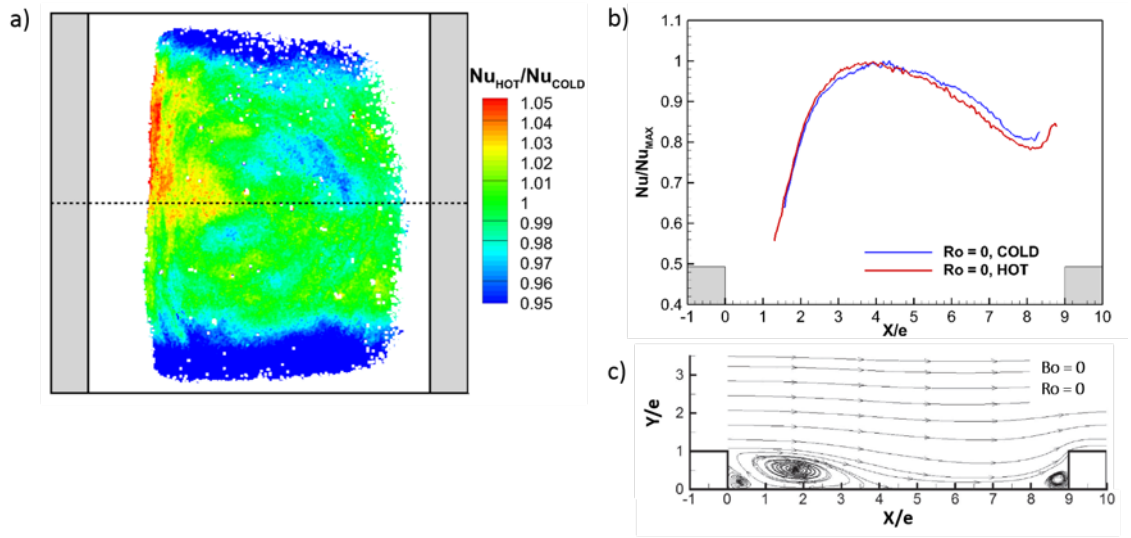

FIGURE 5.12: Comparison for $Ro = 0$: Nu_{HOT}/Nu_{COLD} map (a), midline profile of Nu (b), flow field (c).

A global comparison of the coherence of the results obtained in static conditions with the imposition of a hot and a cold temperature evolution to the process flow is given in Fig. 5.12a. Differences below 5% are observed on the Nu distribution if the data is compared in terms of local ratio. Blanked data regions occur where the liquid crystals did not activate and therefore the heat transfer coefficient h values cannot be computed, the same comments also apply to the data in Fig. 5.13.
In Fig. 5.13 Nusselt maps at the investigated conditions are shown. As a general comment, an augmentation of Nu values is observed at increasing Ro, as expected in view of the rotational effects and the location at the trailing side of the ribbed wall (Coletti et al. [10], Bons and Kerrebrock [4]). The increasing trend is not monotonic, consistent with the literature where a plateau in the enhancement factor is observed for $Ro > 0.2$, the same behavior is highlighted by Mayo et al. in [24]. However, the behavior is much different if realistic or opposite buoyancy effects (cold or hot step, respectively) are applied to the flow. From the maps in Fig. 5.13, it can be appreciated how the area of high heat transfer widens much more at increasing Ro for the cold step cases. Also, much lower heat transfer is found upstream of the second rib in the hot step data.

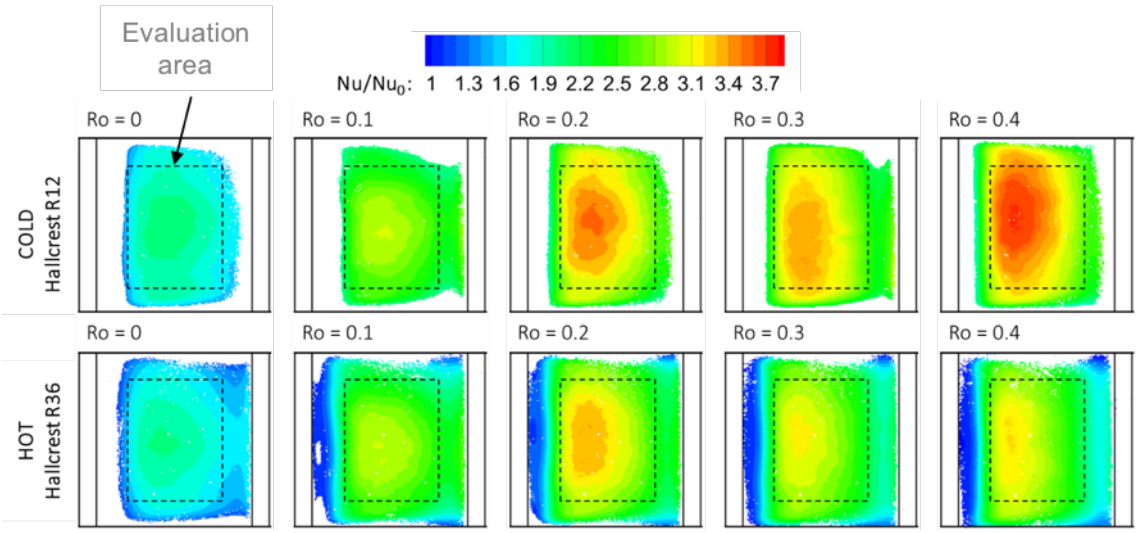

FIGURE 5.13: Nu/Nu_0 maps for cold (top) and hot (bottom) steps.

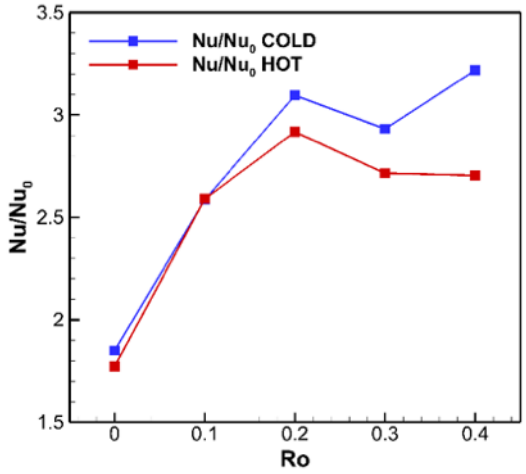

FIGURE 5.14: Averaged Nusselt comparison at different rotating conditions for cold and hot step.

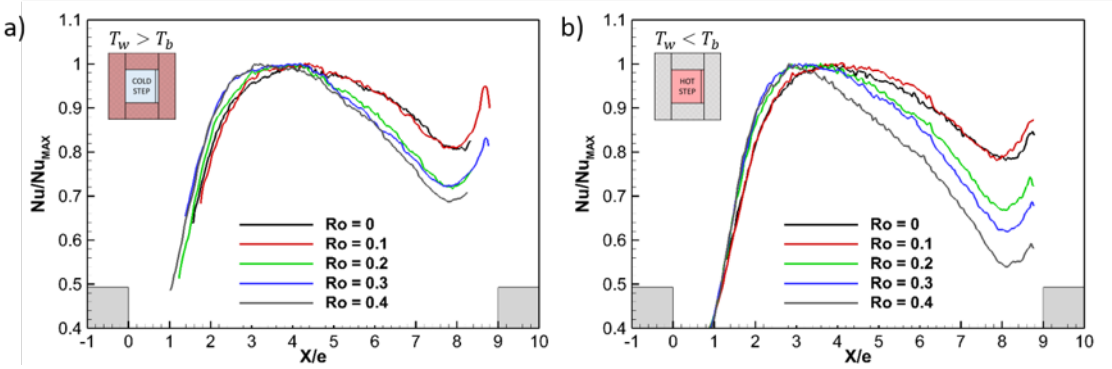

FIGURE 5.15: Nu/Nu_{MAX} comparison for $Re = 10000$, different Ro: cold step (a), hot step (b).

This behavior is clearly visible by comparing the average Nusselt values evaluated on the points within the dashed rectangle of each map of Fig. 5.13. This averaging method has been adopted in order to compare data related to zones on which liquid crystals are activated.
The result of this comparison is reported in Fig. 5.14. In can be seen that, for low rotation numbers, the imposition of opposite temperature evolution, hence opposite buoyancy effects, do not affect the heat transfer process. By increasing the rotation, the effect of different buoyancy conditions become more relevant. It is visible the plateau of the enhancement factor around $Ro = 0.3$ for the cold step and a subsequent increase of the heat transfer for $Ro = 0.4$. Conversely, for the hot step imposed to the process airflow, a further reduction of the enhancement factor is observed for Ro greater than 0.3.
A better comparison can be made by looking at the plots in Fig. 5.15, where Nu profiles along the channel centerline are compared. In order to better highlight variation in the enhancement factor profiles shapes, then modifications of the flow field, each curve is normalized with respect to its Nu maximum value. For the cold step case, the Nu profiles remain self-similar, an indication that the mean flow path does not change dramatically with rotation. In particular, the location of the heat transfer peak does not change significantly with rotation and the Nu distribution (and hence the flow field) remains almost identical once rotation is set above a certain level ($Ro > 0.2$). This is in agreement with the de-stabilizing effect of rotation on the separated shear layer at the trailing side commented by Coletti et al. [10].
By looking at the flow field behavior, results an almost stable or slightly shorter reattachment length at increasing both Ro and Bo, associated to higher turbulence intensity that explains the increased Nu. A much different behavior is found if the fluid is warmer than the wall (hot step, opposite buoyancy forces with respect to the real application). The heat transfer data suggests that rotation determines a dramatic change in the flow path. Indeed, Nu peaks move more and more upstream as Ro is increased which means an upstream motion of the reattachment points. Consistently with a more upstream reattachment location, a lower heat transfer region is found where the new boundary layer develops. Local heat transfer can drop down to 50% of the peak value, conversely to the cold step condition where, consistently with the literature (Mayo et al. [24]), 20% to 30% lower heat transfer is measured.

Chapter 6

Experimental applications: realistic internal cooling geometry

6.1 Channel geometry

In Fig. 6.1 is reported the cooling scheme considered. It has a multi-pass design where coolant enters at the blade hub in the leading edge region and moves radially outwards inside a two-sided ribbed channel (the ribs on the two sides are arranged in a line-on-line configuration). At the blade tip, part of the coolant is discharged through a dust hole (10% of inlet mass flow rate), while the greater part of it goes through a 180° bend and flows radially inwards inside the 2^{nd} passage. This latter, is again a two-sided ribbed channel with a trapezoidal cross section of high aspect ratio. At the end of the second passage, another 180° bend diverts the flow inside the 3^{rd} leg, where low aspect-ratio cylindrical pin fins are arranged in a staggered configuration to promote flow turbulence. Inside the 3^{rd} passage, the coolant is progressively discharged through holes at the blade trailing edge (55% of inlet mass flow rate) and the remaining 35% of the inlet mass flow rate is discharged at the blade tip.
The geometrical features of the ribs used in the 1^{st} and 2^{nd} legs are visible in Fig. 6.2. Ribs are designed with square section, rounded edges and base fillet, rib pitch to height ratio of 8 and inclined at 60° with respect to the radial direction. Their blockage effect inside both 1^{st} and 2^{nd} leg is about 10%. In the 3^{rd} leg pin fins have an aspect ratio of $d/D_h = 0.34$ and base fillet.
The test model considered differs with respect to the real design only because there is no curvature due to the blade camber in order to not introduce excessive distortion in the acquired images. Conversely, the correct stagger angle of the real blade (60° with respect to the peripheral velocity) is preserved.
The model is machined out of Plexiglas, successively polished to ensure a good transparency.

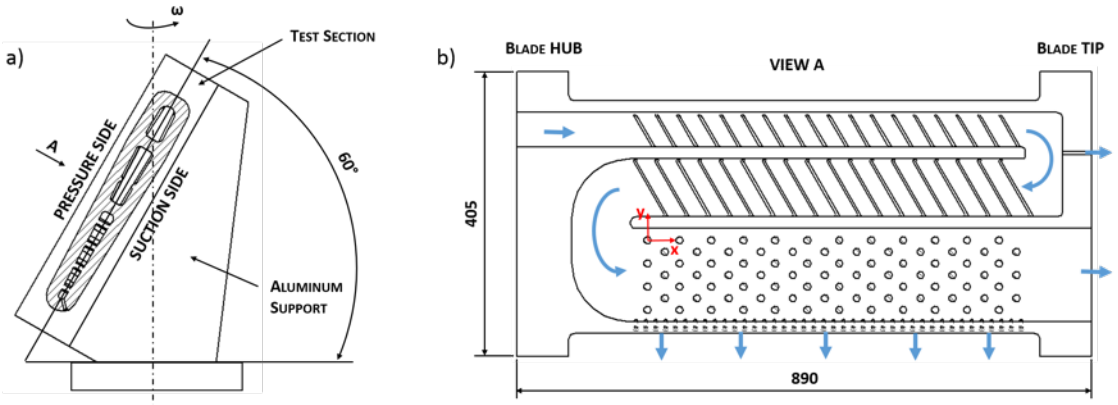

FIGURE 6.1: Test section installation (a), cooling scheme sketch (b).

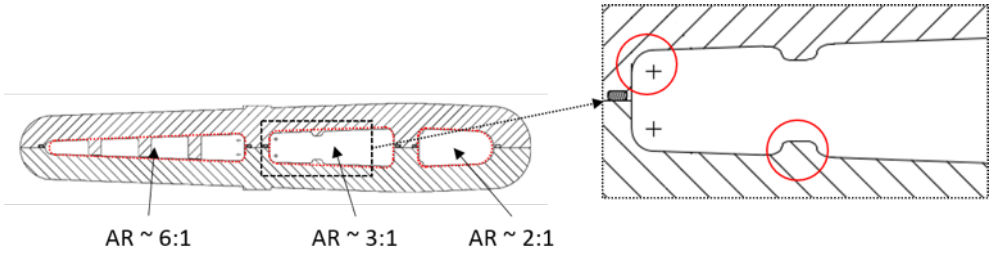

FIGURE 6.2: Cooling scheme features.

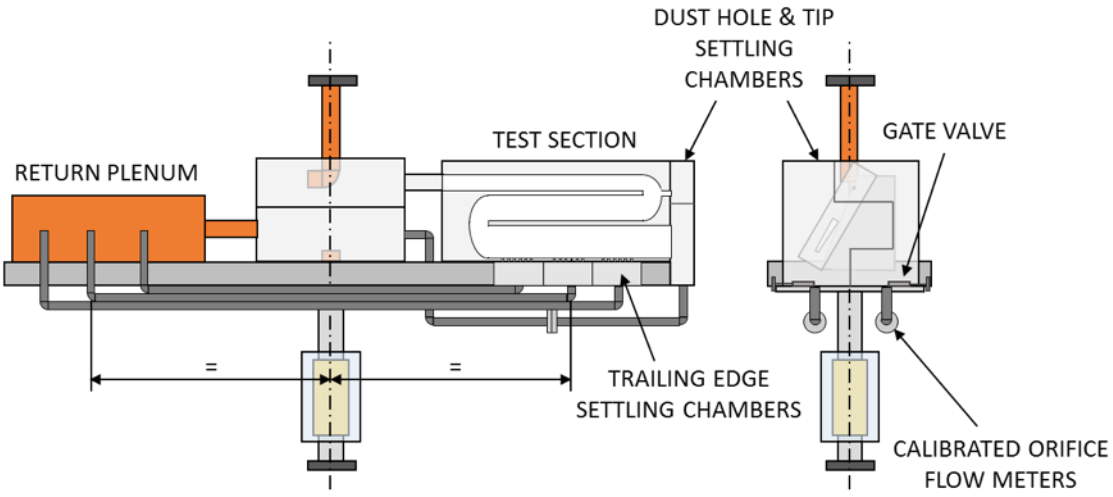

FIGURE 6.3: Sketch of mass flow rates split control.

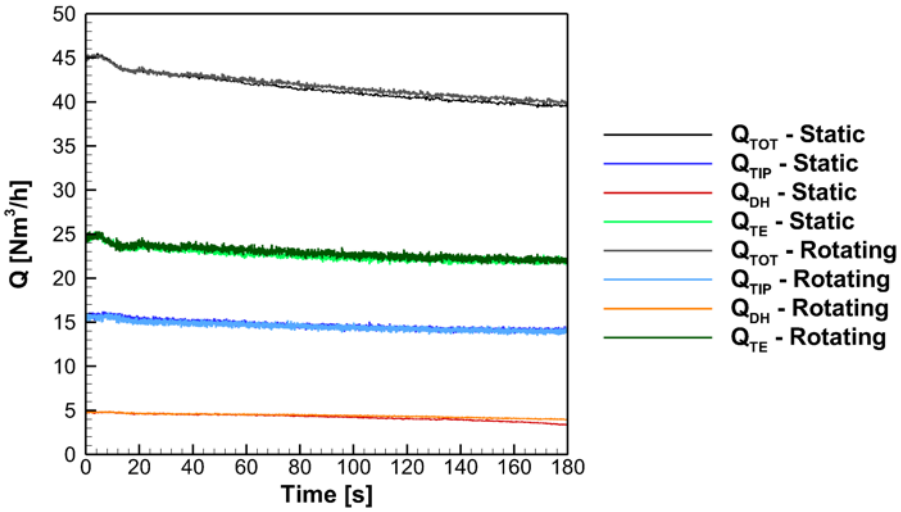

FIGURE 6.4: Mass flow rates split in static and rotating conditions.

The minimum wall thickness is about 20mm, which is sufficiently high to allow for the correct application of the transient Liquid Crystal Thermography technique.
As previously described, and reported in Fig. 6.1, the test section is characterized by multiple discharges. A correct flow split between them must be ensured during stationary and rotating test in order to reproduce real working conditions. For the tip discharges (1^{st} leg dust hole and 3^{rd} leg tip hole), the coolant exits the test section in a dedicated settling chamber, from where the flow is collected by means of instrumented pipes towards a main settling chamber placed at the center of the rotating arm and connected to the electro-fluidic joint (see Fig. 6.3). On the two collecting pipes, calibrated orifice flow meters are installed to measure the airflow rate from dust hole and 3^{rd} leg tip discharge hole, respectively. The correct flow split can be set by acting on gate valves.
A different solution has been used to control the distributed coolant flow extraction along the trailing edge holes. Each hole is connected to a settling chamber (trailing edge (*TE*) settling chambers in Fig. 6.3), which is divided in three regions accordingly to the main blade zones, namely hub, mid, and tip. The settling chambers discharge the air in a return plenum placed on the opposite side of the rotating arm. The three connection pipes extract and deliver the coolant at the same radial position. By doing so, also when the test section is spun, the same pressure gradient due to rotation is seen by each return line. Consequently, the same flow split of the static case will be automatically achieved as can be seen in Fig. 6.4 where are reported the mass flow rate splits acquired during tests in both static and rotating conditions.
In Table 6.1 are reported the normalized pressure values acquired in correspondence of the three settling chambers along the trailing edge extraction in different flow and rotating conditions. The normalization is performed with respect the dynamic pressure representative of each test evaluated as:

$$p_0 = \frac{1}{2}\rho v_{in}^2 \tag{6.1}$$

where v_{in} is the air flow velocity in correspondence of the test section inlet, where the Reynolds number representative of the experiment has been defined.
Comparing the data of each flow condition it can be observed that a uniform extraction is ensured along the trailing edge. Furthermore, the differences ϵ between static and rotating conditions evaluated as:

$$\epsilon = \frac{\left(\frac{p}{p_0}\right)_{rot} - \left(\frac{p}{p_0}\right)_{stat}}{\left(\frac{p}{p_0}\right)_{stat}} \cdot 100 \tag{6.2}$$

indicates that the return plenum works as expected. Differences below 7% are found in all the tested conditions.

TABLE 6.1: Pressure variation along the TE extraction

Re	**Ro**	$\boldsymbol{p/p_o}$			$\boldsymbol{\epsilon}$		
		TE_{HUB}	TE_{MID}	TE_{TIP}	TE_{HUB}	TE_{MID}	TE_{TIP}
17000	0	-33.8	-34.5	-34.5			
17000	0.074	-31.7	-32.3	-32.3	-6.3	-6.4	-6.3
17000	0.091	-33.3	-33.9	-33.9	-1.7	-1.7	-1.6
21000	0	-30.5	-31.4	-31.2			
21000	0.074	-28.8	-29.5	-29.5	-5.5	-5.4	-5.3

6.2 Experimental conditions and data reduction

Detailed heat transfer maps have been obtained on both pressure and suction sides of the channel. In a first experimental campaign tests have been carried out at $Re = 21000$ and $Ro = 0$ and 0.074. In order to explore the thermal behavior at higher rotation numbers, a second measurement campaign was performed at $Re = 17000$ and $Ro = 0 - 0.074 - 0.11$. All test parameters are defined at test section inlet. Both Reynolds and rotation numbers values are consistent with those that can be found inside land based gas turbines. A summary of all tested conditions is provided in Table 6.2.

TABLE 6.2: Test matrix

Re	**Ro**			**SIDE**
	0	0.074	0.11	
21000	x	x		PS
	x	x		SS
	x*			PS
17000	x	x	x	PS
	x	x	x	SS

A mix (50% in volume) of two narrow banded encapsulated liquid crystals supplied by Hallcrest has been used, namely R2C1W and R12C1W (in the following named LC2 and LC1, respectively). As reported in Par. 5.2 the activation temperatures 2 °C and 12 °C have been chosen in order to maintain, during the execution of the test, the non-dimensional temperature parameter Θ in the range between $0.3 - 0.7$ in order to reduce the data uncertainty of the results.
As the present experiments use a transient approach, the definition of the buoyancy parameter is not straightforward, as both fluid & wall temperature vary with position in the passage and with time. However, for the present experiments, considering the geometrical and working characteristics, the Bo values are low. To give an example, the Bo at the inlet of the test section, at the beginning of the temperature step is about 0.02. Therefore, buoyancy effects are expected to be negligible in the present configuration.

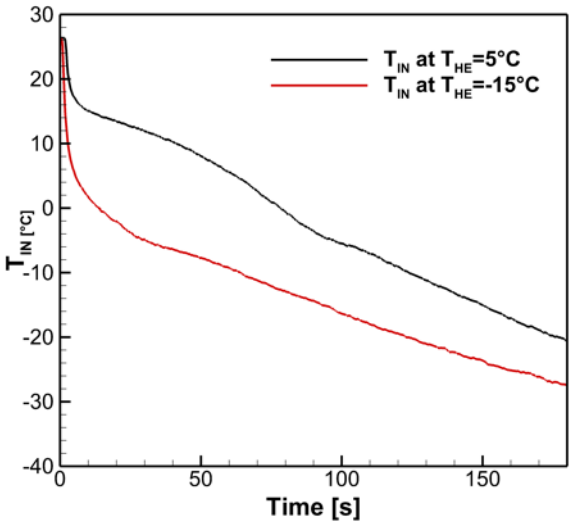

FIGURE 6.5: Achievable temperature evolutions.

Tests in static condition have been performed to assess the reliability of the developed measurement procedure. This is done by comparing the results obtained from tests carried out with the two crystals activated by the imposition of two different flow temperature evolutions, which have been obtained by different settings of the cooling system. The temperature evolutions tested are characterized by two different reference temperatures namely: $T_{HE} = 5$°C (marked x in Tab. 6.2) and $T_{HE} = -15$°C. An example of the temperature evolutions imposed to the process airflow is reported in Fig. 6.5. A consequence of these different evolutions is that the time response of the liquid crystal mixture is varied significantly, hence the robustness and accuracy of the measurement and processing procedure could be tested.
The computation of the Nusselt value has been performed with the specific hydraulic diameter of each leg. The thermal conductivity of the fluid was modelled at every position considering the time-averaged fluid temperature evolution until the liquid crystal indication took place. Nusselt normalization is performed using as reference Nusselt number the smooth channel value from classical Dittus-Boelter correlation with the exponent of the Prandtl number n set to 0.4 as required for cooling processes. The Nu_0 value is computed at the inlet of the test section and kept constant throughout the channel.

6.3 Data uncertainty: validation tests

In literature, it is possible to find different contributions about the analysis of the uncertainties in thermochromic liquid crystal measurements with the application of a transient approach.
The majority of those are based on a strong assumption that is the adoption of an ideal step-change in fluid temperature. In particular, in Yan and Owen [41] it is suggested that the non-dimensional temperature Θ should fall in a certain interval of values in order to guarantee the minimum uncertainty in the computation of the heat transfer coefficient. Hence, if the fluid initial and step temperatures are known, the best suited liquid crystals activation temperature can be calculated and an estimation of the uncertainty on the h values can be provided. However, this fully analytic approach is based on the unrealistic assumption of an ideal step where Θ is uniquely determined. Conversely, in transient experiments the fluid temperature and the respective non-dimensional temperature are not constant during the test. To overcome this limitation, in Waidmann et al. [37] the uncertainty analysis is based on a hypothetical ideal fluid temperature step that provides the same liquid crystal activation time as from the real fluid temperature history.
In this contribution, instead of pursuing the numerical approach for the uncertainty analysis with the limitations of above, it has been decided to exploit the rotating rig capabilities and assess the validity of the presented results through an empirical approach, which is considered to be more reliable.
More precisely, tests have been conducted with very different boundary conditions (such as cold step temperature) and the resulting HTC have been compared. This type of analysis not only confirms the repeatability of the experimental technique, but also allows a quantitative estimation of the integrated effects of all error sources. Indeed, the analysis of the results obtained with a single liquid crystal for different temperature steps or the analysis of the results obtained from two different liquid crystals at the same temperature step allows to highlight the measurement errors that can be generated by:

- uncertainty on the measurement of T_b;
- uncertainty on the measurement of T_w;
- uncertainty on the time detection;
- uncertainty on the determination of the material physical properties.

Figure 6.6 reports the absolute difference of the heat transfer coefficient distributions obtained by LC1 and LC2 for the test performed with the different temperature steps evaluated as follows:

$$\epsilon = \frac{|h_{LC2} - h_{LC1}|}{h_{LC1}} \cdot 100 \tag{6.3}$$

the data has been acquired on the SS only and in static condition. For the hotter step ($T_{HE} = 5°$C, Fig. 6.6a), the comparison is limited to the 1^{st} leg and a portion of the 2^{nd} one because LC2 does not activate within the test time. For both test conditions the comparison reveals that the results from the two LC are consistent, the difference being generally limited to 5%, which is far below the standard accuracy of the method. Only for the colder step ($T_{HE} = -15°$C, Fig. 6.6b), wider zone with differences above 10% can be found inside the 1^{st} leg. This is associated to the very fast activation of LC1 that occurs with this temperature step and that reduces substantially the accuracy of the indication from this liquid crystal.

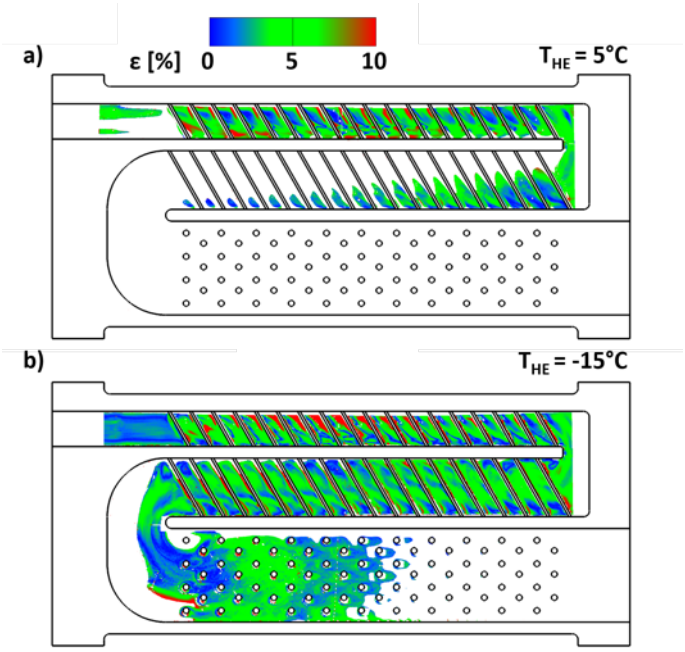

FIGURE 6.6: Differences in the measured HTC values from the two liquid crystals LC1 and LC2 and with different flow temperature evolutions (a) $T_{HE} = 5°C$, (b) $T_{HE} = -15°C$.

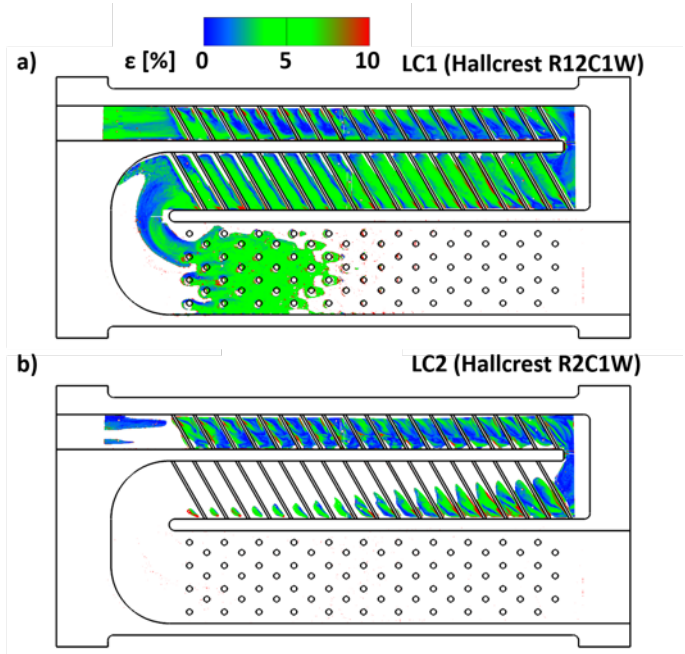

FIGURE 6.7: Differences in the measured HTC values from liquid crystals LC1 and LC2 with different flow temperature evolutions.

The effect of the step shape can be evaluated with a similar approach, by considering for each liquid crystal the difference between the heat transfer coefficient correspondent to the two temperature evolutions as reported below:

$$\epsilon = \frac{h_{T_{HE}=5°C} - h_{T_{HE}=-15°C}}{h_{T_{HE}=-15°C}} \cdot 100 \tag{6.4}$$

the results of this comparison are provided in Fig. 6.7a for LC1 and in Fig. 6.7b for LC2. Again, the differences are limited to 5%, with only small areas of higher values localized in the region of flow impingement downstream of each rib inside the 1^{st} and 2^{nd} legs, however limited to less than 10%.
Considering the results just presented, it was decided to run the experiments with always the same temperature step (the one set by the initial condition of $T_{HE} = -15°$C). The indications by LC2 are used to compute the HTC values inside the 1^{st} leg, while LC1 is used for the successive 2^{nd} and 3^{rd} legs. With these choices, the uncertainty can be assumed below 10% over the whole channel.

6.4 Results

6.4.1 Flow condition: $Re = 21000$

Rotation condition: $Ro = 0$

Figure 6.8 reports the Nu distribution maps on both PS and SS obtained for the static channel condition. At first, an overall agreement between data on PS and SS can be appreciated, as expected in view of the perfect symmetry of the passage. However, a better comparison is made by means of the Nu profiles extracted along the legs centerlines and reported in Fig. 6.9. The profiles comparison shows a very good matching between PS and SS Nu/Nu_0, which confirms the good reliability of the presented data.

Concerning the 1^{st} leg, regions of high heat transfer are found downstream of each rib, the guiding effects of the inclined ribs is also well illustrated by the contours of the Nu/Nu_0 (Fig. 6.8). As expected, an overall enhancement with respect to the smooth channel case is observed on the whole channel surface thanks to the turbulent mixing produced by the ribs (Zhou and Achatya [42], Huh et al. [16]). The same enhancement (about 1.5) is also found in the first 180° turn, at least in the measured area (the outer portion of the curve was not optically accessible). Inside the 2^{nd} leg, the behavior is similar but with the difference that the thermal field development is affected by the flow evolution after the bend. Indeed, it is well known that 180° turns without vanes (as in the present case) determine an acceleration of the fluid layer on the external side of the path with flow separation close to inner corner (Lei et al. [22] and [21]). Downstream the turn, the flow will progressively recover from separation and it will develop towards a more uniform flow distribution over the channel span. This behavior is confirmed by the present data. Regions of low Nu are found close to the lateral wall that separates from the first leg, the minimum being located close to the U-bend corner. A detail of the effect of this flow separation on the heat transfer behavior can be appreciated in Fig. 6.10. The highest Nu, extending on the wider areas, are found downstream of the first ribs of the leg. This confirms the effect of the impact, on the first turbulent promoter, of the flow accelerated in correspondence of the outer region of the bend.

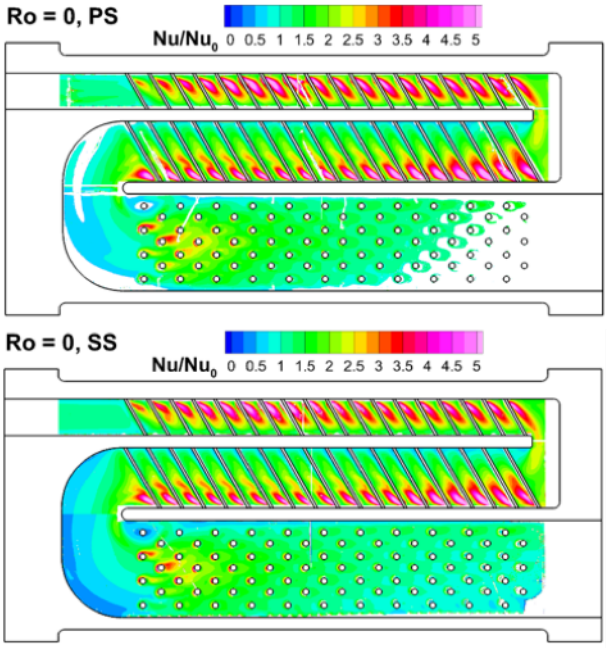

FIGURE 6.8: Nu/Nu_0 maps on pressure (top) and suction (bottom) sides of the channel for the static case.

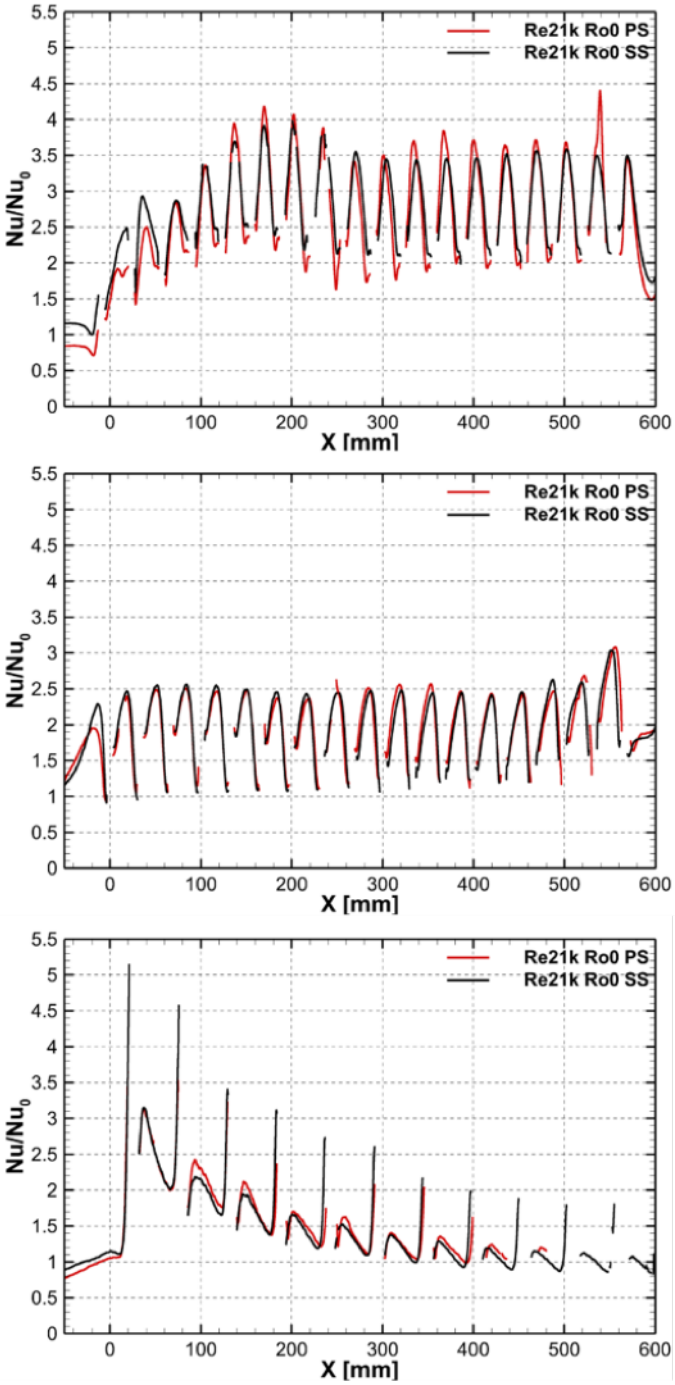

FIGURE 6.9: Comparison of Nu/Nu_0 profiles on PS and SS extracted along the legs centerlines: first leg (top), second leg (center) and third leg (bottom).

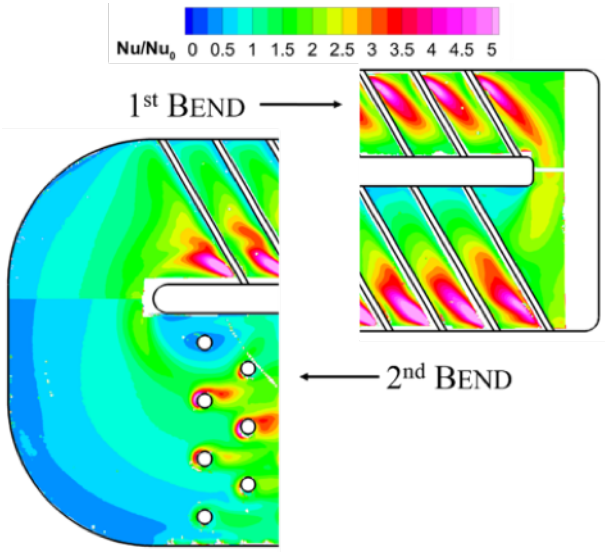

FIGURE 6.10: Details of the Nu distribution around the bend regions on SS at $Ro = 0$.

Afterwards the flow tends to recover a more uniform velocity distribution and therefore its separation above the obstacles is less intense with a consequent reduction of Nu. Inside the 3^{rd} leg, again flow separation is found close to the corner of the bend, as can be appreciated by the very low Nu values that are found around the first pin fin (Figs. 6.8, 6.10). The Nu values are higher at the beginning of the leg and they lower moving towards the blade tip due to the progressive flow discharge at the trailing edge that reduces the local Reynolds number, in agreement with previous observations of Rallabandi et al. [30]. The literature about pin fin roughened channels with lateral discharge (Rallabandi et al. [30], Willet and Bergles [39], Chang et al. [8]) reports a local augmentation of heat transfer coefficient in proximity of each exhaust hole/slot, due to the local flow acceleration. This effect cannot be seen in the present channel configuration. The number of discharge holes is very high (40) and the local amount of exhausted flow rate is consequently low. Local flow acceleration in the hole proximity is therefore not that strong to leave a footprint on the heat transfer field.

Rotation condition: $Ro = 0.074$
The Nusselt distribution maps obtained for the rotating channel case are reported in Fig. 6.11. Obviously, the same main features that were commented about the static case characterize the rotating heat transfer fields. However, the expectation is to find differences in some local features that can be directly related to rotational effects. In the introduction (1.2.1), a review about the rotational effects on radial channels has been made. It is well documented that, in a radial channel with outward flow (Fig. 6.12), the secondary structures set by rotation produce a reduction of the heat transfer on the channel leading wall (SS) where a separation zone is generated by the establishment of the Coriolis induced secondary vortex. Conversely, the impinging flow on the trailing wall (PS), causes an augmentation of the heat transfer. If the flow is radially inward, the behavior is the opposite. With this mind, in the present case by comparing static and rotating data one should expect:

- higher Nu in rotation on PS of 1^{st} and 3^{rd} leg, and on SS of 2^{nd} leg;
- lower Nu in rotation on SS of 1^{st} and 3^{rd} leg, and on PS of 2^{nd} leg.

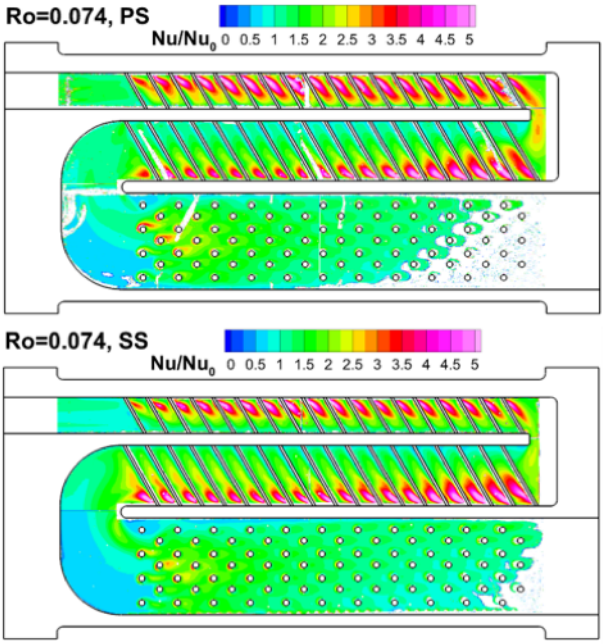

FIGURE 6.11: Nu/Nu_0 maps on pressure (top) and suction (bottom) sides of the channel for the rotating case.

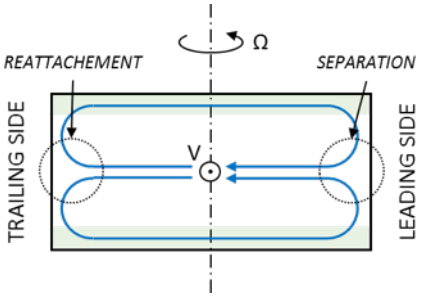

FIGURE 6.12: Effects of rotation on a radial channel with outward flow.

These effects are only partially confirmed by an initial comparison of Fig. 6.11 with Fig. 6.8 In order to highlight these predictions a closer look at defined locations for each passage is reported in Fig. 6.13. In the figure the data of the normalized Nusselt for static and rotating conditions on both pressure and suction side of the tested model is compared.
For the pressure side (Fig. 6.13a), considering the first leg it can be appreciated a wider red area for the rotating case in agreement with the prediction. Also for the second leg the prediction seems confirmed with a reduction of the heat transfer in rotation. On the third leg an augmentation of the Nusselt number is expected but the map reveals that the rotation causes a reduction of the heat transfer. It is supposed that this behavior can be related to the effects that rotation has on the upstream flow.
As said before, on the suction side (Fig. 6.13b) the effects of rotation on the heat transfer are expected to be opposite with respect to the ones above commented. For the first leg the prediction given by the simplified model seems confirmed by a visible reduction of the Nusselt. On the second leg there is no visible augmentation of the Nusselt, instead it seems that it is reducing. Conversely on the third leg it can be appreciated that a reduction of the heat transfer is shown as detected.

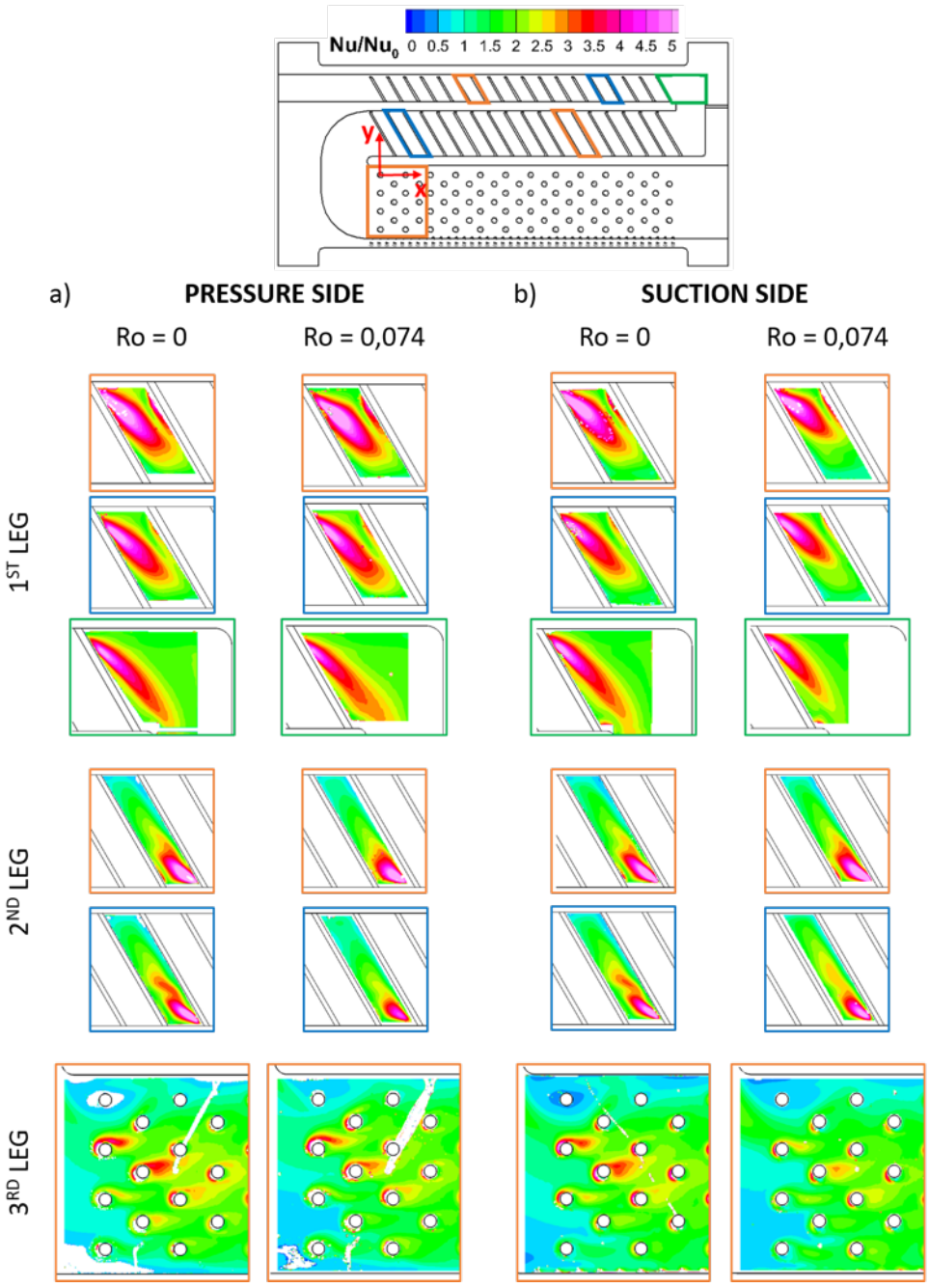

FIGURE 6.13: Nu/Nu_0 features for pressure and suction sides in static and rotating conditions.

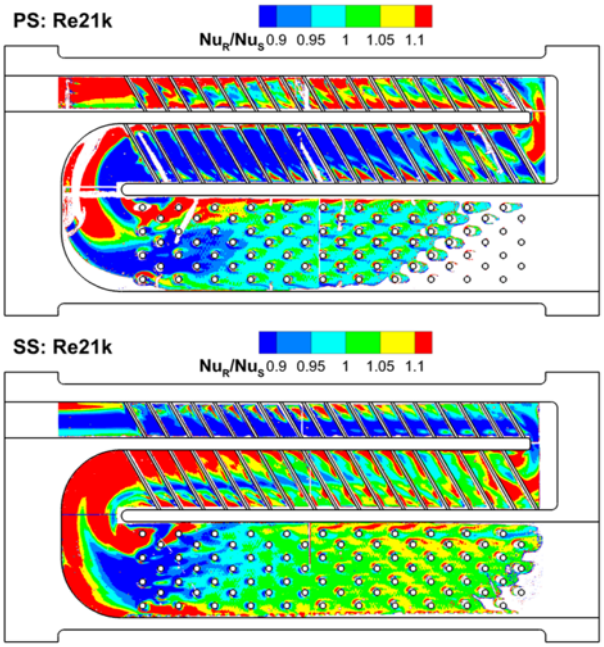

FIGURE 6.14: Nu_R/Nu_S distribution on pressure (top) and suction (bottom) sides.

These local analyses in Fig. 6.13 highlight what is happening inside the channel, such in detail is not predicted from comparison with the models that can be found in literature. A better comparison is made with the data in Fig. 6.14 that shows the ratio between the Nu values measured in rotating and static conditions on the whole maps. Indeed, an overall reduction of heat transfer can be appreciated inside the 1^{st} leg on SS and inside the 2^{nd} leg on the PS. Conversely, smaller variation between static and rotating conditions can be found inside 1^{st} leg PS and 2^{nd} leg SS, where a positive effect of rotation should be found. This behavior, unexpected with respect to the consolidated knowledge, can be explained by looking at the physics that is behind the generation of the rotation induced secondary structures.
As already reported in the introduction (1.2.1), the Coriolis structure formation and development is mainly a mechanism that is driven by the equilibrium between the forces associated with Coriolis acceleration and the induced pressure gradient. Inside the near wall flow layers, this equilibrium is unbalanced towards the pressure forces, which therefore displace the near wall flow towards the leading side of the channel. In the present case, the situation that is set is depicted in Fig. 6.15. The sketch refers to the 1^{st} leg flow configuration, where it can be seen how the misalignment between channel cross section axis and rotation axis leads to the onset of Coriolis structures that does not separate or reattach on the channel lateral walls. Indeed, in view of the physical mechanism behind the phenomenon, separation and reattachment can only exist at the external limits of the cross section. In the present case, the scenario is further complicated by the fact that the separation has to take place on a concave surface (the rounded wall on the upper part of the channel section, made to accommodate inside the blade leading edge). Separation position, which is therefore not easy to be determined, is likely to be characterized by an unsteady nature. In addition, the Coriolis vortex cells have to interact with the secondary structures induced by the ribs, making the conjecture of the overall secondary flow structure quite challenging. Hence, it appears that no flow reattachment of secondary structures will take place on the trailing wall (PS), which justifies the evidence that the heat transfer on that side is not positively influenced by rotation. The same phenomenology

applies to the SS of the 2^{nd} leg.
Inside the 3^{rd} leg, the behavior is more complex with regions of local augmentation or reduction of the Nu values both inside the PS and SS. A local reduction of Nu is observed in the first portion of the leg on both PS and SS. Conversely, rotation has a positive effect on the flow re-circulating region immediately downstream of the turn and close to the dividing wall, where very low values of Nu were found for the static case (see Fig. 6.8). After the first $4-5$ rows of pins, the Nu starts to recover and remains comparable to the static case on the PS while the SS shows a modest increase near the tip. This behavior must therefore be associated to the complex forces induced by rotation acting on the separated flow that surround the pin-fins, which is already intrinsically three dimensional in view of the short aspect ratio of the turbulators.
An overall estimation of the effects that rotation produces inside this cooling channel configuration is provided by an area-average comparison of the normalized Nusselt data.
In Fig. 6.16 is reported the area average distribution through the first two passages, only the first two legs are considered in this analysis due to the ease to compare data of areas defined by the ribs. Hence Nusselt data has been averaged for each inter-rib area, as depicted in Fig. 6.16a. With respect to the contribution of Johnson et al. [18], a good consistency can be appreciated in the trends of the Nu/Nu_0 distribution along the first passage. In the second passage, instead, a different trend is observed. In the present case, a substantial reduction of the Nu/Nu_0 values is found after the bend while in the data of Johnson et al [18] immediately after the bend values of Nu/Nu_0 up to $3.5-4$ are reported. An explanation for this different behavior can be ascribed to the different geometry of the bend region. In the present experiments, the enlargement of the channel cross section, thus the change of the hydraulic diameter, and the mass flow extraction from the dust hole, causes a local Reynolds number decrease that can be the cause of the observed reduction of enhancement after the 180° turn.
Overall performances of the passages at variation of the working conditions can be deduced by looking at the area average of Nu numbers inside each leg, computed on the whole surfaces but excluding the 180° turns. In other words, by doing the average of the data obtained from Fig. 6.16b from section 2 to 18 for the first passage and from section 21 to 37 for the second passage. Data average on the third passage has been evaluated considering the region after the 180° turn and excluding the pins. The resulting values are given in Table 6.3.
It can be appreciated again the good consistency of the data acquired on PS and SS for $Ro=0$. Rotation determines an overall reduction of the heat transfer capabilities of about $7-9\%$ on the 1^{st} leg SS and 2^{nd} leg PS. On the contrary, an augmentation of $5-8\%$ is found on the opposite surfaces.
Concerning the 3^{rd} leg, from an area averaged point of view, its thermal behavior is not affected by rotation, differently from the results reported by Rallabandi et al. [30] where rotational effects where clearly evident also on the area averaged data. This different behavior may be due to the different inlet conditions to the pin fin channels (smooth and radial for Rallabandi et al. [30], 3^{rd} passage fed by a 180° bend in the present case) and the higher Ro that characterizes the analysis performed in the available literature.

TABLE 6.3: Area averaged data

Nu/Nu_o	**Ro=0**		**Ro=0.074**		Nu_R/Nu_S	
	PS	SS	PS	SS	PS	SS
1^{st} LEG	2.69	2.57	2.90	2.38	1.08	0.93
2^{nd} LEG	2.11	2.05	1.92	2.16	0.91	1.05
3^{rd} LEG	1.40	1.37	1.39	1.35	0.99	0.99

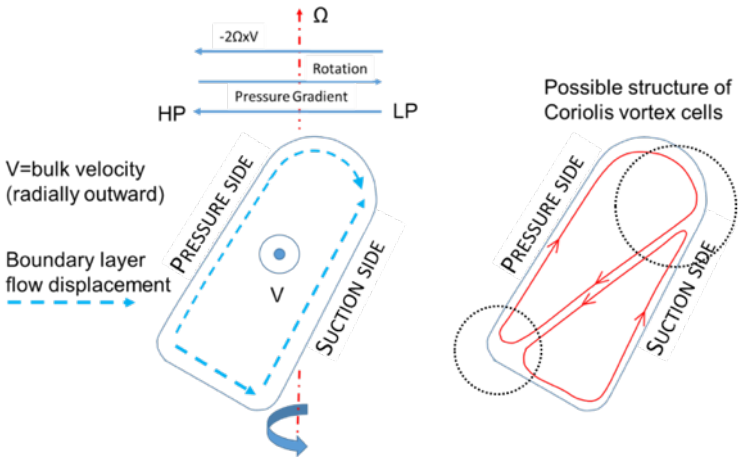

FIGURE 6.15: Effects of rotation on a radial channel with outward flow.

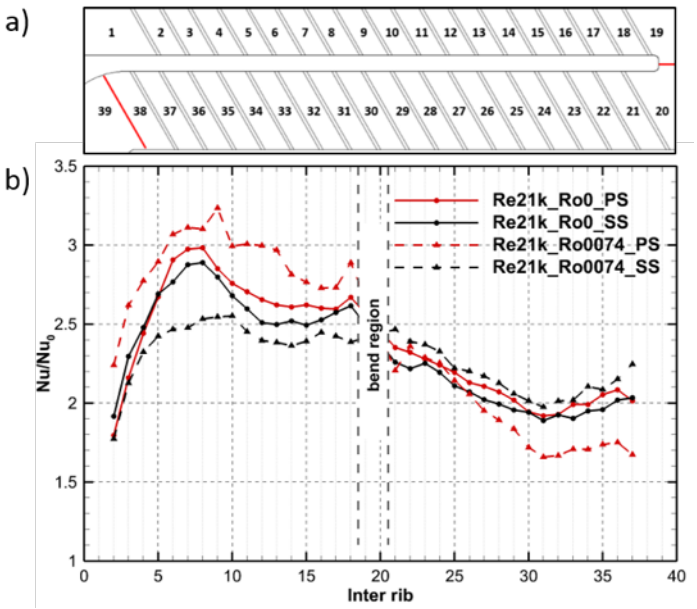

FIGURE 6.16: Detailed distribution of Nu/Nu_0 area averages for each inter rib region.

6.4.2 Flow condition: $Re = 17000$

In order to investigate higher rotation conditions, due to actual rig limitations, it has been necessary to reduce the coolant mass flow rate, hence the Reynolds number at the section inlet at $Re = 17000$. Unfortunately, by doing this only inside the 1^{st} leg a complete activation of liquid crystals is achieved. For this reason, all further analysis and comparisons are limited to the 1^{st} leg of the test section.
Figure 6.17 shows the Nusselt contour plots inside the 1^{st} leg on both pressure and suction side for $Ro = 0 - 0.074 - 0.11$. A first look confirms the different behavior on pressure and suction side due to rotation previously presented for the flow condition with $Re = 21000$. As it can be seen on the suction side, the high Nusselt areas show a decrease with rotation, the difference getting larger with higher rotation number, on the contrary on pressure side at first sight there are no large variations in the contour plots. In order to better highlight the Nusselt trends along the channels area averaged values are represented in Fig. 6.17g.
This analysis, as well as confirming the above considerations, reveals a seemingly counterintuitive effect. On suction side Nu/Nu_0 values decrease monotonically increasing the rotation number, as normally expected. On the contrary, on pressure side a non-monotonic trend is observed: Nu values show a general increase when moving from static to the lower rotation condition ($Ro = 0.074$) as expected, while a further increase of rotational speed (from $Ro = 0.074$ to 0.11) does not determine higher Nu but values that are comparable to the static case.
The same phenomenon was observed on the pressure data acquired along the channel on the pressure side. In order to carry out these measurements, pressure taps were installed at the beginning and end of each leg. By the use of a 16 channel pressure scanner (NetScanner System mod.9116) (see 3.3.1), it was possible to acquire the pressure values at different test conditions.

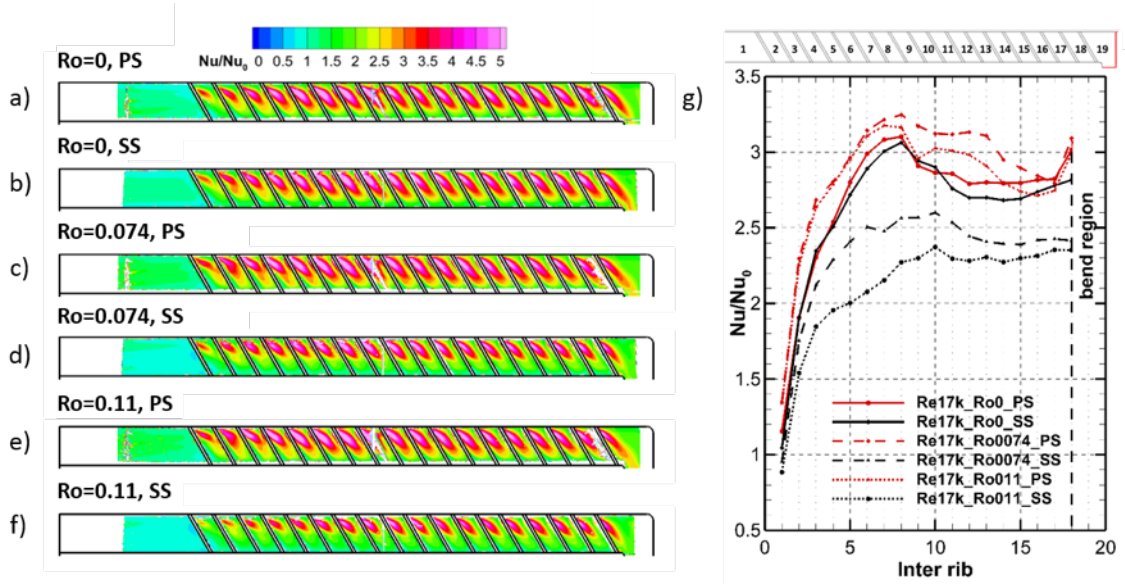

FIGURE 6.17: Nu/Nu_0 maps for $Re = 17000$: $PS - Ro = 0$ (a), $SS - Ro = 0$ (b), $PS - Ro = 0.074$ (c), $SS - Ro = 0.074$ (d), $PS - Ro = 0.11$ (e), $SS - Ro = 0.11$ (f), area averaged values (g).

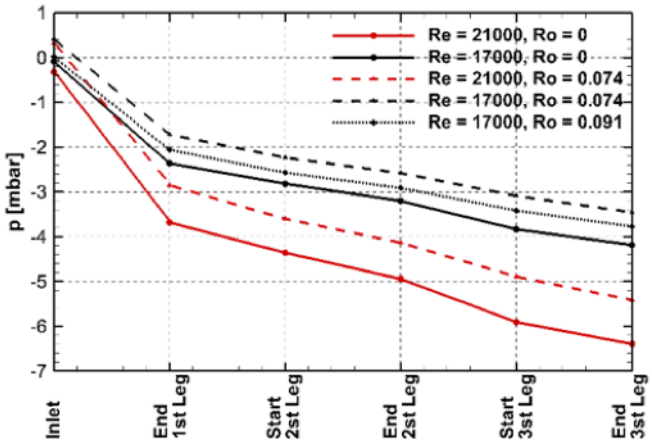

FIGURE 6.18: Pressure distribution along the channels.

The pressure measurements were performed in a second campaign with respect to the heat transfer measurements. Unfortunately the arise of structural problems during rotation at high speed doesn't allow to replicate the same flow and rotating conditions of the first measurement campaign, limiting the Ro parameter to 0.091 instead 0.11 for the Re condition of 17000.
This condition has been replaced with a similar Reynolds number and $Ro = 0.091$ which still allows a qualitative analysis of the pressure data to be performed.
Pressure data is summarized in Fig. 6.18. As it can be seen pressure data at $Re = 17000$ highlights the same behavior as Nu/Nu_0 data presented in Fig. 6.17g. Since the pressure field is generated by the velocity field, which also influences the thermal field it is evident that the two behaviors should be similar. It is clear that the described behavior is dominated by rotational effects that are not easy to be fully understood in view of the complexity of the geometry and working condition (non-orthogonal rotation). A close look at the flow behavior (either by experiment or CFD) would be mandatory to gain more insight about the aero-thermal behavior of the device.

Chapter 7

Conclusions

The design and operation of a new rig for heat transfer measurements in rotation have been presented.
The challenging task to apply transient liquid crystal in rotation and on large models posed many technical issues that have been solved.
The designed test facility is characterized by:

- the possibility to install different types of test models, including full blade models with dimensions up to $890 \times 440 \times 610$ mm maintaining the same stagger angle of the real blade;
- the possibility to explore flow and rotation conditions up to Reynolds number 40000 and rotation number 0.4 at about 400 rpm;
- an on board image and temperature acquisition system in order to avoid the synchronization between rotation and acquisition;
- a feedback control system that acts in order to maintain the test parameters (Re, Ro) constant throughout the test;
- the possibility to impose different temperature evolutions to the process air flow with the use of different air conditioning systems: a mesh heater for the hot temperature steps and a N_2-air system in order to impose cold temperature steps to the air flow.

Many efforts have focused on the development of a software for the analysis of acquired data, and thus allow for the calculation of the surface heat transfer coefficient. In particular, a lot of time has been spent in developing and validating a code that would allow:

- the processing of highly distorted images;
- the computation of the bulk flow temperature directly on the geometry of the test model;
- the analysis of multi peak signals derived from the usage of multiple liquid crystals. It was therefore sought to find a solution that would allow the correct search of peaks of different shapes and sizes and their validation (in terms of activation and amplitude order)

A first part of the activity was then focused on validating the measurement system on a stereotyped geometry representative of a first passage of a cooling system. The chosen geometry is a square channel with ribs positioned only on the trailing side.
In the second part the attention was focused on a representative geometry of a blade cooling scheme. The geometry consists of three passages, the first two with inclined ribs and the third with pin fins arranged in a staggered configuration, was tested at different rotation conditions and heat transfer data were acquired both on the pressure and suction side.

7.1 One-side ribbed square channel

The rig and the methodology have been successfully validated with a wide tests campaign on a simplified internal cooling geometry. In particular, rotating tests have been performed at different Ro and Bo values, repeating the same experiment also by imposing opposite buoyancy forces with respect to the real application, i.e. by warming the fluid as usually done with the transient liquid crystal approach. The reported results confirm the need to go for the presented methodology in order to achieve meaningful heat transfer data, even at the relatively low values of Ro and Bo here considered. However, these results represent only the first steps into the validation process of such complex methodology. One of the crucial point that remains open is the effect on the final accuracy of the buoyancy forces that are actually changing during the test, which is associated to the wall and flow temperature variation required by the transient approach.

7.2 Realistic internal cooling geometry

Detailed heat transfer maps were evaluated on both suction side and pressure side of a real cooling scheme characterized by three passages with rib turbulators on the first and the second passage and pin fins on the third. Spatially resolved heat transfer maps highlighted the effects of rotation for both Reynolds conditions (21000 and 17000) evaluated in correspondence of the test section inlet and rotation numbers of 0.074 for the first flow condition, 0.074 and 0.11 for the latter. A consistent detrimental effect on the Nu values has been found inside the 1^{st} leg SS and 2^{nd} leg PS, while on the opposite walls (1^{st} leg PS and 2^{nd} leg SS), an increment of the heat transfer is found with respect to the static case. This behavior is explained by the combined effect of the present channel orientation and cross-section. Inside the pin fins roughened 3^{rd} leg, rotation has complex and localized effects, but the area averaged Nu values remains practically unchanged between static and rotating conditions, confirming previous contributions. Furthermore, pressure drops inside the channels confirm the trends highlighted by the heat transfer analysis, confirming the influence of the flow field on the heat transfer process.

7.3 Future developements

As future developments of this work, we have increased the test facility potential by installing a more powerful electric motor (11 kW with respect the actual 5 kW) and a new transmission, in order to broaden the available test conditions. Another point to focus on is the development of a test mode for the correct evaluation of buoyancy during the transient phase.

Bibliography

[1] P.S. Addison. *The Illustrated Wavelet Transform Handbook*. Institute of Physics, 2002.

[2] T. Astarita et al. "Some experimental investigations on gas turbine cooling performed with infrared thermography at Federico II". In: *International Journal of Rotating Machinery* (2015). URL: http://dx.doi.org/10.1155/2015/890414.

[3] C.B. Bayley and R.S. Bunker. "Heat transfer and friction in channels with very high blockage 45° staggered turbulators". In: *ASME Turbo Expo 2003, collocated with the 2003 International Joint Power Generation Conference*. Vol. Volume 5. 2003.

[4] J.P. Bons and J.L. Kerrebrock. "Complementary velocity and heat transfer measurements in a rotating cooling passage with smooth walls". In: *ASME 1998 International Gas Turbine and Aeroengine Congress and Exhibition*. Vol. Volume 4: Heat Transfer; Electric Power; Industrial and Cogeneration. 1998.

[5] M. Çacan. "Aero-thermal investigation of fixed rib-roughened internal cooling passages". MA thesis. Université Catholique De Louvain, 2000.

[6] L. Casarsa and T. Arts. "Experimental investigation of the aerothermal performance of a high blockage rib-roughened cooling channel". In: *Journal of Turbomachinery* 127.3 (2005). URL: https://doi.org/10.1115/1.1928933.

[7] P.R. Chandra, M.L. Fontenot, and J.C. Han. "Effect of rib profiles on turbulent channel flow heat transfer". In: *Journal of Thermophysics and Heat Transfer* 12.1 (1998), pp. 116–118. URL: https://doi.org/10.2514/2.6312.

[8] S.W. Chang et al. "Heat transfer in radially rotating pin-fin channel at high rotation numbers". In: *Journal of Turbomachinery* 132.2 (2010). URL: https://doi.org/10.1115/1.3147103.

[9] M.K. Chyu, Y.C. Hsing, and V. Natarajan. "Convective heat transfer of cubic fin arrays in a narrow channel". In: *Journal of Turbomachinery* 120.2 (1998), pp. 362–367. URL: https://doi.org/10.1115/1.2841414.

[10] F. Coletti et al. "Turbulent flow in rib-roughened channel under the effect of Coriolis and rotational buoyancy forces". In: *Physics of Fluids* 26 (2014). URL: http://dx.doi.org/10.1063/1.4871019.

[11] N. Domaschke, J. von Wolfersdorf, and K. Semmler. "Heat transfer and pressure drop measurements in a rib roughened leading edge cooling channel". In: *Journal of Turbomachinery* 134.6 (2012). URL: https://doi.org/10.1115/1.4004747.

[12] S. Dutta and J.C. Han. "Local heat transfer in rotating smooth and ribbed two-pass square channels with three channel configurations". In: *Journal of Heat Transfer* 118.3 (1996), pp. 578–584. URL: https://doi.org/10.1115/1.2822671.

[13] S.V. Ekkad and J.C. Han. "A transient liquid crystal thermography technique for gas turbine heat transfer measurements". In: *International Journal of Heat and Fluid Flow* 11.7 (2000). URL: https://doi.org/10.1088/0957-0233/11/7/312.

[14] L. Furlani, A. Armellini, and L. Casarsa. "Effects of rotation and buoyancy forces on the flow and behavior inside a triangular rib roughened channel". In: *Journal of Turbomachinery* 139.5 (2017). URL: http://dx.doi.org/10.1115/1.4035103.

[15] J.E. Hart. "Instability and secondary motion in a rotating channel flow". In: *Journal of Fluid Mechanics* 45.2 (1971), pp. 341–351. URL: https://doi.org/10.1017/S0022112071000077.

[16] M. Huh, J. Lei, and J.C. Han. "Influence of channel orientation on heat transfer in a two-pass smooth and ribbed rectangular channel (AR=2:1) under large rotation numbers". In: *Journal of Turbomachinery* 134.1 (2010). URL: https://doi.org/10.1115/1.4003172.

[17] P.T. Ireland and T.V. Jones. "Liquid crystal measurements of heat transfer and surface shear stress". In: *Measurement Science and Technology* 11.7 (2000). URL: https://doi.org/10.1088/0957-0233/11/7/313.

[18] B.V. Johnson et al. "Heat transfer in rotating serpentine passages with trips skewed to the flow". In: *Journal of Turbomachinery* 116.1 (1994), pp. 113–123. URL: https://doi.org/10.1115/1.2928265.

[19] J.P. Johnston, R.M. Halleent, and D.K. Lezius. "Effects of spanwise rotation on the structure of two-dimensional fully developed turbulent channel flow". In: *Journal of Fluid Mechanics* 56.3 (1972). URL: https://doi.org/10.1017/S0022112072002502.

[20] S. Kunstmann, J. von Wolfersdorf, and U. Ruedel. "Heat transfer and pressure loss in rectangular one-side-ribbed channels with different aspect ratios". In: *Journal of Turbomachinery* 135.3 (2013). URL: https://doi.org/10.1115/1.4006871.

[21] J. Lei et al. "Heat transfer in rotating multi-pass rectangular smooth channel with and without a turning vane in hub region". In: *ASME Turbo Expo 2013: Turbine Technical Conference and Exposition*. Vol. Volume 3A: Heat Transfer. 2013.

[22] J. Lei et al. "The effect of a hub turning vane on turbulent flow and heat transfer in a four-pass channel at high rotation numbers". In: *International Journal of Heat and Mass Transfer* 92 (2016), pp. 578–588. URL: https://doi.org/10.1016/j.ijheatmasstransfer.2015.08.034.

[23] D.K. Lezius and J.P. Johnston. "Roll-cell instabilities in rotating laminar and turbulent channel flows". In: *Journal of Fluid Mechanics* 77 (1976), pp. 153–175. URL: https://doi.org/10.1017/S0022112076001171.

[24] I. Mayo et al. "Aerothermal characterization of a rotating ribbed channel at engine representative conditions - Part II: detailed liquid crystal thermography measurements". In: *Journal of Turbomachinery* 138.10 (2016). URL: https://doi.org/10.1115/1.4032927.

[25] I. Mayo et al. "Two-dimensional heat transfer distribution of a rotating ribbed channel at different reynolds numbers". In: *Journal of Turbomachinery* 137.3 (2014). URL: http://dx.doi.org/10.1115/1.4028458.

[26] D.E. Metzger, C.S. Fan, and S.W. Haley. "Effects of pin shape and array orientation on heat transfer and pressure loss in pin fin arrays". In: *Journal of Engeneering Gas Turbines Power* 106.1 (1984), pp. 252–257. URL: https://doi.org/10.1115/1.3239545.

[27] M. Pascotto et al. "Coriolis effects on the flow field inside a rotating triangular channel for leading edge cooling". In: *Journal of Turbomachinery* 136.3 (2013). URL: http://dx.doi.org/10.1115/1.4025570.

[28] R. Poser, J. von Wolfersdorf, and E. Lutum. "Advanced evaluation of transient heat transfer experiments using thermochromic liquid crystals". In: *Journal of Power and Energy* 221.6 (2007), pp. 793–801. URL: https://doi.org/10.1243/09576509JPE464.

[29] L. Qiu, H. Deng, and Z. Tao. "Effect of channel orientation in a rotating wedge-shaped cooling channel with pin fins and ribs". In: *ASME Turbo Expo 2012: Turbine Technical Conference and Exposition*. Vol. Volume 4: Heat Transfer, Parts A and B. 2012.

[30] A.P. Rallabandi, Y.H. Liu, and J.C. Han. "Heat transfer in trailing edge wedge-shaped pin-fin channels with slot ejection under high rotation numbers". In: *ASME Turbo Expo 2010: Power for Land, Sea, and Air*. Vol. Volume 4: Heat Transfer, Parts A and B. 2010.

[31] D.L. Schultz and T.V. Jones. *Heat-transfer measurements in short-duration hypersonic facilities*. Vol. 165. AGARD, 1973.

[32] C.G. Speziale. "Numerical study of viscous flow in rotating rectangular ducts". In: *Journal of Fluid Mechanics* 122 (1982), pp. 251–271. URL: https://doi.org/10.1017/S0022112082002201.

[33] C.G. Speziale and S. Thangam. "Numerical study of secondary flows and roll-cell instabilities in rotating channel flow". In: *Journal of Fluid Mechanics* 130 (1983), pp. 377–395. URL: https://doi.org/10.1017/S0022112083001135.

[34] M.E. Taslim and S.D. Spring. "Effects of turbulator profile and spacing on heat transfer and friction in a channel". In: *Journal of Thermophysics and Heat Transfer* 8.3 (1994), pp. 555–562. URL: https://doi.org/10.2514/3.578.

[35] D.J. Tritton. "Stabilization and destabilization of turbulent shear flow in a rotating fluid". In: *Journal of Fluid Mechanics* 241 (1992). URL: https://doi.org/10.1017/S0022112092002131.

[36] J.H. Wagner et al. "Heat transfer in rotating serpentine passages with trips normal to the flow". In: *Journal of Turbomachinery* 114.4 (1992). URL: https://doi.org/10.1115/1.2928038.

[37] C. Waidmann, R. Poser, and J. von Wolfersdorf. "Application of thermochromic liquid crystal mixtures for transient heat transfer measurements". In: *10th European Conference on Turbomachinery Fluid Dynamics and Thermodynamics, ETC 2013 2014*. 1. 2014, pp. 685–696.

[38] C. Waidmann et al. "Investigations of heat transfer and pressure loss in an engine-similar two-pass internal blade cooling configuration". In: *ASME Turbo Expo 2013*. 2013.

[39] F.T. Willet and A.E. Bergles. "Heat transfer in rotating narrow rectangular pin-fin ducts". In: *Experimental Thermal and Fluid Science* 25.7 (2002), pp. 573–582. URL: https://doi.org/10.1016/S0894-1777(01)00103-0.

[40] L.M. Wright et al. "Heat transfer in trailing edge, wedge-shaped cooling channels under high rotation numbers". In: *Journal of Heat Transfer* 130.7 (2008). URL: https://doi.org/10.1115/1.2907437.

[41] Y.Y. Yan and M. Owen. "Uncertainties in transient heat transfer measurements with liquid crystals". In: *International Journal of Heat and Fluid Flow* 23.1 (2002), pp. 29–35. URL: https://doi.org/10.1016/S0142-727X(01)00125-4.

[42] F. Zhou and S. Acharya. "Heat transfer at high rotation numbers in a two pass 4:1 aspect ratio rectangular channel with 45 degree skewed ribs". In: *Journal of Turbomachinery* 130.2 (2008). URL: http://dx.doi.org/10.1115/1.2752185.